Propulsion Considerations for Supersonic Oblique Flying Wings

by
Yuto Shinagawa

B.S. Aerospace Engineering
University of Texas at Austin, 2003

SUBMITTED TO THE DEPARTMENT OF AERONAUTICS AND ASTRONAUTICS
IN PARTIAL FULFILLMENT OF THE REQUIREMENTS FOR THE DEGREE OF

MASTER OF SCIENCE IN AERONAUTICS AND ASTRONAUTICS
AT THE
MASSACHUSETTS INSTITUTE OF TECHNOLOGY

FEBRUARY 2006

Signature of Author: _____
Department of Aeronautics and Astronautics
February 3, 2006

Certified by: _____
Alan H. Epstein
R.C. Maclaurin Professor of Aeronautics and Astronautics
Thesis Supervisor

Accepted by: _____
Jaime Peraire
Professor of Aeronautics and Astronautics
Chair, Committee on Graduate Students

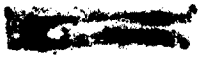

Propulsion Considerations for Supersonic Oblique Flying Wings

by
Yuto Shinagawa

Submitted to the Department of Aeronautics and Astronautics on February 3, 2006 in partial fulfillment of the requirements for the degree of Master of Science in Aeronautics and Astronautics

Abstract

Propulsion considerations unique to the supersonic oblique flying wing, including cycle selection, sizing, and integration were investigated via the development and interrogation of aerodynamic and propulsive synthesis models. These models were an amalgamation of computational tools (MSES), linearized theory, parametric estimation, and quasi 1D thermodynamic cycle analysis. Lift-to-drag ratio, thrust specific fuel consumption, and nacelle wave drag were examined as intermediate figures of merit that would ultimately impact the final performance metric—namely, range parameter and specific excess power.

It was found that higher bypass ratio engines could yield an increase in the range parameter up until a critical mach number, above which the increasing nacelle drag would offset the TSFC reductions to yield a net degradation in range performance. Between the baseline TF30-type cycle and its BPR 2.4 modified variant, this critical mach number was found to be at approximately M 2.0 for $T_{T4}/T_{T2} = 5$, and M 2.2 for $T_{T4}/T_{T2} = 6$.

The OFW whose engine was sized for supersonic cruise was also found to have less excess power throughout the low speed regime and hence, longer climb and acceleration times than a comparable symmetric-wing supersonic aircraft. It was concluded that the OFW's reduced drag at supersonic cruise mitigates the gross oversizing of the engine that is common and inevitable for conventional supersonic aircraft at takeoff.

Preliminary investigation of the turntable-mounted engine and slot-inlet have demonstrated their feasibility as viable engine integration concepts, but has also revealed the need for integrated design solutions, such as the development of a novel flat-top airfoil, aggressive S-ducts, and in general, a highly compact engine.

Thesis Supervisor: Dr. Alan H. Epstein
Title: R.C. Maclaurin Professor of Aeronautics and Astronautics

Acknowledgements

It was truly a privilege to have had the opportunity to brush sleeves with so many distinguished academians. I owe my gratitude to all with whom I had the opportunity to work with, some whose guidance was direct, and others indirect, but all of whom are unquestionably the best in the business.

Thank you Professor Epstein, for letting me work on a research project that I considered to be the best project at the Institute – you are right; all projects should be this fun, but only in an ideal world. I always enjoyed your pertinent anecdotes. I think they teach just as well the relevant lessons that are to be learned, as do numbers and formulas.

An equal amount of gratitude is deserved by Professor Mark Drela of the ACDL, whose infinite aeronautical wisdom frequently transcended my cognitive capabilities. You have no idea how many times I spent hours wracking my brain over a convoluted thought, only to realize that the end result was exactly what you had asserted in an earlier meeting, or even worse, to have it invalidated in the next. Those hours weren't in vain though, for that's all part of the learning process.

But it was Ali Merchant who often translated Dr. Drela's unfathomable concepts to a language more suited for my comprehension (English), and thus deserves part of the credit. I owe you one, buddy. By the way, Colonel Young says you need to go fly your planes more often. Incidentally, Colonel Young is the one—although not directly involved in my research—with whom I have spent countless hours chatting and in correspondence with about airplanes—a true kindred spirit.

I would also like to convey my gratitude to Dr. Ilan Kroo and his colleagues at Desktop Aero for sharing their one-of-a-kind aeronautical expertise, and to Mr. Thomas Beutner at DARPA for asking the right (most relevant) questions to steer my research in the right direction.

I am also obliged to a good friend and a fellow Longhorn, Mohit Garg for giving me the privilege to proofread his thesis and to brush up my grammar skills in the process. I would have returned you the favor, but I understand you have more fun things to do, like studying for your upcoming quals. I'll stay true to my common practice and refrain from wishing you good luck, since when you *do* pass, it is you that deserve it and not luck.

And who could forget my fellow researchers at the GTL. Listing their names here would be imprudent since there are simply too many to be thanked, and as I would inevitably leave out a deserving name. I'd like to end by saying that as "unsociable" a place MIT is supposed to be, I'll undoubtedly remember this place, not for the research and academics, but for its social prosperity. Thank you.

Table of Contents

List of Figures and Tables

List of Principal Symbols

a	local speed of sound
A	cross sectional area
AR	aspect ratio
b	span
c	chord
C_d	section profile drag
C_{dp}	section pressure drag
C_{df}	section friction drag
C_D	total drag
C_{Df}	overall friction drag
C_{Di}	induced drag
C_{Dnac}	nacelle drag
C_{Do}	parasite "zero-lift" drag (includes wave)
$C_{Dw,l}$	wave drag due to lift
$C_{Dw,v}$	wave drag due to volume
C_{Dpf}	overall profile drag (parasite drag without wave)
C_l	section lift coefficient
C_L	aircraft lift coefficient
d	diameter
D	drag force
e	Oswald's efficiency factor
eef	engine efficiency factor
ef	empty weight fraction
f	fuel to air ratio
ff	fuel fraction
g	gravitational constant
h	altitude
K_o	wave drag due to volume factor
K_w	wave drag due to lift factor
l	length
L	lift force
l/d	length-to-diameter ratio
L/D	lift-to-drag ratio
$\dot{m}$	mass flow
M	mach number
N	spool speed
OPR	overall pressure ratio
P_s	specific excess power
P_t	total pressure
pf	payload fraction
pnt	percent no taper

psp	excess power parameter
q	dynamic pressure
$\Re$	real part
R	range
Re	Reynold's number
R.P	range parameter
S_{ref}	reference area
t	thickness
T	thrust
T_t	total temperature
TSFC	thrust specific fuel consumption
u	flow velocity
v	flight velocity
V	volume
W	weight
W/S	wing loading

Greek Letters

α	bypass ratio
β	compressibility parameter
β	relative flow angle
γ	ratio of specific heats
Λ	oblique sweep angle
ε	engine installation angle
σ	axis ratio
ψ	complementary oblique sweep angle
ρ	density
π_i	inlet pressure recovery
π_c	compressor pressure ratio
π_f	fan pressure ratio
χ	flight path angle

Subscripts

uninst	uninstalled
inst	installed
nac	nacelle
red	reduced
eff	effective
$\perp$	perpendicular

List of Acronyms

BV	Blohm and Voss
CG	center of gravity
DARPA	Defense Advanced Research Projects Agency
HBR	high bypass ratio
HSCT	high speed civil transport
OFW	oblique flying wing
ME	Messerschmitt
MIT	Massachusetts Institute of Technology
NACA	National Advisory Committee for Aeronautics
NASA	National Aeronautics and Space Administration
NM	nautical mile
QSP	Quiet Supersonic Platform
SST	supersonic transport
STF	supersonic through-flow fan
TFX	Joint Service Requirements
TRL	Technology Readiness Level
UAV	unmanned aerial vehicle
VCE	variable cycle engine

Chapter 1

Introduction

The oblique flying wing is viewed by many an aerodynamicist to be the ideal geometry for an aircraft that is to travel at transonic speeds and above. Indeed, ever since RT Jones's invention of the concept in 1952, the OFW has been the subject of numerous studies and technical papers both in academia and industry. And yet, during the same half-century that brought forth the breathtaking emergence of the jet and space age, the aerospace community continues to make surprisingly little progress on its development beyond the conceptual phase of a design study. Part of the blame lies in the social, political and economic circumstances that, until recently, have been beyond the control of the aerospace engineer. Fuel prices, sonic boom, market demand, and ozone depletion are all words that one typically hears in any discussion of a viable supersonic transport (SST), and are also factors that have conspired against its realization. For the most part, however, its struggle stems from the inherent difficulties that arise from combining characteristics that are most challenging to flight including asymmetry, supersonic aerodynamics, and most importantly, the lack of precedence – or at least one that hasn't had its share of problems.

1.1 History

The oblique flying wing borrows its features from a variety of concepts that existed long before its conception in the mid 1950s. The unswept flying wing and the variable swept wing can both trace their origins back to the Horten flying wings of the 1930s and the Blohm and Voss P.202 pivoting wing concept of the 1940s. These German engineers foresaw the structural benefits of span-loading an aircraft in the shape of a flying wing. Likewise, the variable sweep engineers of BV and ME deemed that a variable sweep wing

could potentially preclude an otherwise inevitable compromise between low-speed and transonic aerodynamic performance. Following World War II, both of these concepts were reborn under American development programs and their temperaments thoroughly investigated with planes such as Northrop's B-35 and B-49 flying wings, and Bell X-5 and Grumman XF10F symmetric swing-wing aircraft [1]. Engineers and pilots in particular were not impressed with the flying qualities of these experimental concepts. In particular, Northrop's flying wings exposed unprecedented stability and control issues when a number of test flights ended in fatal crashes. As a result, the Air Force eventually cancelled Northrop's flying wing program.

It was about the same time that NACA researcher, Dr. R.T Jones developed the theory for the oblique flying wing and revealed its aerodynamic superiority over conventional symmetric-wing aircraft. A decade later in 1961, Mr. G. Lee of Handley Page revisited the concept to propose a Mach 2 oblique flying wing passenger transport [2]. With the critical antecedents facing these political and technological obstacles however, the undertaking of this even more daring concept, the oblique flying wing, was out of the question for the time being.

Meanwhile, engineers continued to work through the end of the 1950s to implement a working variable sweep wing into an operational aircraft. The F-111, which was the first production aircraft to incorporate variable sweep wings, was deemed to be a costly failure, and its inability to satisfy the Joint Services Requirements (TFX) of the Air Force and the Navy was in part due to the excessive structural weight of its complex swing-wing mechanism [3]. In the commercial sector, the variable sweep wings on the initial version of the Boeing 2707 supersonic transport was eventually abandoned due to the weight penalties associated with the design.

By the late 1960s, Grumman engineers had learned from the mistakes of the F-111 and succeeded in perfecting the technology with the F-14 – a supersonic interceptor that boasts a range unmatched by any modern supersonic fighter. But as the deficiencies faded with

the maturation of the concept, so too did the types of mission requirements that would justify the succession of the variable sweep wing (political). For this reason, almost all modern day supersonic fighters have fixed-sweep wings. This would later change with the emergence of a new kind of warfare.

In 1979, NASA Ames and Dryden undertook the experimental development of the first full scale obliquely-swept wing aircraft with wings which could be pivoted to angles of up to 60 degrees. Due to its unpleasant flying characteristics, which limited its promise for practical use, the aircraft was flown a total of only 79 times between 1979 and 1982 before being abandoned by its once-ambitious engineers [4]. Furthermore, aspects of the oblique wing which were of the most interest to engineers, such as its performance in the transonic regime could not be studied due to the low cost of the program and limited technical scope. Yet, the program was successful in exposing the major technical challenges that had to be addressed in subsequent programs, including the incorporation of aeroelastic tailoring and artificial stability augmentation to mitigate the adverse pitch-roll coupling.

So far, the OFW has been introduced solely as an aerodynamic concept. However, the author would like to point out that almost in parallel with the aerodynamic community's seemingly slow progress on the oblique flying wing has been the propulsion engineer's efforts to develop an efficient engine suited for such a supersonic transport. These include the supersonic high bypass ratio (HBR), supersonic through-flow fan (STF), and variable cycle (VCE) engines. These concepts have existed for some time, but without the commitment of the aircraft manufacturers to follow through with an SST development program, there has been very little motivation to do the same for an operational engine.

1.2 Fundamental Advantages

The attractiveness of the oblique flying wing as a passenger transport concept is rooted in the aerodynamic qualities of a variable sweep wing and structural characteristics of a flying wing.

- Minimal structural weight

- Minimal wave drag at supersonic regimes
- Minimal induced drag at all regimes

As with conventional symmetric flying wings, the absence of a concentrated load in the form of a fuselage minimizes the bending moments within the wing structure, and as a result, a commensurate reduction in structural weight can be achieved. Aerodynamically, the absence of a fuselage and the horizontal and vertical tail surfaces eliminates the parasite drag (profile and wave) sources that each of those components would otherwise contribute. Furthermore, the ability of the oblique flying wing to sweep its wing to that which is most suited for a particular flight regime minimizes the induced drag penalties associated with oversweeping a fixed-sweep wing. In general, the aerodynamic and structural benefits are manifested in the Breguet range equation by a high lift to drag ratio (L/D) and a low empty weight fraction (ef), respectively. Everything else being the same, an oblique flying wing will likely have a range longer than that of an equivalent conventional aircraft.

1.3 Fundamental Challenges

These advantages are not without their caveats. The oblique flying wing poses numerous stability, control, and aeroelastic challenges that must be dealt with in order to maximize its inherent advantages.

- Minimal stability
    - Dynamic coupling of axes
    - Low pitch moment of inertia
    - Low stability margin
    - Zero pitching moment criteria
- Aeroelasticity
- Low Internal volume/Excessive span necessary for commercial viability

Of the four unfavorable stability characteristics of the oblique flying wing, only the first is a consequence of the asymmetry. As demonstrated by the flight tests of the AD-1 oblique wing aircraft, this coupling is most prominent in the pitch and roll axes, whereby a pitch-up

command results in a left rolling moment, and likewise, a right roll for the opposite.[1] The latter three characteristics are, to an extent, attributes that are characteristic of all flying wing aircraft. However, unlike symmetric flying wings, whose incorporation of fixed sweep adds to the longitudinal static stability margin, such is not the case for an oblique flying wing. Furthermore, its low pitching moment is exacerbated by the requisite high axis ratio and zero fixed sweep. In fact, the very nature of symmetric sweep that provides favorable roll-yaw coupling for conventional aircraft precludes its use in OFWs since the aircraft must maintain near-zero roll trim irrespective of the oblique sweep angle.[2] Such a design, oblique or not, is often referred to as a "flying plank" since it lacks in almost all of the desirable stability characteristics of a flying wing [5].

One of the biggest obstacles that may hinder the realization of the OFW as a commercial transport is its large span when sized for passengers. Based on a simple three-step aircraft sizing example, one can easily demonstrate this fact.

1. Cabin height based on human occupants → airfoil thickness known
2. Specify the wing thickness to chord → chord falls out
3. Specify the planform aspect ratio → span falls out

For a nominal OFW with a 2m high cabin, a thickness to chord of 14%, and a modest aspect ratio of 8, this corresponds to an unswept span of approximately 400 ft – a size which modern airport facilities are not equipped to accommodate. The shear passenger capacity of such an OFW may prove to be a mismatch for the current passenger transport market, thereby precluding any chance of commercial viability.

Fortunately for proponents of the oblique flying wing, the emergence and accessibility of high-bandwidth control systems, aeroelastic tailoring, and unmanned aircraft technology may render these challenges to be somewhat obsolete.

---

[1] This is for the Kroo OFW configuration with the starboard wing swept forward
[2] All subsequent references to "sweep" will imply oblique sweep as opposed to inbuilt symmetric sweep

1.4 Current State of OFW Development

Recent developments in quiet supersonic flight and unmanned aerial vehicles have sparked renewed interest in oblique flying wings. The Quiet Supersonic Platform (QSP) program led by the US Defense Advanced Research Projects Agency (DARPA) in 2000 was an attempt to "develop and validate critical technologies for long-range advanced supersonic aircraft with substantially reduced sonic boom" characteristics [6]. It was found that geometric modifications to the nose section of an F-5E aircraft proved effective in mitigating the sonic boom-induced ground-level overpressures. From a commercial standpoint, the QSP program was the first step in overcoming what would otherwise be the proverbial political barrier to the development of a high speed civil transport (HSCT).

From a military standpoint, the introduction of UAVs and the corresponding removal of the pilot from the airframe conveniently and effectively eliminated the scaling problems as well. The drive has also been bolstered by operational necessity – the emergence of an ideal oblique flying wing mission which requires a strike aircraft to dash to the target at high speeds and subsequently loiter for an extended period of time ("hurry up and wait."). This multi-role capability is not so much crucial in a single mission as much as it is in a particular campaign, in which there is a need for "supersonic strike on day 1 of the war and long endurance loiter for popup targets on day 30" [7]. Indeed this type of warfare has become increasingly common, as confirmed by Desert Storm in the 90s and Operation Enduring Freedom in the present decade. In such cases, a homogenous fleet of a single type of aircraft has the potential to significantly lower the procurement and operational cost of a strike system.

In 2005, DARPA launched the "Switchblade" Program, which solicited the leading aerospace companies to build a small-scale supersonic oblique flying wing demonstrator with the following requirements (Taken word for word from reference [8]):

- *Non-expendable aircraft with a wheeled, retractable undercarriage for take-off and landing*
- *Air breathing propulsion*

- *Supersonic demonstration at a Mach number greater than or equal to 1.2*
- *Tailless configuration in supersonic cruise and subsonic loiter conditions*
- *Variable wing sweep demonstrated in-flight from a minimum wing sweep of not more than 30 degrees to a maximum wing sweep of not less than 60 degrees*
- *Aspect ratio greater than or equal to 7 at the minimum sweep condition*
- *Wingspan greater than or equal to 40 feet at the minimum sweep condition*

At the time of the writing of this thesis, various bidders in industry were working to promote their proposed design to a technology readiness level (TRL) of 4 or 5, with the ultimate goal of reaching level 7 necessary for consideration as a concept for future operational vehicles [9]. "This time around," as one Flight International columnist put it, "technical maturity and operational necessity might actually coincide [2]."

1.5 References to Related Literature

Once again, the reader has to her disposal, many papers that discuss the technical merits and challenges of the OFW – mostly from an aerodynamic, stability, and control perspective. Here, the author would like to provide a short list of references of what is by no means a comprehensive collection of oblique flying wing-related literature, but is a good starting point for the unacquainted.

In his 1992 Ph.D. thesis, Van der Velden [10] conducted a preliminary investigation of the oblique flying wing concept and its purported advantages by synthesizing a large-scale supersonic transport subject to all the current technical, environmental (NO_x), and operational (sonic boom) constraints. Van der Velden proposed that only after the economic viability of the oblique flying wing is realized could further research into the inherent stability and control problems be merited. It was concluded that in terms of operating costs, the OFW would only be superior to a conventional wing-body configuration if it is designed for more than 400 passengers, and preferably, for cruise at speeds of up to Mach 2.0. Also at Stanford, Morris and Kroo have addressed the OFW

from a structural, and stability and control point of view, with the latter work culminating in a flying OFW radio-controlled model in the early 1990s [11], [12], [13].

One will notice that as abundant as such literature is, virtually no attention has been paid to the propulsion aspects of the oblique flying wing and its related challenges, from a cycle, sizing or engine integration standpoint. Indeed, the oblique flying wing is the epitome of C.W. Miller's "Dream Airplane" for the aerodynamicist, [14] in which the priorities of the other disciplines have been pushed aside in favor of aerodynamic indulgence. The controls and propulsion engineer will especially agree that the OFW certainly provides no identifiable merits for their respective disciplines. It is interesting to note that contrary to the previous assertion, propulsion advocates will consider the OFW with pod-mounted engines to be the propulsion engineer's dream airplane, with it being nothing more than a flying engine with wings. Unfortunately for them, such is not the case when the task of submerging the engine into the airframe is introduced.

1.6 Thesis Goals

This thesis confronts issues that surprisingly little studies in the past have addressed – namely the question, "what happens when we size, design, and fit an engine into the oblique flying wing?" Since it was the author's intent to not reinvent what had already been investigated in past literature, this thesis borrows and combines effective synthesis methodologies from a number of sources that have already undergone repeated validation. (i.e. R.T Jones's linearized theory). Some of the more specific questions that this thesis ultimately sets out to answer include

- What are viable engine integration concepts for the OFW
- How does the OFW's aerodynamic characteristics affect the engine sizing criteria?
- What is the ideal engine cycle for any aircraft that is to fly in regimes which is most favorable for the OFW
- What are the aerodynamic penalties associated with pursuing this ideal cycle

- In terms of integrated mission performance, what is the best compromise for the engine cycle, sizing, and integration.

Before we can answer the above, we must answer some more fundamental questions that are not directly related to propulsion. They include

- At what flight regimes (altitude and speed) does the OFW provide the most operational benefit over conventional supersonic aircraft
- What are the aerodynamic characteristics at the critical design points (takeoff, transonic acceleration, and supersonic cruise), and how do they compare to a conventional supersonic aircraft
- With static stability in mind, how critical is the placement of subsystems and how is it a function of large scale geometric parameters (aspect ratio, wing loading)

Equations are worth a thousand words. The following outline establishes the mission performance as the figure of merit and reveals their dependence on mission parameters, and aerodynamic and engine performance.

Mission performance = f(mission parameters, aerodynamic performance, engine performance)

where,

- **Mission parameters** = (weight fractions, loiter time, segments)
  - Segments = (flight condition, distance)
- **Aerodynamic performance** = f(flight conditions, airfoil properties, large scale geometry, engine cycle(nacelle))
  - Flight conditions = (altitude, Mach, sweep, weight)
  - Airfoil properties = (CDpressure2D, CDfriction2D) = f(flight conditions, airfoil geometry)
  - Large scale geometry = (span, thickness to chord, aspect ratio, taper ratio, percent no taper)

- **Engine performance** = f(engine cycle, flight conditions)
    - Engine cycle = (bypass ratio, fan pressure ratio, compressor pressure ratio, combustor exit temperature, polytropic efficiencies, design point)

The aerodynamic performance estimation is carried out via the development of an aerodynamic synthesis model and its execution in Chapter 2. The effect of flight parameters on the aerodynamic efficiency, including altitude trajectory and sweep schedule will also be investigated later in the chapter. Likewise, Chapter 3 repeats a similar type of process for the performance estimation of a powerplant of a supersonic aircraft, with emphasis on cycle selection and its effect on nacelle wave drag. Chapter 4 presents a realistic strike mission (first bullet) and combines the results of the aerodynamic and propulsive analyses (second and third bullet) to estimate the range performance of three types of aircraft: the baseline OFW, a F-111, and a Concorde. Only in Chapter 5 are propulsion considerations unique to the OFW investigated—namely, engine sizing and physical engine integration.

At the end of this thesis, the functional relation established above will be reiterated, but with the independent variables either crossed out or ordered (left to right) to reflect its relative impact on the final figure of merit. Hopefully, this will provide a holistic perspective into what is important and what is not. Finally, the author would like to add that the focus of this thesis is not so much on the numerical results as it is on the methodology, with the hope that it will be of some value to those wishing to pursue OFW-related research in the future.

Chapter 2

Aerodynamic Synthesis

For the purposes of this thesis, the author would like to define a synthesis model as a combination of analytical (theoretical), parametric (historical), and computational methods that allow its users to simulate a complex system – in this case, the OFW aircraft. In doing so, one may not necessarily be able to predict quantitatively the actual behavior of the system, but at the least, observe qualitatively the individual effects that each independent parameter has on the system and its subsystems. As outlined in the thesis goals in Section 1.6, the final objective of this thesis is to shed light on the mission performance of the OFW as a function of the aerodynamic and propulsive decisions that the aircraft design engineer makes. A block diagram that illustrates the parametric flowdown for each synthesis model is presented in Appendix A.

2.1 Geometric Model

It seems reasonable to begin the synthesis by defining an OFW geometry that all subsequent synthesis models can refer to. Unfortunately, each of the aerodynamic synthesis sub-models function under their own unique geometric assumptions, and as a result, requires three separate and convenient geometries. This section will provide a brief summary of those three geometries – the linear, elliptic, and section-oriented geometries.

2.1.1 Linear Model

The linear model assumes a linear, constant-taper wing with an inboard constant-chord section. The wing thickness is assumed to taper such that the wing thickness to chord ratio remains constant.

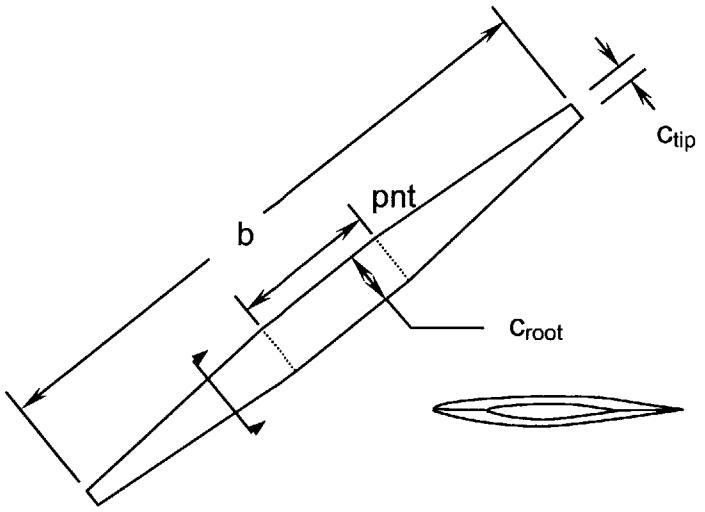

Figure 2.1: Linear model and its geometric definitions

2.1.2 Elliptic Model

For reasons explained in Section 2.2.2, the optimal OFW geometry from an aerodynamic standpoint is one with an elliptical planform and a parabolic thickness distribution in the spanwise direction [15]. Contrary to the linear model, the thickness to chord ratio does not stay constant across the span. Incidentally, this elliptical planform is the optimal geometry for a lifting line that is to be constrained within the parallelogram ABCD.

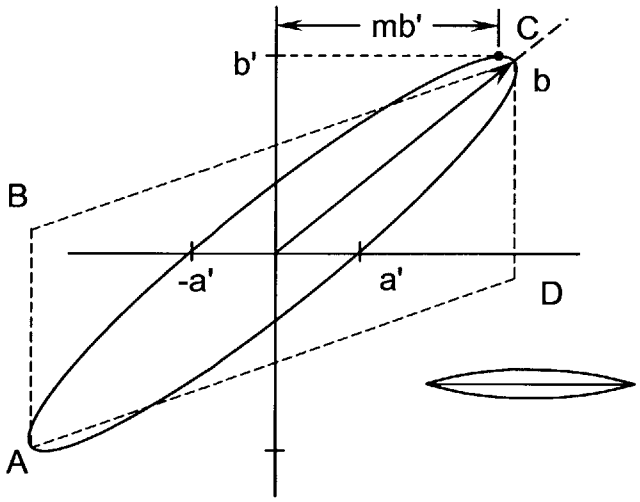

Figure 2.2: Elliptic model and its geometric definitions (adapted from [15])

2.1.3 Section Model

For the purposes of estimating the profile drag characteristics unique to a particular 2D airfoil, we now model the OFW as a swept constant chord wing of particular section geometry and of infinite span.

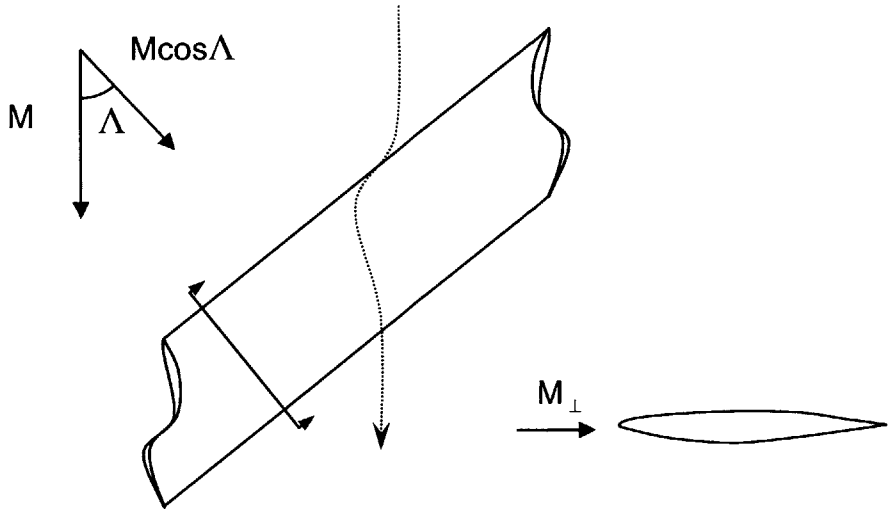

Figure 2.3: Infinite span, constant chord model and its streamline trace

2.2 Aerodynamic Model

The synthesis model makes uses of RT Jones's linearized theory for the estimation of volume and lift-dependent wave drag; classical aerodynamic theory for induced drag; parametric estimation for form drag of isolated components; and a coupled inviscid-viscous 2D code, MSES for profile drag. Linear independence of the four main types of drag is assumed such that the total drag is simply their superposition. Of the four methodologies enumerated above, the classical and parametric are those that, for example, are widely used in industry during the preliminary stages of a design. An example of such would be the estimation of undercarriage drag by cross referencing a table of form factors. Since confidence in the fidelity of these methodologies is assumed, the author will forgo detailed explanation of such related theory. The author recommends Raymer as a source for further information on related topics [16].

2.2.1 Drag Bookkeeping

Because of the confusing and sometimes conflicting nomenclature in accounting for the various sources of drag, it is worthwhile to briefly describe the drag classifications and their hierarchy. Here, the author recommends Dragbusters [17] and once again, Raymer for effective graphical representations of the drag breakdown.

2.2.2 Linearized Potential Theory

In 1918, Prandtl demonstrated that an elliptical lift distribution minimizes the vortex drag of a finite span wing, and that it could be achieved through planform tailoring, wing twist, or spanwise section variation [18]. In terms of supersonic aerodynamics, Sears and Haack noted in 1947 that there exists an ideal volume distribution for an object of given length that would minimize its volume dependent wave drag [19]. This distribution would later be named the Sears-Haack area distribution. With the above two facts known, it was in 1961 that Smith discovered the ideal OFW geometry by noting that the Sears-Haack area distribution could be decomposed into an elliptical distribution in one dimension and a parabolic in another such that it would simultaneously minimize the induced and wave drag contributions [20]. The uniqueness of this particular ellipsoid is that its area projection in any Mach plane is elliptical, thereby making it the most effective geometry for minimal wave drag at *every* Mach number.

Following M.N. Kogan's suggestion that the wave drag of a uniformly loaded elliptic wing could be calculated by simply factoring the induced drag by the axis ratio of its characteristic trace, Jones derived the following expression for the wave drag of an OFW lifting line [15].

$$C_{Dw,l} = K_w \frac{\beta^2}{2\pi d^2} C_L^2 S_{ref}. \tag{2.1}$$

Here, the drag due to lift term, K_w is minimum for a uniformly loaded elliptical wing, and can be expressed as follows [10]:

$$K_w = \frac{2}{\beta^2}\left[m'^2 + \frac{a'^2}{b'^2}\right]\left[\frac{b'}{a'}\Re\sqrt{\beta^2 - \left(m' + i\frac{a'}{b'}\right)^2} - 1\right]. \tag{2.2}$$

where the primed variables are dimensions in the streamwise coordinate system and can be expressed in terms of the unswept dimensions.

$$\begin{aligned} m' &= \frac{(b^2 - a^2)\sin\psi\cos\psi}{b'} \\ a' &= \frac{ab}{b'} \\ b' &= \sqrt{a^2\cos^2\psi + b^2\sin^2\psi} \\ \beta &= \sqrt{M^2 - 1} \\ \psi &= \frac{\pi}{2} - \Lambda \end{aligned} \tag{2.3}$$

In 1961, J.H.B Smith carried out a similar derivation for the wave drag contribution due to the volume of an oblique ellipse.

$$C_{Dw,v} = \left(\frac{t_o}{a}\right)^2\left(\frac{b'}{b}\right)^2\Re\left\{\frac{\beta^2 - (m' + in)(m' + 2in)}{\left[\beta^2 - (m' + in)^2\right]^{3/2}}\right\}. \tag{2.4}$$

The aforementioned analyses are based on linearized theory, they become inapplicable as Mach approaches unity. Furthermore, experimental measurements of wave drag on a Sears-Haack body have revealed the actual drag to be up to twice that dictated by the supersonic area rule. Similar discrepancies can be expected for an oblique ellipse geometry, whose theoretical methods are based on the same principles. Later, the synthesis model makes a reasonable correction by multiplying the theoretical wave drag solution by an appropriate scaling factor (~2).

Jones also provides a single analytical expression that encompasses both lift-dependent drag terms, including the induced and wave due-to-lift contributions.

$$C_{Di} + C_{Dw,l} = \frac{C_L^{\,2}}{4} \Re \sqrt{\beta^2 - \left(m' + i\frac{a'}{b'}\right)^2} \,. \tag{2.5}$$

This expression may be suitable for design point operation at supersonic speeds where linearized theory holds, but not necessarily so for subsonic off-design performance.[3] For those regimes, it would be better to consider the induced drag contribution separately via classical aerodynamic theory. Namely,

$$C_{Di} = \frac{C_L}{\pi AR e} \,. \tag{2.6}$$

Which, if we write in terms of normal components, becomes

$$C_{Di} = \frac{C_l^2 \cos^2 \Lambda}{\pi \sigma e} \,, \tag{2.7}$$

where,

$$\begin{aligned} C_l &= \frac{C_L}{\cos^2 \Lambda} \text{ and} \\ AR &= \sigma \cos^2 \Lambda \,. \end{aligned} \tag{2.8}$$

Here, the "effective" aspect ratio decreases with increasing sweep and is proportional to the fixed, unswept axis ratio. It is later revealed that the best L/D is typically achieved by flying an altitude, Mach, and sweep trajectory such that the normal component of the lift coefficient, C_l, is fixed at that which is best for the particular airfoil section. For the nominal quasi-optimized section used in this study, this corresponds to a C_l of about 0.6. With this in mind, the benefit of writing the induced drag term as such is evident. That is, the minimum achievable induced drag increases with the square of sweep. If we assume a sweep schedule such that the normal component of the Mach stays constant as well, then we can write the sweep angle as follows:

[3] Previous literature would have considered subsonic regimes to be off-design, but that notion may be a misnomer in this study since for example, a single OFW may be designed for subsonic loiter equally as well as for supersonic cruise

$$\Lambda = \cos^{-1}\left(\frac{M_{\perp}}{M_{\infty}}\right), \tag{2.9}$$

where, $M_{\perp}$ is typically slightly less than the critical Mach number of the airfoil section. Substituting equation 2.8 into the previous form of the induced drag equation, we can write the expression in terms of the flight Mach number, Minfinity.

$$C_{Di} = \frac{(M_{\perp} C_l)^2}{M_{\infty}^2 \pi \sigma e}. \tag{2.10}$$

From equation 2.10, it is evident that although higher sweep angles decrease the effective aspect ratio, the net effect as one increases the flight Mach number is a reduction in induced drag.

2.2.3 Computational Methods

Previous graduate work at MIT such as those by Butler [21] yielded a quasi-optimized OFW section geometry that maximizes the figure of merit of interest (range parameter), while at the same time, conforming to "user specified" geometric constraints. User specified constraints are those whose absence would otherwise allow such solutions as infinitely thin cross sections with zero bending stiffness. The author considers these airfoils to be quasi-optimized since such a generic multi-regime airfoil is the best one can do without further constraining the design space (i.e. flight speed, maximum span, passenger capacity).

Because of the uniqueness of these OFW-specific airfoils, there are no existing lift and drag polars available from which to extrapolate the profile drag in the flight regimes of interest. For the case of the OFW, the relative magnitude of the pressure and friction drag terms compared to the other virtually non-existent drag terms makes its fidelity all the more important. The proposed solution process involves the coupled inviscid viscous CFD code, MSES and is as follows:

1. At a reference Reynolds number, compute the 2D profile pressure and friction drag coefficients for the OW4 airfoil at a range of normal Mach numbers and normal lift

coefficients. From these outputs, construct a two-dimensional lookup table as a function of $M_\perp$ and C_l. This obviates the time consuming process of having to execute a separate MSES routine in conjunction with each execution of the synthesis code.

2. For each user specified flight condition, extrapolate the two profile drag terms from the lookup table.
3. Based on the actual Reynolds number for the particular OFW geometry and flight regime, apply a correction factor to the profile drag.
4. Calculate the streamwise (3D) component of these drag contributions.

The Reynolds number correction in step 3 was proposed by Kroo et al in reference [22].

$$c_f \sim C.F.[\log_{10} \mathrm{Re}]^{-2.58}, \tag{2.11}$$

where the correction factor C.F. can be written empirically as a function of M,

$$C.F. = 1.002929 - 7.220527\times10^{-2} M - 3.063979\times10^{-2} M^2 4.52067\times10^{-3} M^3, \tag{2.12}$$

and the Reynolds number is based on 80% of the streamwise chord length.

The net profile drag, which points in the direction of the unswept aircraft axis, can be resolved into components parallel and normal to the flight direction. Here, the side force arising from the normal drag component, by convention, does not contribute to any performance degradation, but must be offset either by yaw trim or thrust vectoring if one is to maintain zero sideslip. Butler proposes that for bookkeeping purposes, the reduction in useful thrust as a result of canting the engine to the side be equated to an equivalent increase in total drag [21].

For a swept constant chord wing, Drela [23] writes the friction and pressure drag forces in terms of the normal-section drag terms as follows:

$$\begin{aligned} D_f &\cong D_{f\perp}/\cos^2\Lambda \\ D_p &\cong D_{p\perp}\cos\Lambda \end{aligned}, \tag{2.13}$$

Here, the shear forces are assumed to point roughly in the streamwise direction and to be proportional to the free stream Mach rather than the normal Mach. Normalizing these drag forces by the streamwise dynamic pressure and reference area yields in the equivalent 3D profile drag coefficients.

$$C_{Df} = c_{df}$$
$$C_{Dp} = c_{dp} \cos^3 \Lambda \tag{2.14}$$

2.3 Results and Model Verification

Before proceeding with the rest of the mission synthesis model, we will discuss the aerodynamic characteristics of the OFW and verify the results of the aerodynamic model by comparing its results to those of existing supersonic aircraft. Here, in addition to specifying a baseline OFW geometry, we must also define a flight trajectory for the OFW to fly for each of the synthesis cases. Here, the flight trajectory will be defined as the altitude and sweep angle that is to be sought for each flight Mach number. Possible altitude trajectories include constant altitude, constant C_L, constant C_l, and best L/D trajectories. The sweep schedule can be such that it achieves best L/D or maintains constant $M_\perp$, and can also be bounded by a minimum and maximum allowable sweep.

2.3.1 Optimal Altitude Trajectory

Drela proposes that for minimum total drag, the trajectory should be flown such that the airfoils operate at their best section lift coefficient and perpendicular Mach number, which, for the baseline OW4 section, is about C_l =0.6~0.7 and $M_\perp$=0.70~0.75, respectively [23]. To verify this assumption, L/D was plotted as a function of Mach number for each of the aforementioned trajectories.

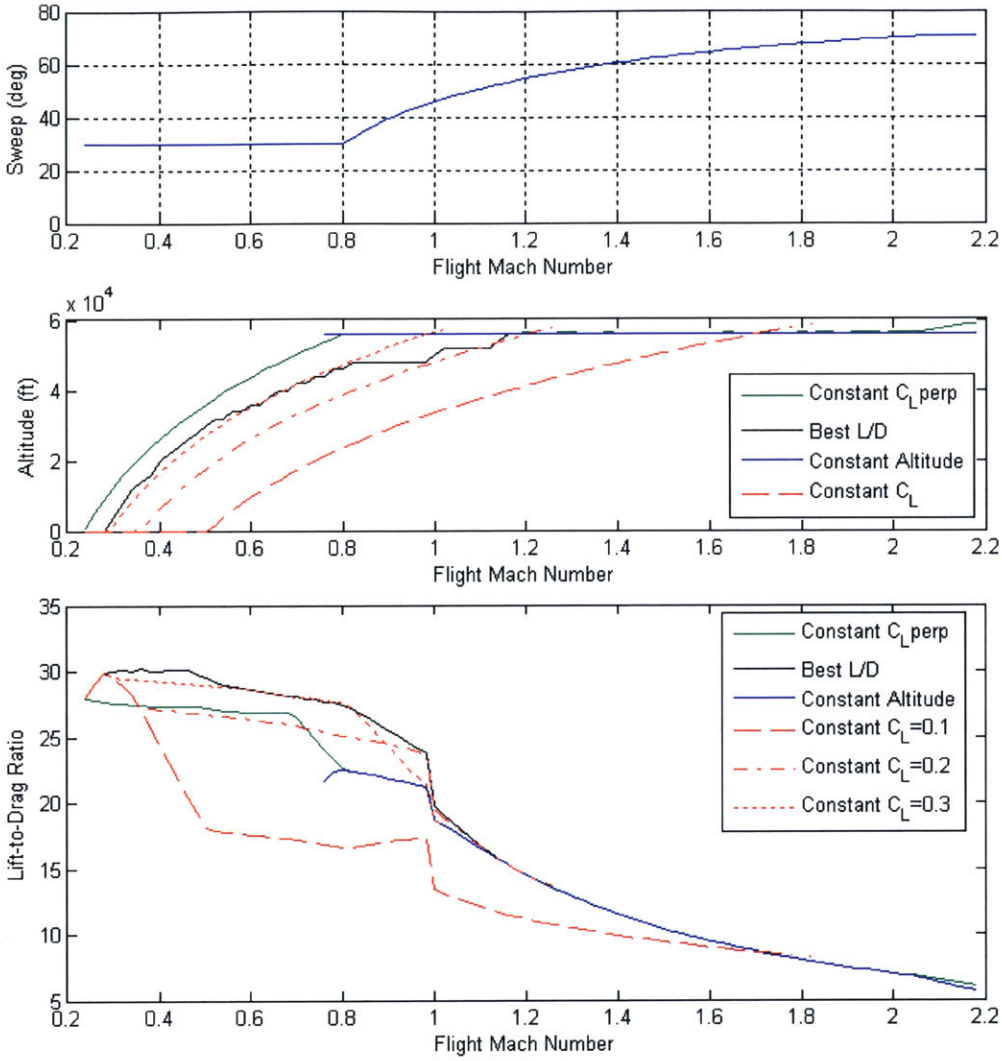

Figure 2.4: Overall lift-to-drag ratios along various flight trajectories

In each of the cases, the sweep schedule maintains a minimum sweep angle of 30 degrees until the critical normal Mach number limit necessitates further sweep, at which point, the wing sweeps such that the normal Mach would match the critical value. If we neglect changes in the wing loading due to fuel burn, then for fixed C_L or C_l, the aircraft must maintain constant dynamic pressure by flying at higher altitudes for higher Mach. The result is an ambient pressure requirement that is inversely proportional to the square of the Mach, which, given the exponential characteristic of the atmosphere, yields an altitude trajectory which is a logarithmic function of the square of the Mach number.

From Figure 2.4, it is evident that in terms of achieving best L/D, a constant C_L=0.3 trajectory is optimal for Mach numbers less than unity. Above that speed, the OFW is unable to maintain the specified C_L since the advancing sweep 'loads up' the wing to the point where C_l exceeds that of stall. In Figure 2.4, that limit coincides with the location where the respective lines terminate. With that in mind, it is evident from the figure that trajectories that maintain a lower C_L can fly faster without straying out of the feasible operating range (red dashes). For those trajectories, however, the L/D for most of the subsonic Mach number range is considerably lower than what is ideally achievable (black line).

Past the transonic regime, all altitude trajectories converge to the user specified design altitude of 56,000 ft, which in this case, is the optimal altitude for an OFW with a wing loading with 38 psf. In general, a higher wing loading tends to drive the design altitude lower for most transport aircraft (100 psf for cruise at 40,000 ft). Here, the design altitude will be defined as that which yields a C_l that maximizes the *section* L/D. Again, because of the dominance of the profile drag over other drag sources, it is assumed that best *overall* L/D will also be achieved near this flight condition. Hence, in the supersonic regime where $M_\perp$ and C_l are held fixed due to the sweep scheduling and the best L/D criteria respectively, the design altitude remains fixed, independent of Mach number. In conclusion, the ideal trajectory is one which maintains a constant C_L up to a critical Mach—unity in this case—and subsequently transitions to one of constant C_l.

2.3.2 Sweep Angle Limits

Upper and lower bounds on sweep angle are also imposed based on what is realistically feasible in terms of controllability, and desirable in terms of propulsion integration. A realistic upper limit of 70 degrees—established by stability and control considerations in [4]— marks the point where any excess sweep results in the three-dimensional spanwise component of the flow to dominate over the normal component.

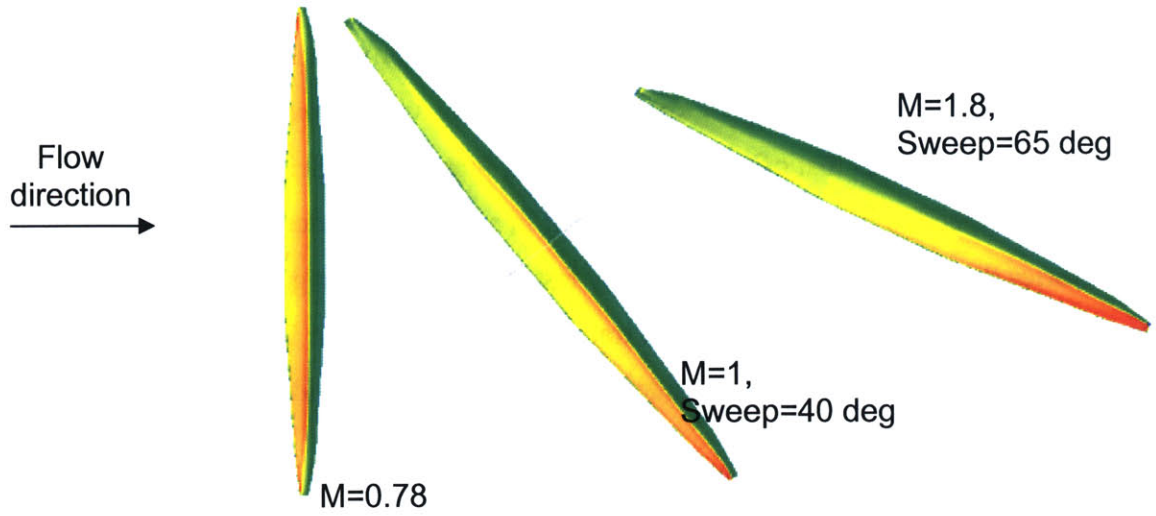

Figure 2.5: Surface Mach number contours provided by 3D Euler calculations (Courtesy of A. Merchant)

The result is a gross asymmetry in the flowfield between the upwind and the downwind wing section in which the strength of the local shocks on the suction side of the wing vary considerably along the span of the aircraft – stronger towards the downwind side and weaker towards the upwind. In locations where the normal component of the flow is already close to the limit for acceptable transonic performance ($M_{\perp,max}$~1.15), this spanwise variation may force the cumulative shock losses to exceed acceptable levels. This, combined with the decreased projected frontal area of the control surfaces will certainly exacerbate the existing lateral controllability issues. As evident from the geometry in Figure 2.3, the current model assumes uniform flow down a wing of infinite span and therefore breaks down when such flow interactions exist. It is for this same reason that OFWs with very low aspect ratios (~4) cannot be evaluated with the current method.

Whereas the upper limit to the sweep is almost certainly an inevitability, the lower limit is a negotiable concession in which low-speed loiter performance can be sacrificed at the expense of propulsion system conformity. The practical benefits of limiting the minimum sweep to a nonzero value will be discussed in detail later in the propulsion integration section—in short, it reduces the range of sweep angles that the propulsion system must

sweep across throughout its entire flight. In addition, takeoffs, landings, and ground operations in non-zero sweep configuration will alleviate some of the dimensional constraints for large 500-passenger scale OFWs that cannot otherwise be accommodated at modern airport facilities. However, this comes at the expense of takeoff field length, as is shown in Section 5.1.3.1.

Most notably, setting an upper and lower bound to the sweep has a negative effect in the aerodynamics in that it further constraints the operating envelope of the OFW. Figure 2.6 is a plot of maximum achievable L/D as a function of flight Mach for three separate sweep limiting cases. The termination of the line on the left marks the stall limit whereas the single terminating point on the right marks the flight Mach number at which sweep in excess of 70 degrees will be required in order to keep the OW4 airfoil within the limits of acceptable 2D transonic performance ($M_{\perp} < 0.75$).

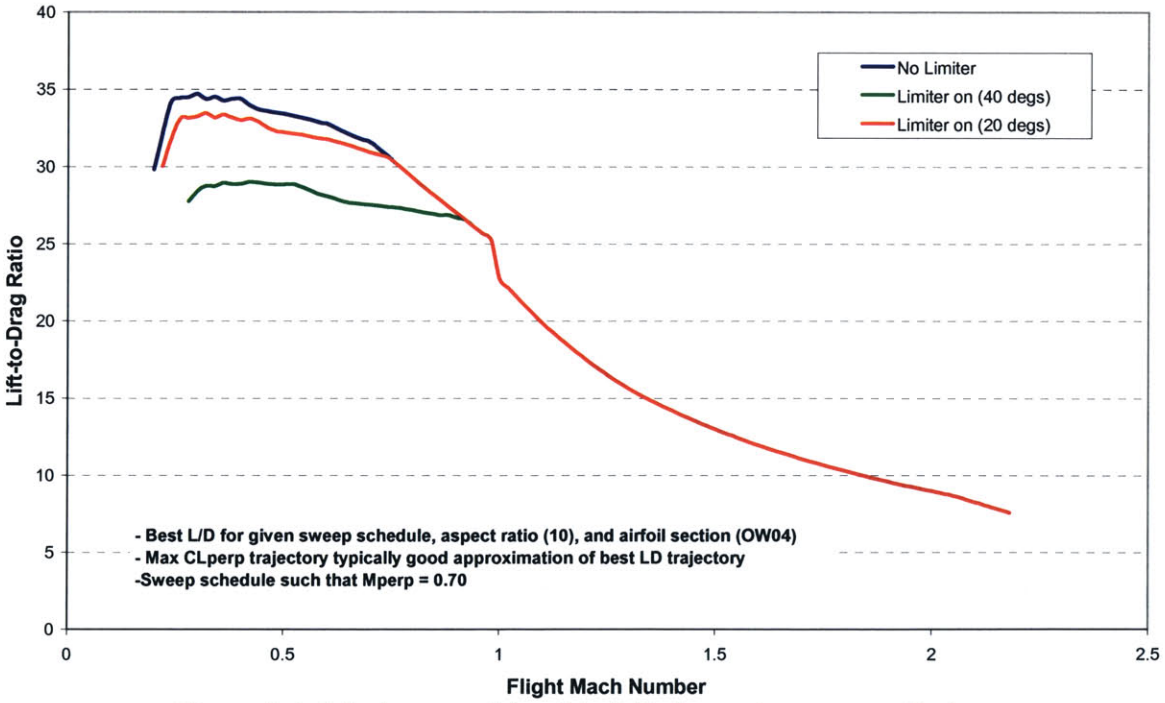

Figure 2.6: Maximum achievable L/D for various sweep limits

2.3.3 Optimal Sweep Schedule

It has been proposed that for any fixed cruise Mach number, optimal L/D is achieved by sweeping the wing such that the section operates at a perpendicular Mach and C_l for best *section L/D* (that which only takes into account the profile drag calculated by MSES). Typically, this optimal section Mach lies slightly below the critical Mach number and, aside from the geometry of the airfoil, is mostly a function of the section C_l—higher for low C_l and vice versa. If sweep is to be limited to within 70 degrees at cruise conditions, then it is desirable to operate at the highest possible perpendicular Mach, and subsequently find the highest achievable C_l that corresponds to that Mach.

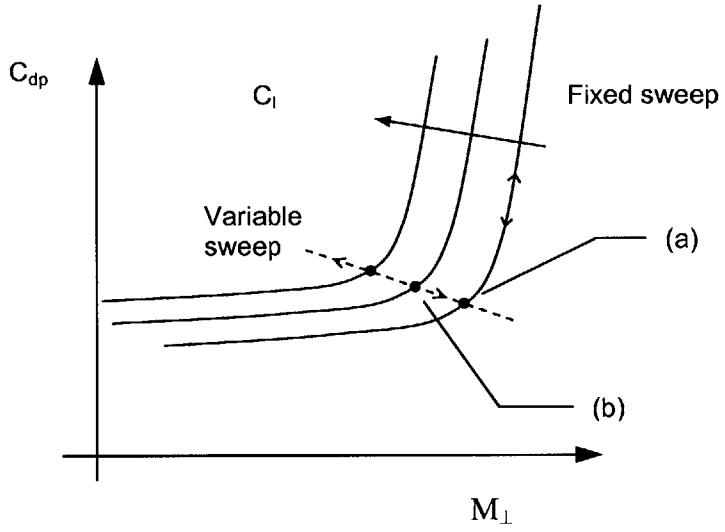

Figure 2.7: Optimal sweep scheduling

For the baseline OW4 airfoil, this design operating point is at a $M_\perp$ of 0.70 and a C_l of 0.6, as denoted by point (a) on Figure 2.7. It was presumed that the total OFW drag is minimized at sweep angles that correspond to this operating point, with an overswept wing paying the penalty with respect to induced and profile drag, and an underswept wing with respect to wave drag. Surprisingly enough, this was shown not to be the case when L/D was plotted as a function of sweep angle for lines of constant Mach and altitude (Figures 2.8 and 2.9 below). In fact, the optimal sweep angles were found to be higher than that dictated by the $M_\perp$=0.75 sweep schedule proposed earlier, implying that by oversweeping the wing, the wave drag reductions outweigh the induced and profile drag penalties to yield

a net positive effect on overall L/D. This new operating point is indicated on Figure 2.7 as point (b), and corresponds to a nearly-constant $M_{\perp}$ of about 0.6. Unfortunately, oversweeping the wing is expected to introduce challenges in yaw-control that would otherwise not be present for a nominally swept wing. In fact, sweep angles optimal for cruise at 56,000 ft are inadvisable for Mach numbers above 1.6, and almost prohibitive for cruise at lower altitudes (20,000 ft).

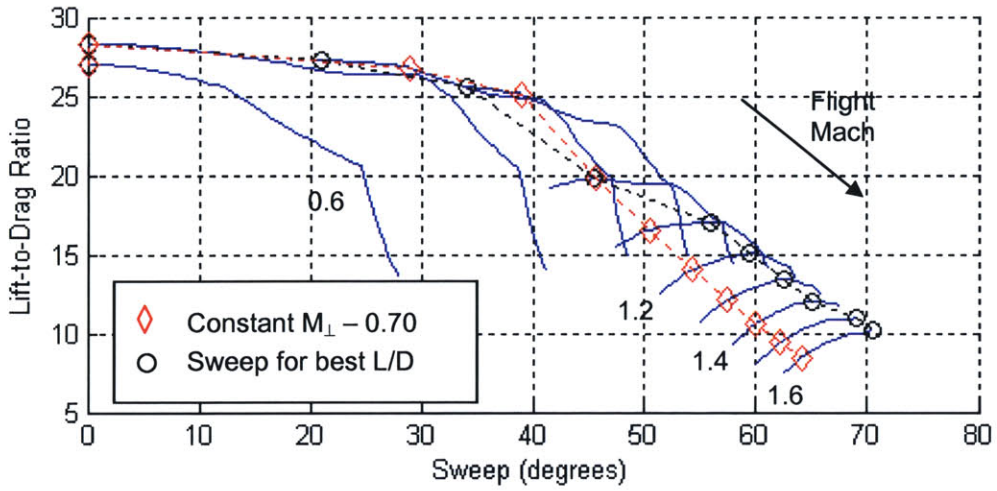

Figure 2.8: Sweep schedule and its effect on lift-to-drag ratio (56,000 ft; W/S = 38 psf)

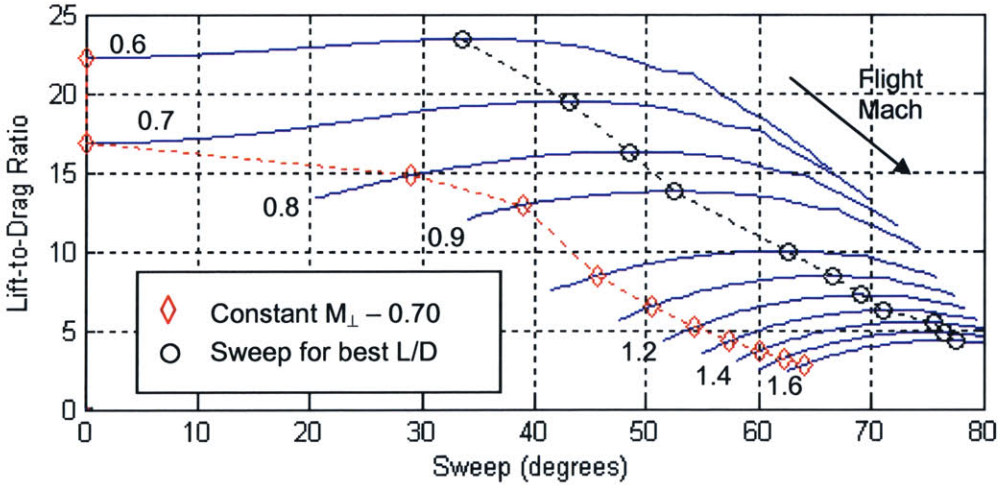

Figure 2.9: Sweep schedule and its effect on lift-to-drag ratio (20,000 ft; W/S = 38 psf)

2.3.4 Drag Comparison

For most aircraft, the parasite drag accounts for most of the aircraft drag at cruise conditions, and its minimization is especially critical for good supersonic performance. Figure 2.10, adopted from Raymer [16], plots the parasite drag as a function of Mach number for an OFW with t/c=0.12, and AR=10 and compares it against those of older generation subsonic and supersonic aircraft. The parasite drag distribution is lower by on average, about 15 counts than that of the XB70 bomber, which also benefits from then-ground-breaking- developments in area ruling and the minimal wing area thanks to an innovative compression-lift scheme. Its lift dependant drag characteristics (vortex and wave due to lift), however, are not expected to be as stellar as that of the OFW, and its inferior L/D reflects the higher total drag.

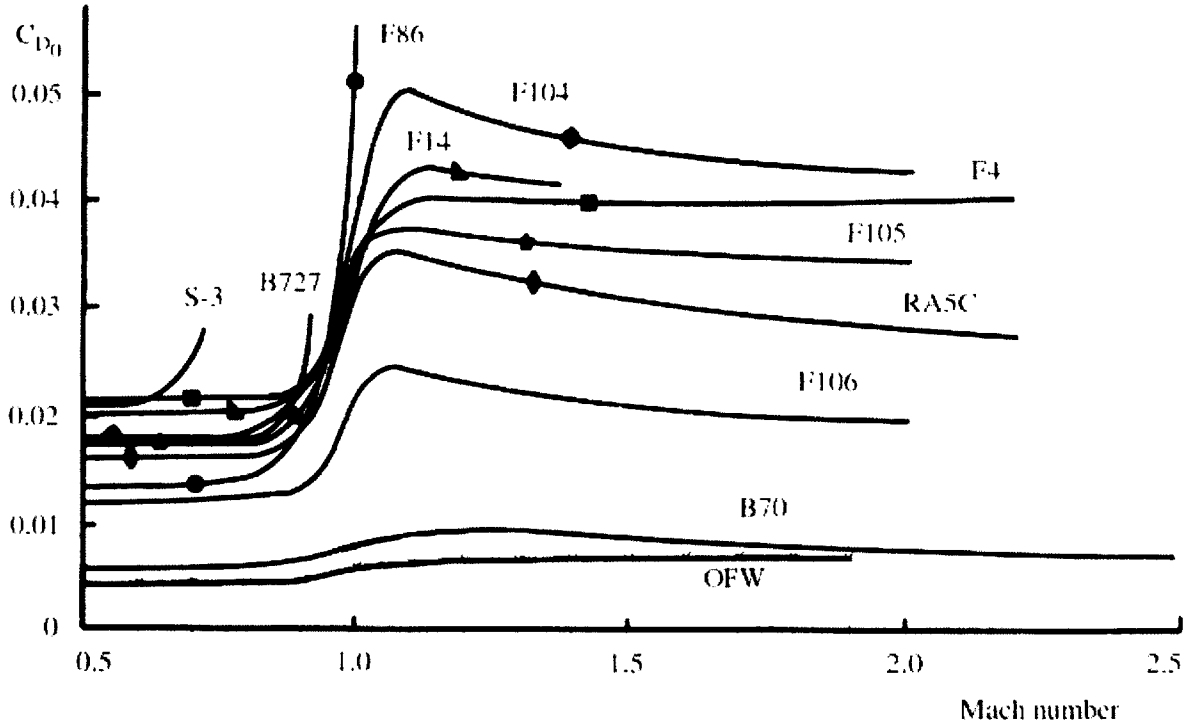

Figure 2.10: Parasite drag rise comparison (adapted from Raymer [16])

2.3.4.1 Transonic Drag Rise – Why the OFW is so Special

According to F.T. Lynch, at drag divergence for most supersonic aircraft, "the additional transonic drag is approximately evenly divided between the explicit shock drag and the shock induced additional profile drag [24]." The explicit wave drag can be attributed to such things as bow shock formations near the nose cone of similar non-lifting bodies, whereas the "shock induced" drag can be attributed to the formation of strong shocks on the suction side of lifting surfaces. For the OFW, one will note the absence of the characteristic dip in parasite drag following the transonic drag rise. Here, if we consider the transonic drag rise to be the superposition of two types of additive drag sources—the explicit and profile, as explained above and as shown in Figure 2.11—the reason for the trend becomes evident. With the normal Mach number held below the critical value at all flight Mach numbers, the OFW never experiences any additive profile drag that typically results from penetrating the transonic regime at fixed sweep (middle diagram in Figure 2.11). To a lesser extent, such is also the case for other symmetric variable sweep aircraft, such as the F-111 and F-14.

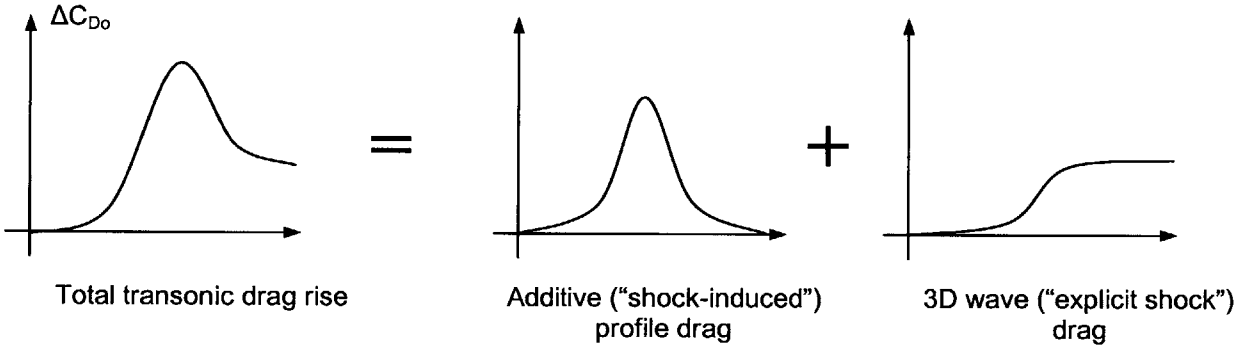

Figure 2.11: Decomposition of the transonic drag rise

2.3.4.2 Comparison Between Theoretical and Experimental Results

Wind tunnel experiments carried out by Whitcomb in 1952—although validating the benefits in transonic area ruling—also revealed the discrepancy between the measured and theoretical trends in the transonic drag rise. Figure 2.12 illustrates such a discrepancy for a smooth area-ruled volume, not unlike that of the OFW. One can see that contrary to the

drag jump in the theoretical result, much of the actual drag rise takes place well after the transition past sonic, and is thus lower than that dictated by theory for Mach numbers in this vicinity ($1.0 < M < 1.1$). Although this smoothing was performed manually in the parasite drag plot in Figure 2.10, such manipulations cannot be carried out practically for each synthesis run. Here, the only recourse is to present a disclaimer such that we hold suspect all future synthesis results in this Mach regime.

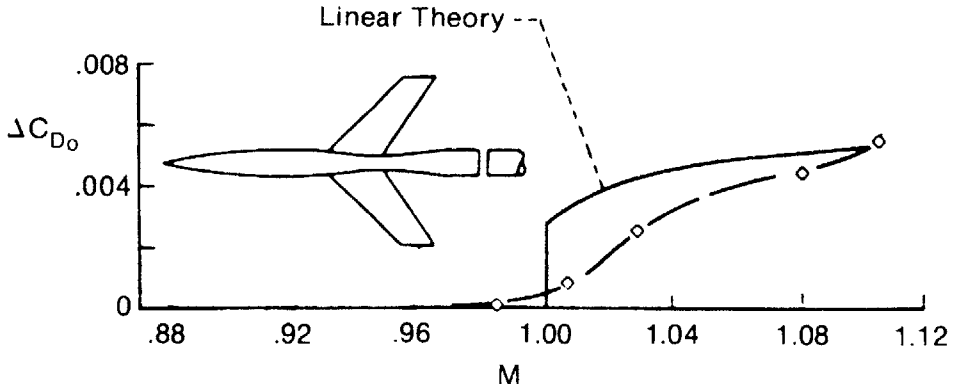

Figure 2.12: Transonic drag rise comparison between theoretical and measured values [15]

2.3.4.3 Comparison with Concorde

Figure 2.13 compares the drag breakdown of the baseline OFW and a Concorde as a function of flight Mach number. Whereas the OFW breakdown was constructed for a constant C_L trajectory, the published Concorde drag breakdown is expected to be at altitudes and values of C_L that correspond to a typical flight plan [25]. For all flight regimes except takeoff, any C_L mismatch between the OFW and the Concorde is not expected to significantly affect the drag breakdown since the lift-dependent drag contributions are dominated by the other drag terms and hence, not expected to significantly influence the total drag. Once again, as was illustrated in Figure 2.10, the characteristic transonic drag rise and its accompanying post-transonic drag bucket is absent on the OFW. Friction drag also contributes a larger percentage of the total drag on the OFW because of the large wetted area-to-volume ratio of the OFW.

Figure 2.14 is a contour plot of the ratio of drag coefficient between the OFW and the Concorde, with colder colors indicating flight regimes for which the OFW drag is substantially lower than that of the Concorde. Since the wing loadings of the two aircrafts being compared have been matched (common C_L at each operating point), the inverse of the contour variable can also be interpreted as the L/D ratio between the two aircraft. Subsonic flight at high-altitude and low-supersonic flight across all altitudes are two regimes for which the OFW is particularly attractive. The OFW's ability to unsweep at low speeds explains why this is so for subsonic high altitude flight. Likewise, the absence of the shock-induced additive profile drag explains low drag at transonic speeds. Note that this disparity diminishes as the flight Mach is increased – to about 0.7 for M2.2. Although this ratio tends toward unity for even higher Mach, there is no reason to believe that at any point, the Concorde will surpass the OFW in terms of L/D.

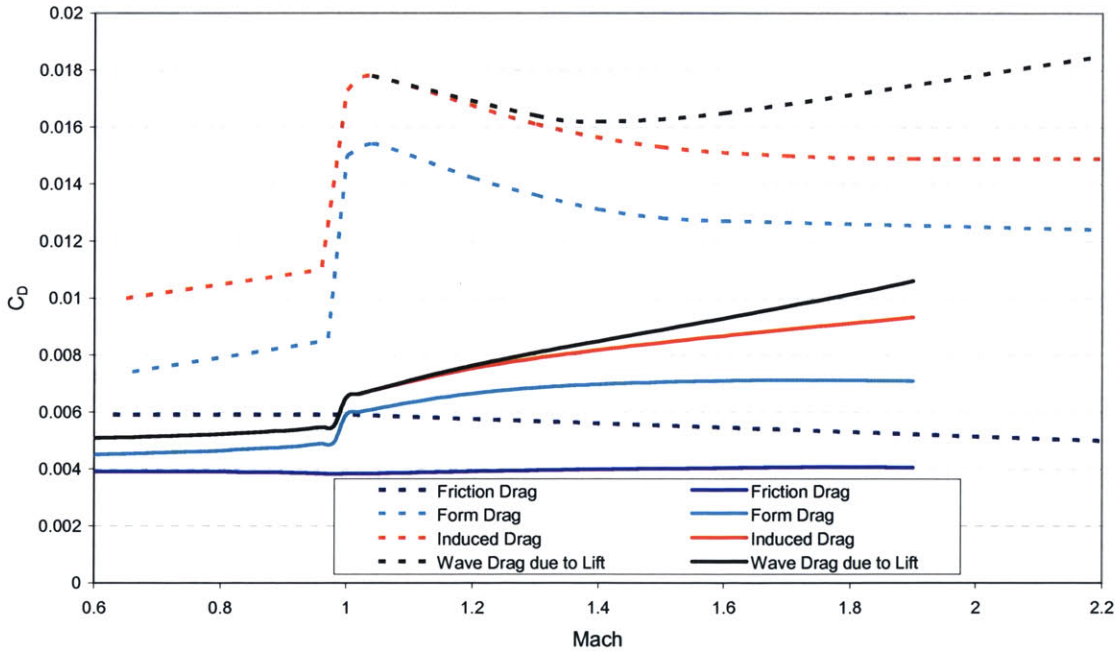

Figure 2.13: Drag breakdown comparison between OFW and Concorde

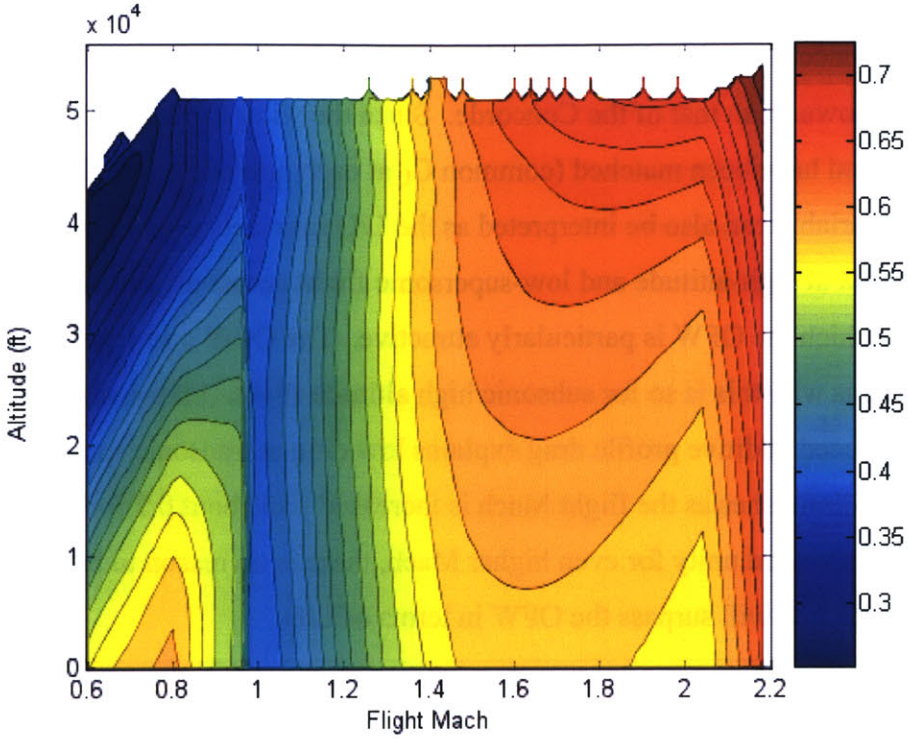

Figure 2.14: OFW-to-Concorde drag ratio for identical W/S (50 psf)

Chapter 3

Propulsion Synthesis

The mission performance and operability of a supersonic aircraft is highly sensitive to the engine cycle selection and its sizing criteria due to the fact that the performance disparity between two arbitrary cycles tends to widen as one increases the operating Mach number. In this thesis, the term, "propulsion selection" is used as a catch-all phrase for all the propulsion-related decisions that the aircraft design engineer is to make, including engine cycle selection, engine sizing, and engine integration. Although each decision is highly dependent on one another, this thesis will initially consider each of them independently and in that aforementioned sequence by adopting a rubber engine and aircraft model.
The purpose of this section is to find the most suitable cycle for any supersonic aircraft that is to have range as one of its primary metrics, with emphasis on the cumulative performance of the engine once nacelle drag is taken into account. That being the case, engine sizing and integration will be neglected for now, as they depend on the drag characteristics and geometric constraints unique to the OFW. Later in Chapter 5, *propulsion selection* will be revisited via a more holistic approach so as to integrate all of the aerodynamic, propulsive, and geometric considerations.

3.1 Aero-Propulsive Modeling

With the assumption that the OFW's primary role is that of a long range supersonic platform, thrust specific fuel consumption (TSFC) was selected as the primary metric for cycle selection, with thrust lapse and specific excess power given secondary considerations. To the second order, the cycle also affects the geometry of the engine, and therefore becomes critical for platforms which have dimensional constraints if one is to keep the

engine count low. It will be later revealed that the OFW is a platform with especially restrictive dimensional constraints.

3.1.1 Aero-Propulsive Performance Bookkeeping

In terms of cycle, this thesis hypothesizes that since TSFC favors low specific thrust, and installation drag and weight favors the opposite, there exists an optimal cycle that maximizes the overall mission performance (range parameter). By convention, such tradeoff is usually carried out by the balancing the propulsive, aerodynamic, and weight terms in the Breguet range equation such that each discipline can be given (or deducted) appropriate credit for fulfilling (or falling short of) their respective performance requirements. In this thesis, however, the aerodynamic penalties attributed to the installation of a propulsion system will be accounted for with a reduction in the uninstalled TSFC, with what will be referred to as a "reduced TSFC," and engine weight considerations will be ignored. Readers may note that this is analogous to the modeling of propeller scrubbing losses with what is referred to as "reduced thrust."

$$TSFC_{red} = \frac{T - D_{nac}}{\dot{m}\, f}. \tag{3.1}$$

The range parameter can now be written in terms of an aerodynamic efficiency term independent of the propulsion system.

$$R.P. = \frac{M}{TSFC}\left(\frac{L}{D}\right)_{inst} = \frac{M}{TSFC_{red}}\left(\frac{L}{D}\right)_{const}. \tag{3.2}$$

3.1.2 Engine Cycle Modeling

The engine modeled is a single-spool, mixed-flow turbofan with the following station designations:

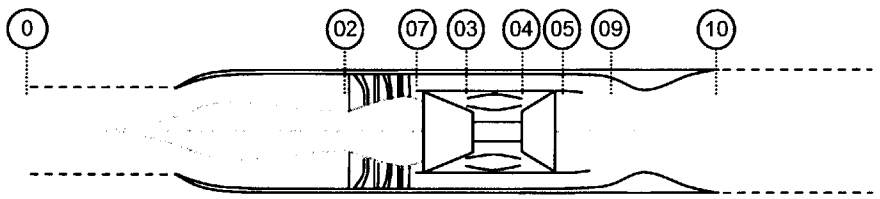

Figure 3.1: Station designations of a single-spool, mixed-flow turbofan

Two types of cycle analyses are implemented—one in which GasTurb [26] is used to obtain the off-design performance of the engine at user specified flight conditions, and another in which a continuous on-design condition is maintained for the purpose of estimating the nacelle wave drag. The proceeding discussion of the assumptions pertains to the latter objective.

The flow properties through the gas generator are calculated with steady, quasi 1-D cycle analysis methods detailed in [27], and will be omitted here with the exception of the mixer properties analysis. The model assumes a variable geometry inlet such that the engine airflow matching can be achieved without having to constrain the operating point of the gas generator. It is also assumed that the inlet can turn and pass the desired mass flow without incurring any spillage across the lip. However, achieving these two criteria at all flight Mach numbers is never done in practice as it requires too complex a mechanism. What is often the case, rather, is the implementation of a variable geometry inlet scheme that maximizes inlet pressure recovery and minimizes nacelle drag at key operating conditions. In addition, the nozzle throat area is assumed to be fully variable so as to keep T_{t4}/T_{t2} a free parameter, and to achieve isentropic expansion of the exit flow at all flight conditions. It will be later revealed that by maximizing the exhaust streamtube area in this manner, we can also minimize the nacelle wave drag attributed to the inevitable expansion and contraction of the streamtubes as the flow passes through the engine. Although idealistic, the purpose of modeling the cycle as such is to estimate the minimum achievable nacelle drag for any particular cycle, regardless of the specifics of the geometry.
The polytropic efficiencies of the compressor and turbine and other mechanical and component efficiencies, with the exception of the inlet pressure recovery, are assumed to be constant and independent of the design and operating point. Specifically, the inlet pressure recovery is assumed to be a sole function of the flight Mach number, and is defined in accordance with MIL-E-5008B specifications as follows [16]:

$$\pi_i = 1 - 0.075(M_\infty - 1)^{1.35}. \tag{3.3}$$

3.1.2.1 Mixer Conditions

To find the conditions downstream of the mixer, the flow conditions downstream of the fan are first calculated via continuity

$$D(M_7) = \sqrt{\frac{T_{t7}}{T_{t2}}}\frac{P_{t2}}{P_{t7}} \cdot D(M_2), \tag{3.4}$$

where, the corrected mass flow is defined as follows:

$$D(M) = \frac{M}{\left[1+\left(\frac{\gamma-1}{2}\right)M^2\right]^{\gamma+1/2(\gamma-1)}}. \tag{3.5}$$

There exists no analytical solution for M_7, and it must be obtained iteratively. Now, based on the requirement that the static pressures of the two flows have to be equal at the mixing plane, the Mach number at the turbine exit, M_5 can be calculated via Kerrebrock's expression [27].

$$M_5 = \sqrt{\frac{2}{\gamma-1}\left[\left(1+\frac{\gamma-1}{2}M_7^2\right)\left(\frac{P_{t5}}{P_{t7}}\right)^{(\gamma-1)/\gamma} - 1\right]}. \tag{3.6}$$

The area ratio between the bypass and core flow can be expressed in terms of M_5.

$$\frac{A_7}{A_5} = \alpha\sqrt{\frac{T_{t7}}{T_{t5}}}\frac{M_5\left(\frac{P_{t7}}{P_{t5}}\right)^{-(\gamma-1)/2\gamma}}{\sqrt{\frac{2}{\gamma-1}\left[\left(1+\frac{\gamma-1}{2}M_5^2\right)\left(\frac{P_{t7}}{P_{t5}}\right)^{(\gamma-1)/\gamma} - 1\right]}}. \tag{3.7}$$

Momentum conservation yields an expression for stagnation pressure ratio between the mixed flow and the turbine exit, P_{t9}/P_{t5}, as a function of the above area ratio.

$$\frac{P_{t9}}{P_{t5}} = \frac{\left(1+\gamma M_5^2\right)+\left(1+\gamma M_7^2\right)\left(A_7/A_5\right)}{\left(1+\gamma M_9^2\right)\left(1+A_7/A_5\right)}\left(\frac{1+\frac{\gamma-1}{2}M_9^2}{1+\frac{\gamma-1}{2}M_5^2}\right)^{\gamma/(\gamma-1)}. \tag{3.8}$$

Similar to the steps carried out in equation 3.8 (above), mass continuity yields another expression for the pressure ratio.

$$\frac{P_{t9}}{P_{t5}} = \frac{\sqrt{(1+\alpha)\left(1+\alpha\frac{T_{t7}}{T_{t5}}\right)}}{1+A_7/A_5}\frac{M_5}{M_9}\left(\frac{1+\frac{\gamma-1}{2}M_9^{\,2}}{1+\frac{\gamma-1}{2}M_5^{\,2}}\right)^{\gamma/2(\gamma-1)} \quad . \tag{3.9}$$

Simply stated, equations 3.8 and 3.9 must be solved for the two unknowns – the pressure ratio term on the left side, and M_9, embedded into the unsolvable right side. A solution can be sought iteratively by 'guessing,' a value for three of the four M_9 terms in both equations and subsequently solving for the remaining term as follows:

$$M_9 = \frac{\left(1+\gamma\tilde{M}_9^{\,2}\right)\sqrt{(1+\alpha)\left(1+\alpha\frac{T_{t7}}{T_{t5}}\right)}}{\left(1+\gamma M_5^{\,2}\right)+\left(1+\gamma M_7^{\,2}\right)(A_7/A_5)}\left(\frac{1+\frac{\gamma-1}{2}\tilde{M}_9^{\,2}}{1+\frac{\gamma-1}{2}M_5^{\,2}}\right)^{-\gamma/2(\gamma-1)} \quad . \tag{3.10}$$

For the purposes of calculating the wave drag, the three streamtube areas of interest are of the freestream, compressor front face, and the fully expanded exhaust, and can be written in the following general form:

$$A_k = \frac{\dot{m}(1+\alpha)}{\frac{P_k}{RT_k}M_k\sqrt{\gamma RT_k}} . \tag{3.11}$$

where k denotes the respective station designations. For the fully expanded exhaust, we can write the exit Mach number as

$$M_{10} = \left[\left(\frac{P_{t9}}{P_0}\right)^{\gamma-1/\gamma} - 1\right]\frac{2}{\gamma-1} . \tag{3.12}$$

3.1.2.2 Fan pressure ratio selection

For trade studies involving cycles with different bypass ratios, GasTurb's "adaptive random search" algorithm was employed in an attempt to optimize the fan pressure ratio of each cycle. It was found that a considerable amount of 'hand holding' is required throughout the process for this type of optimization, as the natural tendency for the optimizer is to favor a higher fan pressure ratio (thereby increasing OPR if the compressor pressure ratio is to remain fixed). As a practical matter, given the high external compression for engines

operating at supersonic speeds, a high OPR is not an option if one considers the limits on T_3. In principal however, because there is no such thing as free OPR, it was deemed that a fair comparison could be made only by keeping OPR constant. The intent of the optimization was to find the optimal balance between π_f and π_c for any fixed OPR. For future fan pressure ratio optimization, the author suggests that the OPR be adjusted at each flight Mach number so as to keep T_3 constant.

In terms of TSFC, the optimal π_f was often found to be much higher than those typically seen on existing engines of the same bypass ratio. In practice, a lower-than-optimal π_f is favored as a means of minimizing the overall weight of the engine by limiting the number of weighty fan stages. That, combined with the fact that the optimal compression comes in discrete factors, may prove to be sufficient reason for designers to "round down" to a lower-than-optimal π_f.

3.1.3 Nacelle Drag Estimation

The wave drag on a nacelle can be estimated by representing it as an equivalent axisymmetric body with base area that correspond to the engine inlet and exit streamtube areas [10].

$$C_{Dnac} = K_0(A_0, A_d, A_{10})\frac{128}{S_{ref}\pi}\frac{V_{nac}^2}{l_{nac}^4}, \tag{3.13}$$

where the streamtube K_0 factor is a function of the maximum nacelle cross sectional area, and inlet and exit streamtube areas. For the purposes of estimating the minimal achievable wave drag, this maximum cross sectional area of the engine is assumed to be no larger than that of the compressor front face. In addition, the presence of the engine is modeled as an isolated drag source, with no adverse or favorable interference effects between the airframe and engine, as is not often the case for supersonic aircraft with submerged engines and high length-to-span ratio. The effective volume of this body is then taken as the integral of the

difference between the local cross sectional area and the smaller of the inlet or exit streamtube area.

$$V_{nac} = \int_{x=0}^{x=l\,nac} A_x - \min(A_0, A_{10})dx. \tag{3.14}$$

Although an analytical evaluation of the above integral requires the exact geometry of the nacelle to be known, it can be evaluated parametrically via Eminton's [28] wave drag minimization method. Much like how the length and caliber of an axisymmetric body defines a unique Sears-Haack geometry, there exists an ideal distribution that minimizes the wave drag on a blunt-based axisymmetric body.

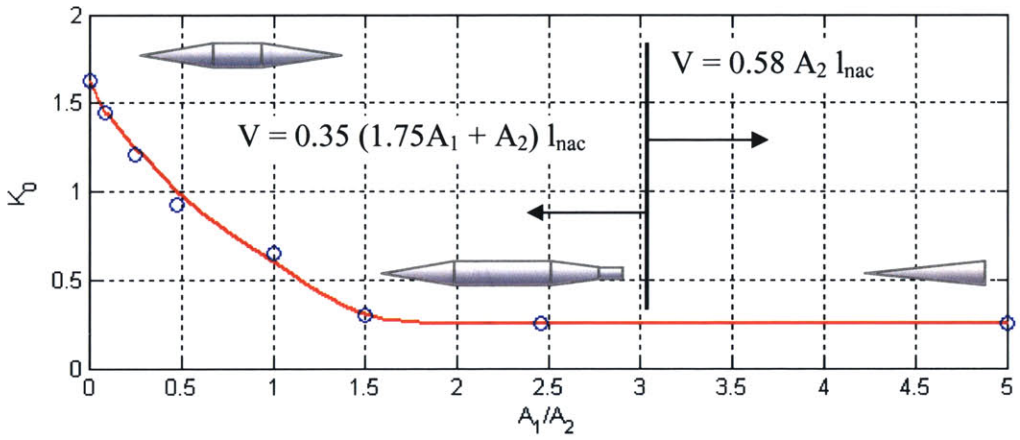

Figure 3.2: K_0 parametric for streamtubes with various area ratios (Adapted from [10])

3.1.3.1 Nacelle Drag Scaling

Engine configuration and integration has the potential to affect the overall propulsion system performance just as much as the cycle selection. Fuselage boundary layer ingestion and its contribution to distortion, exhaust flow scrubbing losses, and nacelle wave drag interference are examples of factors that one needs to consider when evaluating

configurations. For the case of isolated pod-mounted engines, such as in this case, it is possible to evaluate whether the overall reduced TSFC of the propulsion system is affected by the number of engines into which the total thrust is divided (many small engines vs. fewer larger engines). Under the quasi-1D thermodynamic cycle and rubber-engine assumptions, the cycle analysis is independent of this discretization, but such may or may not be the case for the nacelle wave drag. Simple dimensional analysis follows:

$$\begin{aligned} C_{Dnac} &= K_0\left(A_0, A_d, A_{10}\right)\frac{128}{S_{ref}\pi}\frac{V_{nac}^2}{l_{nac}^4} \\ &\sim K_0\left(A_d/A_0, A_d/A_{10}\right)\frac{\left(l_{nac}d_{nac}^2\right)^2}{S_{ref}l_{nac}^4} \\ &\sim K_0\left(A_d/A_0, A_d/A_{10}\right)\frac{l_{nac}^2}{S_{ref}l_{nac}^4}\left(\frac{l}{\left(l/d\right)_{nac}}\right)^4 \end{aligned} \tag{3.15}$$

If the streamtube area ratios and the engine length-to-diameter ratios are assumed to be only a function of cycle, then the relationship further simplifies to

$$\begin{aligned} C_{Dnac} &\sim \frac{l_{nac}^2}{S_{ref}}, \text{ or} \\ D_{nac} &\sim C_D\, qS_{ref} \sim q\, l_{nac}^2 \end{aligned} \tag{3.16}$$

where, the dynamic pressure, q is a function only of the flight condition and can be held constant for this analysis. With the assumption that the exhaust flow is fully expanded, we can write the net thrust as follows:

$$T = \alpha\dot{m}\left[(1+f)u_{10} - u_0\right], \tag{3.17}$$

which, for fixed cycle, becomes

$$\begin{aligned} T \sim \dot{m} \sim \rho_0 A u_0 &\sim \frac{Aq_0}{u_0} \sim \frac{d_{nac}^2 q_0}{u_0} \sim \frac{q_0}{u_0}\frac{l_{nac}^2}{\left(l/d\right)_{nac}^2} \\ T &\sim l_{nac}^2 \times g(cycle) \times h(\textit{flight condition}). \end{aligned} \tag{3.18}$$

Taking the ratio between net thrust (equation 3.18) and nacelle drag (equation 3.16), we obtain

$$\frac{T}{D} \neq f(scale), \tag{3.19}$$

What this scaling analysis demonstrates is that the total nacelle drag of a propulsion system is—to the first order—independent of how the thrust is broken up. Furthermore, by rewriting the *reduced TSFC* in terms of this fixed ratio, we can also see that this metric is independent of scale as well.

$$TSFC_{red} = \frac{T-D}{\dot{m}f} \sim \frac{T - \frac{T}{(T/D)_{const}}}{\dot{m}f} \sim \frac{T}{\dot{m}f} \sim \frac{\dot{m} \times g(cycle)}{\dot{m}f} \neq f(scale). \tag{3.20}$$

Despite this first-order invariance to scale, the inclusion of friction drag into our consideration will tend to bias the results in favor of larger scale propulsion systems, as the Reynolds number and the wetted area terms in the expression for friction drag leave a length-scale dependence in equations 3.19 and 3.20. This, combined with the trend for lower component efficiencies associated with larger component tolerances and blade tip clearances at small scales will again favor a single large engine over an array of smaller engines. There are, however, competing factors that favor the opposite, as will be pointed out later in the discussion of wake recovery and its benefit on propulsion system efficiency (Section 5.3.1.3).

3.2 Results and Model Verification

This section will evaluate the TSFC and nacelle drag of the baseline and modified engine cycles using the preceding synthesis model (Table 3.1). All comparisons will be made at Mach numbers and altitudes that correspond to the trajectory that was found to be 'aerodynamically optimal' in Section 2.3.1 (constant C_L up until cruise altitude, and C_l thereafter).

Table 3.1: Cycle parameters for TF30 engine

Baseline Cycle (TF30-P-111)		
Overall pressure ratio	21.8	
Bypass ratio	0.73	
Fan pressure ratio	2.43	
Turbine inlet temp ratio, TT4/TT2	5	
Length to diameter ratio	4.93	
Compressor polytropic efficiency	0.85	
Turbine polytropic efficiency	0.85	

Design Operating Point		
Cruise altitude	56000	ft
Cruise Mach	1.6	
TT4/TT2	5	

The fan pressure ratio for each of the modified cycles was optimized via the method described in Section 3.1.2.2. Figure 3.3 below plots TSFC as a function of FPR and reveals that for each bypass ratio, there exists a TSFC 'bucket' whose minima decreases with increasing bypass ratio. It is also apparent that fan pressure ratio selection is much more critical for higher bypass ratio engines, which tend to have narrow FPR ranges for optimum TSFC.

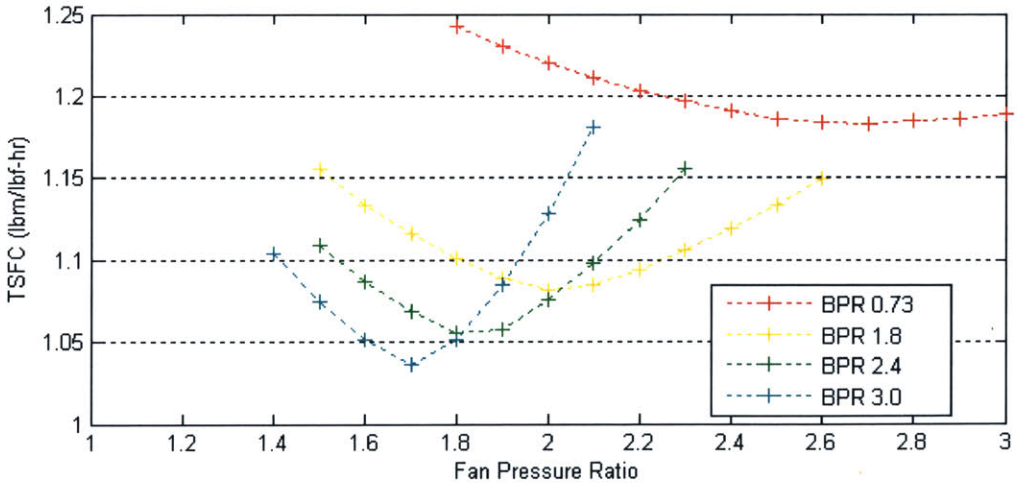

Figure 3.3: Fan pressure ratio optimization

As a means of quantifying nacelle drag, we define a nondimensional parameter, the engine efficiency factor (eef) to be the percent loss in uninstalled thrust.

$$eef = \frac{T_{uninst} - D_{nac}}{T_{uninst}}. \tag{3.21}$$

Although the *eef* provides useful insight into the behavior of the nacelle drag itself, the reduced TSFC remains to be the final metric in evaluating the attractiveness of each cycle from an integrated aerodynamic and propulsive standpoint.

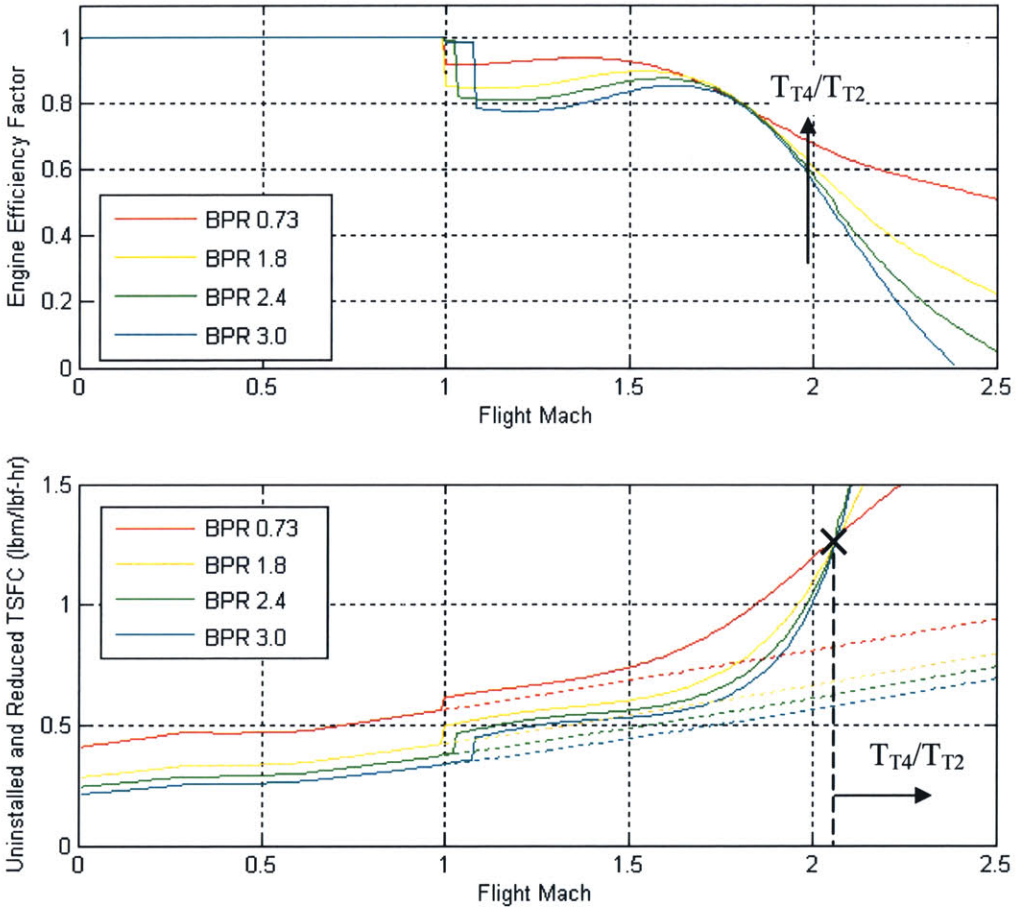

Figure 3.4: Effect of nacelle wave drag on integrated engine performance (solid: reduced TSFC; dashed: uninstalled TSFC)

Note that the TSFC values obtained from the synthesis model are considerably lower than those obtained from GasTurb for the purposes of optimizing fan pressure ratio. This discrepancy can be attributed to the several simplifying assumptions that the synthesis model makes, the most important of which is the assumption that the exhaust flow

undergoes a fully isentropic expansion via a variable geometry converging-diverging duct. Losses other than those incurred from compression and expansion (such as duct losses and mechanical efficiency) have also been neglected. In addition, the TSFC bucket that one typically sees across the subsonic Mach number regime is absent in this synthesis since the pressure recovery is assumed to be unity at subsonic regimes and not the familiar 'inverse bucket' curve, typically responsible for the TSFC bucket. Despite these limitations, the effect of cycle on its corresponding nacelle drag is still expected to be captured successfully by the variations in the relative magnitudes of TSFC. According to the plot of *eef*, it is interesting to note that for these particular cycle parameters (Table 3.1), there exists an operating Mach number (~1.8) at which all engines, irrespective of bypass ratio, have the same thrust to nacelle drag ratio. Below and above this singularity, lower specific thrust cycles suffer a larger nacelle drag penalty. The fact that the four curves converge to a single point is simply a coincidence, but the general trend towards the narrowing of the curves can be explained as the combination between two competing factors: external compression and nacelle drag. For increasing Mach numbers below 1.8, the increase in thrust as a result of the higher external compression dominates the nacelle drag rise to yield a net increase in the *eec* parameter—an effect which is more pronounced for higher bypass ratio cycles. Above a critical Mach number, however, the opposite is true, and the mounting nacelle wave drag results in an overall decrease in the *eec*. Higher specific thrust cycles are less sensitive to these Mach variations, which explains the narrowing of the curves evident in Figure 3.4 and 3.5.

3.2.1 Effect of Other Cycle Parameters

In general, it was found that the nacelle drag of higher bypass ratio cycles are much more sensitive to cycle parameters such as T_{t4}/T_{t2} and OPR than are lower bypass ratio cycles. Hence, although increasing T_{t4}/T_{t2} tends to mitigate the nacelle drag (increase *eec*) for all cycles, its particularly strong impact on higher bypass ratio cycles means that the gap between the two extreme cases is narrowed (Figure 3.5, top). The same benefits can be seen for increases in OPR, though not to the extent of T_{t4}/T_{t2}. Unfortunately, the

aerodynamic benefit of increasing T_{t4}/T_{t2} is not enough to offset the thermodynamic cycle penalties. As evident from the bottom plot in Figure 3.5, the TSFCs corresponding to the elevated T_{t4}/T_{t2}s are noticeably higher than that of the nominal T_{t4}/T_{t2}s for most of the Mach range. Here, the culprit is the lower propulsive efficiency resulting from the higher exhaust velocity, which outweighs the improvements in thermodynamic efficiency to yield a net degradation in overall efficiency (TSFC). However, the opposite is true for flight Mach numbers past some critical Mach number, the exact value of which is relatively independent of bypass ratio—that is, all four cycles experience a gradually increasing improvement in reduced TSFC at speeds above Mach 2. In these regions, the increase in T_{t4}/T_{t2} yields a nacelle drag reduction large enough to outweigh the thermodynamic cycle penalty. Although this section deals with independent increases in the combustion temperature, which by itself, results in a TSFC increase, it is usually accompanied by higher OPR to result in a net cycle benefit. For those reasons, had the T_{t4}/T_{t2} sensitivity study been carried out with commensurate adjustments in OPR, the engine efficiency factor would have been higher than that dictated by Figure 3.5 below, which assumes a fixed OPR. Incidentally, because the ideal OPR is often limited by the achievable polytropic efficiencies, its variation in this analysis would absorb higher polytropic efficiency-dependent effects that would not be as easily discerned in the final results. The OPR was kept fixed for all analyses for this reason. In general, however, this case study supports our presumption that if higher combustion temperatures and compression ratios do not necessarily yield a thermodynamic cycle benefit, then it will at least help the integrated performance of the propulsion system by driving engine geometries to those that are favorable from the perspective of nacelle wave drag (more compact engine).

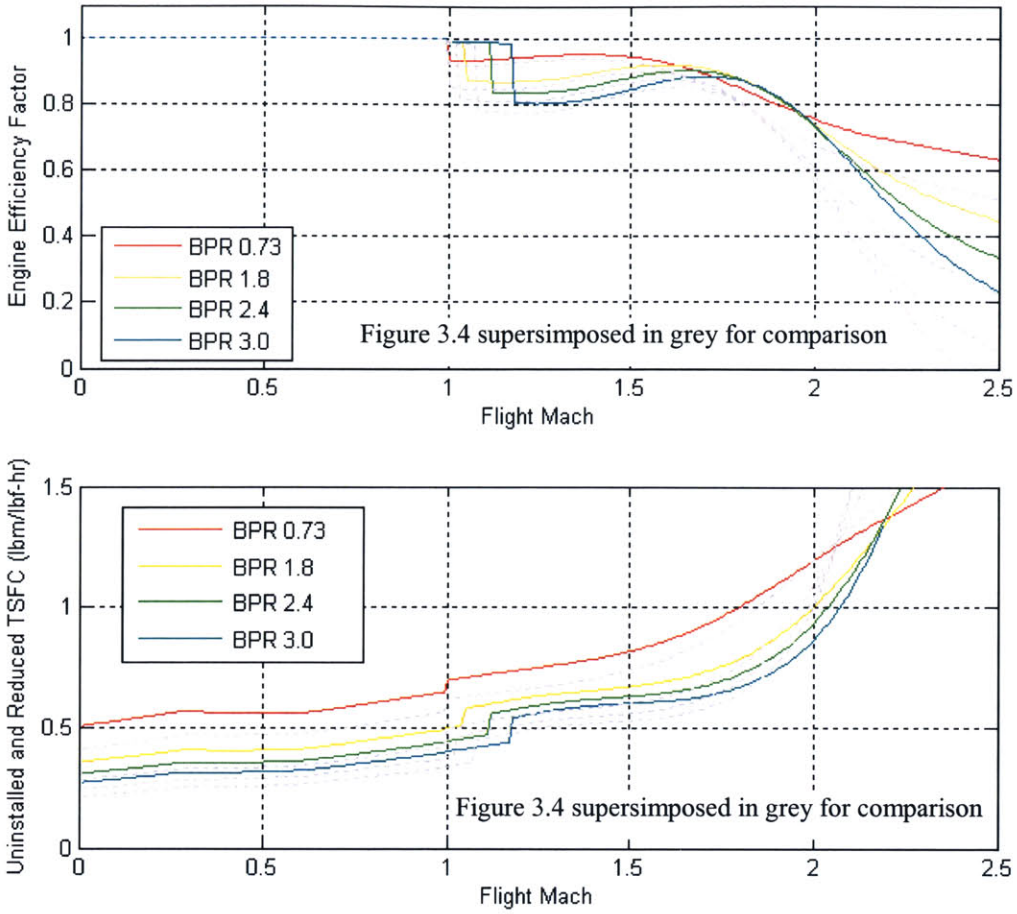

Figure 3.5: Effect of raising T_{t4}/T_{t2} on nacelle drag (colored: T_{t4}/T_{t2}=6; grey: T_{t4}/T_{t2}=5)

Chapter 4

Mission Synthesis

This section discusses the methodology for correlating the results of the aerodynamic, propulsive, and structural synthesis models to relevant mission performance metrics – namely, loiter time, endurance, and combat radius. The types of mission considered include long range strike with various combinations of loiter and dash and are derived from the requirements proposed for the recent DARPA Switchblade program.

The distance that an aircraft and steady level flight covers over a period of time it takes to burn an incremental amount of fuel can be written as a differential expression as follows:

$$\frac{dR}{dW} = \frac{M\,a(L/D)}{TSFC\,W}. \tag{4.1}$$

Integrating this expression for constant aerodynamic and propulsive efficiency yields the familiar Breguet Range equation. Because we are afforded the luxury of evaluating the non-constant terms as a function of instantaneous weight, however, we can calculate the *exact* integral so as to take into account the probable degradation in L/D and TSFC as the aircraft becomes lighter and as the engine is throttle down, respectively.

$$R_{i,i+1} = \int_{W_i}^{W_{i+1}} \frac{M\,a \times \frac{L}{D}(W)}{TSFC(W) \times W}\,dW \le \frac{M\,a}{TSFC}\frac{L}{D}\ln\left(\frac{W_i}{W_{i+1}}\right), \tag{4.2}$$

where i denotes the designation at each phase of the mission. With these off-design considerations, the actual range of integrated mission segment is expected to be less than that predicted by the Breguet Range equation.

4.1 Weight Fraction Parametrics

Perhaps the area with the greatest amount of work that needs to be done to ensure the completeness of this thesis is the field of weight estimation. In this thesis, weight estimation, as a part of the mission syntheses of the following sections, has been boiled down to a simple parametric estimation of a single parameter—the empty weight fraction. In an actual design process, this is estimated and minimized through careful bookkeeping of the weight of all the subsystems, and a thorough stress analysis of all the structural components. Although several factors—the most important of which are listed below—will affect the empty weight fraction, a detailed analysis was beyond the scope of this effort, as the calculated uncertainty in the final metric is expected to be just as large as the common range of weight fractions for a full spectrum of aircraft (as high as 0.6 for a jet fighter and as low as 0.25 for a large composite span-loaded aircraft).

- The engine integration scheme will establish the distribution of engine weight across the span of the OFW and will therefore prescribe the stiffness and the commensurate weight of the wing spars (i.e an array of small engines distributed along the span will help achieve true span-loading and a low empty weight fraction)
- Aeroelasticity and aeroservoelasticity considerations will compel the structural weight to be higher than what can be achieved for a comparable non-oblique flying wing. Such considerations were ignored for the purposes of weight estimation.
- The question of survivability for military purposes aside, the use of low-density composite materials for achieving the lower-limit to the empty weight fraction is limited by the design operating speed and the amount of aerodynamic heating that is incurred at that speed. Although Brear [29] suggests M 2.4 as a point of reference for such considerations, the exact Mach limit is highly dependent on the type of composite and its density.

By superimposing the structural weight expectations of the OFW onto the trends provided by Raymer for conventional aircraft, an empty weight fraction (ef) of 0.3 was selected to be reasonable for a 100,000 lb class OFW. Since the projected *ef* tends to decrease linearly

with the log of the gross weight, this value is only suitable for OFWs in this weight range, with 10,000 lb-class OFWs expected to have values closer to 0.4. It is important to remember that uncertainties in the *ef* tends to have a magnifying effect on the uncertainties in the gross weight of the aircraft, since a heavier aircraft has to pay the penalties with respect to fuel weight as well.

With an empty weight fraction specified, the remaining weight fractions, the fuel fraction (ff) and payload fraction (pf) must be traded off for optimal mission performance. For any given payload and combat radius, the total fuel consumption can be minimized by scaling down the aircraft such that the *pf* is large and the *ff* small. In general, however, the internal volume available for the payload constraints the maximum achievable *pf*, and such is expected to be especially the case for the OFW, which suffers from an inherently low volume-to wetted area ratio.

4.2 Results and Verification

A lo-lo-hi strike mission, originally intended for the F-111, was synthesized for the baseline OFW and a comparable supersonic symmetric wing aircraft. The results were then compared against values published for the F-111 proposal [3].

Table 4.1: Mission segment designations for lo-lo-hi strike mission

Mission Breakdown	
1	Takeoff
1-2	Mach 0.6 cruise at SL
2	Accelerate to dash speed
2-3	Supersonic dash to target at SL
3	Payload release, military power zoom climb
3-4	Mach 0.8 cruise at 40,000 ft

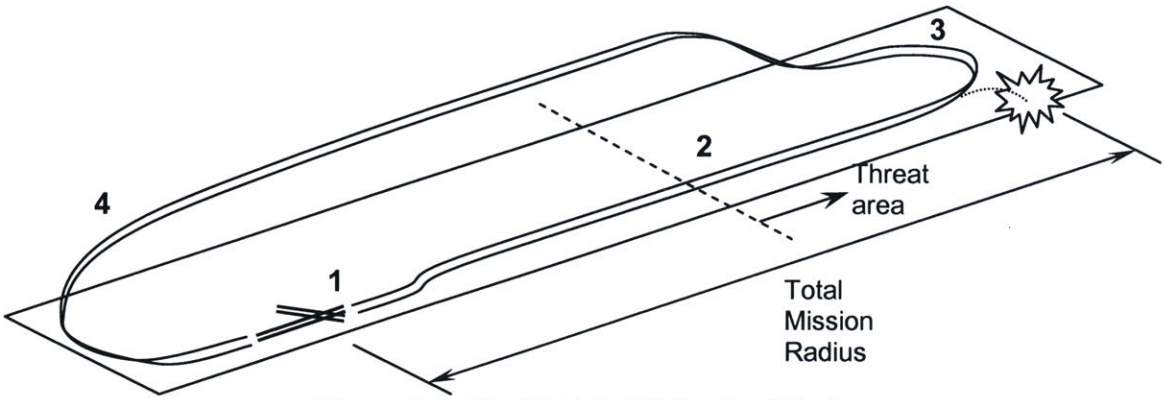

Figure 4.1: The F-111's Hi-Lo-Lo Mission

With the gross takeoff weight fixed, the variables which are to be traded off for this mission include total mission radius, dash distance, and dash speed, all of which, whose maximization benefits survivability and utility.

4.2.1 Mission Tradeoff for OFW

Figure 4.2 below plots lines of constant dash speed as total mission radius (1-3) is traded off for sea level dash distance (2-3)

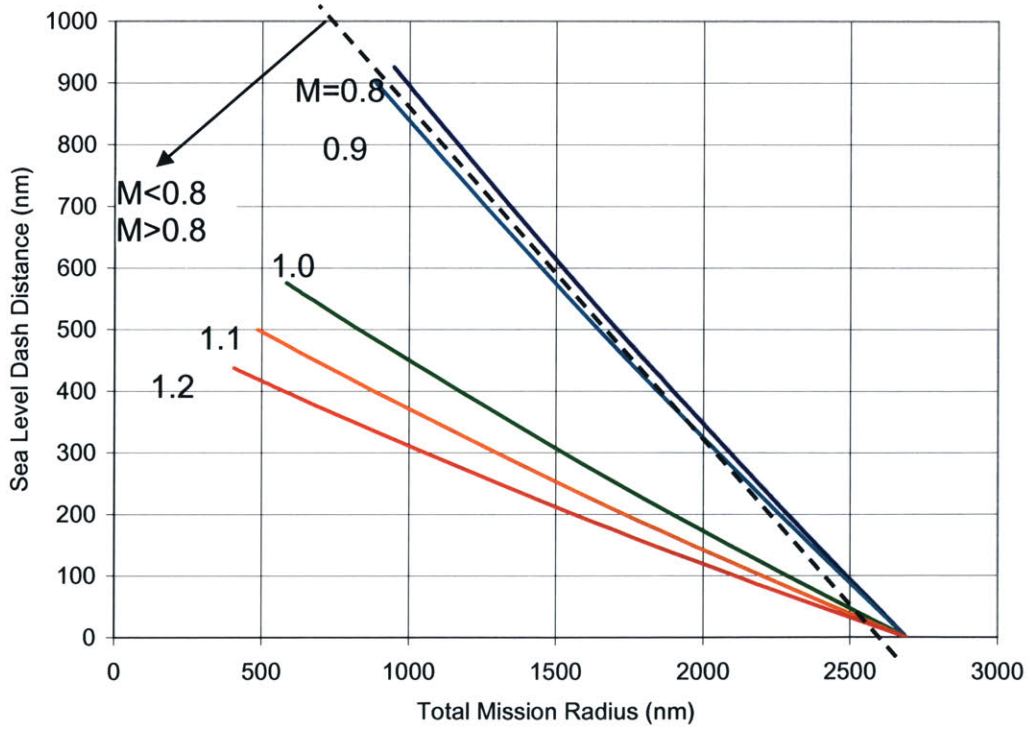

Figure 4.2: Mission performance tradeoff for the baseline OFW

The substantial aerodynamic penalty due to wave drag is immediately evidenced by the large variation in slope between the M=0.9 and M=1.0 lines. Note that the location where the lines terminate on the left marks the case where the ingress to target consists solely of the supersonic dash segment (dash distance equals the combat radius). Although not plotted on the figure, dash speeds lower than M0.8 were found to reverse the trend, with the total mission radius becoming progressively smaller with decreasing Mach. This indicates that the range parameter, M(L/D)/TSFC is maximized in the vicinity of this dash speed.

The weak nonlinearity in the lines of constant Mach is an artifact of the L/D and TSFC variations as the aircraft becomes lighter throughout the mission, and will be referred hereafter as "off design penalties." In this case, the slight upslope indicates that these off design penalties tend to be mitigated for missions that have comparatively longer dash segments, implying that *off-design* is more influential a factor at low speeds than high speeds. A reasonable explanation is that since the induced drag accounts for a greater percentage of the total drag at lower speeds, the off design penalties—which arise from the changes in the lift-dependent drag terms—will be greater at these speeds as well. Whatever the causes of these perturbations may be, the fact that their effects are insignificant implies that the constant range parameter integral—the Breguet range equation—is a sufficiently accurate approximation for our purposes.

4.2.2 Mission Tradeoff for Conventional Symmetric Wing Supersonic Aircraft

Figure 4.3 below is a similar representation for a comparable supersonic symmetric wing aircraft whose drag polars were extrapolated from that of the Concorde [25].

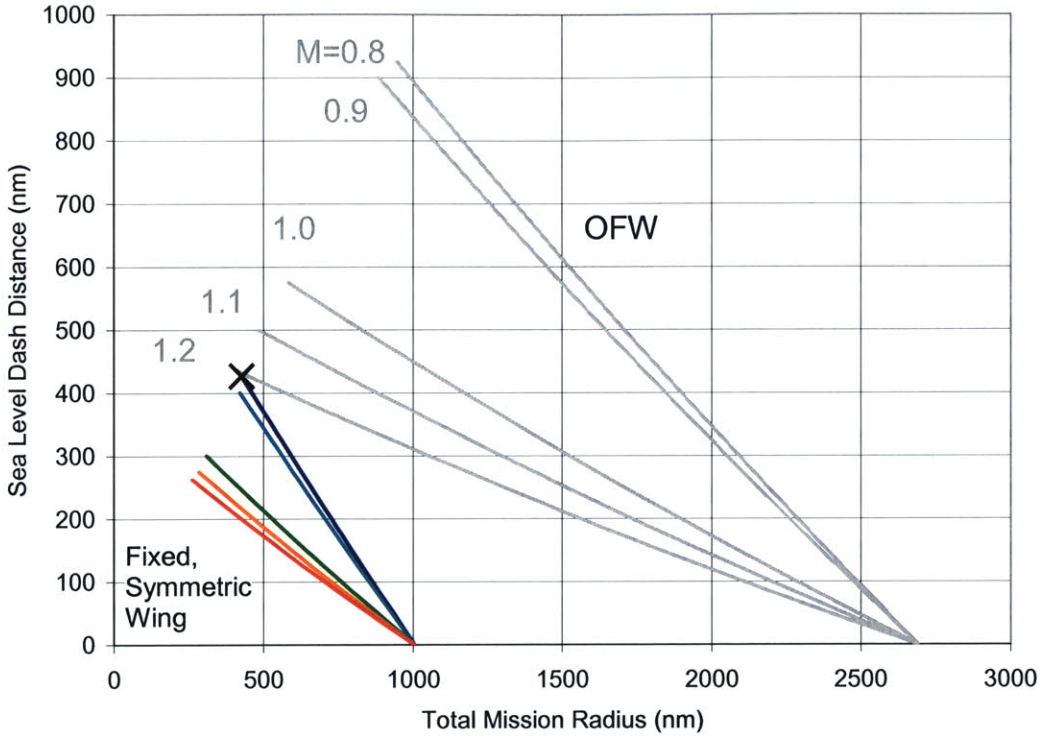

Figure 4.3: Mission performance tradeoff for a comparable fixed-symmetric wing aircraft (OFW in grey)

The attainable total mission radius for this symmetric wing aircraft is approximately 40% of that of the baseline OFW, mostly due to the high induced drag penalty it suffers during the high altitude subsonic flight during the return phase. The location where the M=1.2 line of the OFW abuts the M=0.8 line of the conventional aircraft marks the case where both aircraft fly identical missions. However, whereas the OFW can dash to the target at supersonic speeds, the conventional aircraft must do so subsonically to cover the same distance. In fact, the conventional aircraft is far from optimal for such a mission, and the resulting comparison between it and the OFW is hardly objective. A much fairer comparison can be made with a subsonic-optimized symmetric wing aircraft with supersonic capabilities—the F-111 discussed in the next section being such an example.

4.2.3 Mission Tradeoff for F-111

The F-111, which employs symmetric variable-sweep, is such an aircraft. Figure 4.4 superimposes, on top of the two synthesized plots, the projected F-111 mission performance obtained from the manufacturer's proposal document [3].

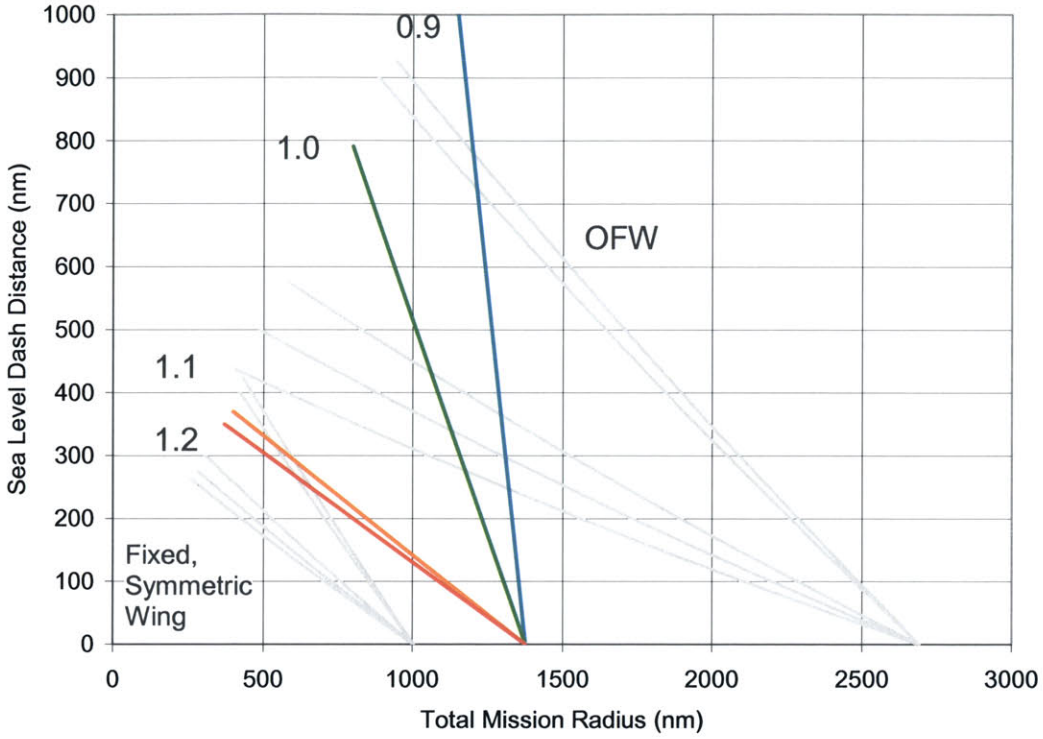

Figure 4.4: Published mission performance tradeoff for F-111 with full internal fuel and external stores, (1) MK-43 plus (2) AIM-9/B's
(OFW and fixed-symmetric wing aircraft in grey)

The F-111 has appreciably higher mission radius across all dash speeds compared to the fixed symmetric sweep case. In fact, for long dash distances at high subsonic speeds (M0.9), the F-111 can achieve a mission radius larger than an OFW with the same dash speed. The author would like to point out that these F-111 mission performance figures are not demonstrated by the manufacturer. That, combined with the uncertainty in the theoretical wave drag estimation via linearized theory, should be enough reason to hold suspect any comparisons made between the two types of aircraft. Once again, the comparison is biased in favor of the OFW, which assumes internal stores for observability

reasons. The published performance estimates for the F-111, on the other hand, do not make that assumption.

Chapter 5

Integrated Design Considerations

In the previous sections, we addressed such questions as "what flight trajectory, sweep schedule, and large-scale geometric parameters are optimal for the purposes of maximizing the OFW's aerodynamic efficiency?" and "how sensitive is the final metric to deviations from those optimal design and operating spaces?" We subsequently addressed propulsion considerations from the isolated perspective of cycle selection for any supersonic aircraft which has range as one of its primary metrics – namely, "what types of cycles maximize effective TSFC?" This section investigates the next two steps in the propulsion selection process (engine sizing and integration schemes) by taking into consideration the aerodynamic and geometric characteristics unique to the OFW. The former is the dominant consideration for engine sizing, while the latter is the primary driver of integration concepts.

5.1 Engine Sizing

Historically, transonic acceleration performance has sized the engine for most supersonic fighters, with most requiring thrust augmentation to penetrate the transonic drag rise and to sustain supersonic flight (the exception being aircraft with supercruise capabilities, such as the F-22). With this being the case, many supersonic fighters whose engines are sized for this restrictive regime automatically and involuntarily exceed the dash speed requirements. For example, the F-14, originally intended as a Mach 2.2 interceptor, has an unofficial nominal top speed of Mach 2.5. In another example, the Olympus turbojet engines on the Concorde, requires reheat to accelerate the aircraft from Mach 1 to Mach 1.7, but not for cruise at higher Mach. The purpose of this subsection is to investigate the criticality of the transonic regime for the OFW and to see which sizing criteria apply.

5.1.1 Specific Excess Power, P_s

Although P_s is often the preferred metric for evaluating the maneuverability potential of a fighter, it is chosen here as a means of sizing the engine at key operating points (takeoff, transonic acceleration, and supersonic cruise) and for quantifying the climb and acceleration performance throughout the entire envelope. Thrust to weight ratio is also considered, as it influences the takeoff distance. In comparing the aircraft performance between the two types of aircraft, it was considered whether the comparison be made at matching wing loadings, or wing loadings optimized for cruise for each respective aircraft (see altitude trajectory section). To first order, the scale at which the excess power, P_s, is evaluated is irrelevant since the weight dependence in the expression can be dropped; once again, a rubber aircraft and engine model can be conveniently adopted for this analysis. The excess power can be re-written in terms of the nondimensional metrics established in the earlier sections as follows:

$$\begin{aligned} P_s &= \frac{v}{W}(T - D) \\ &= \frac{v}{W}\left[W \cdot \left(T/W\right) - \frac{W}{L/D} \right] \\ &= v\left(T/W - \frac{1}{L/D} \right) \neq f(W) \end{aligned} \tag{5.1}$$

where the lift to drag ratio, L/D is still highly dependent on wing loading, W/S for any particular altitude as shown in Section 2.3.1. Although a simplified nacelle drag model was developed earlier, it is not incorporated into the engine sizing scenarios of this section, and the engine is sized only big enough to offset the airframe drag (nacelle drag is assumed negligible compared to airframe drag and therefore doesn't affect engine sizing).

At a design flight condition of M 1.6 at 56,000 ft, it was found that a wing loading of 45 psf achieves a lift coefficient similar to a half-loaded Concorde at its design point of M 2.0. Similarly, 45 psf corresponds to a normal Mach and lift coefficient that is near-optimal for

maximizing the OFW's L/D at this regime. Hence, it was deemed that matching the wing loading at 45 psf was reasonable for the purposes of this comparison. Figures 5.1 and 5.2 plot P_s contours for the OFW and the Concorde, both with the nominal TF30 cycle (Table 3.1) sized to yield a T/W of 0.75 at takeoff. Superimposed on top of the P_s contours are lines of constant energy heights, defined as

$$h_e = h + \frac{1}{2g} v^2 . \tag{5.2}$$

5.1.2 Best Climb Trajectory

By marking the locus of points where the lines of constant P_s lie tangent to the lines of constant h_e, best time to climb trajectories were obtained and traced onto their respective figures. Note that the trajectory for best climb does not necessarily coincide with the loci of maximum P_s. The resulting trajectories for both aircraft are similar in that initially, both accelerate at low altitude until reaching the speed for best P_s before commencing the climb. However, whereas the optimal climb trajectory for the Concorde (and presumably for most conventional supersonic aircraft) remains in the subsonic regime for the initial portion of the climb, the optimal OFW trajectory continues to accelerate into and within the supersonic regime for most of the climb. For this reason, the OFW trajectory is characteristic of that of a high-thrust fighter, in which a transonic dive at constant energy height is not necessary to minimize the time to climb. This can be verified via comparison with two published P_s plots provided in [16]—one for the F-104 "low-thrust" fighter, resembling Figure 5.2 and another for an unnamed high-thrust fighter resembling Figure 5.1

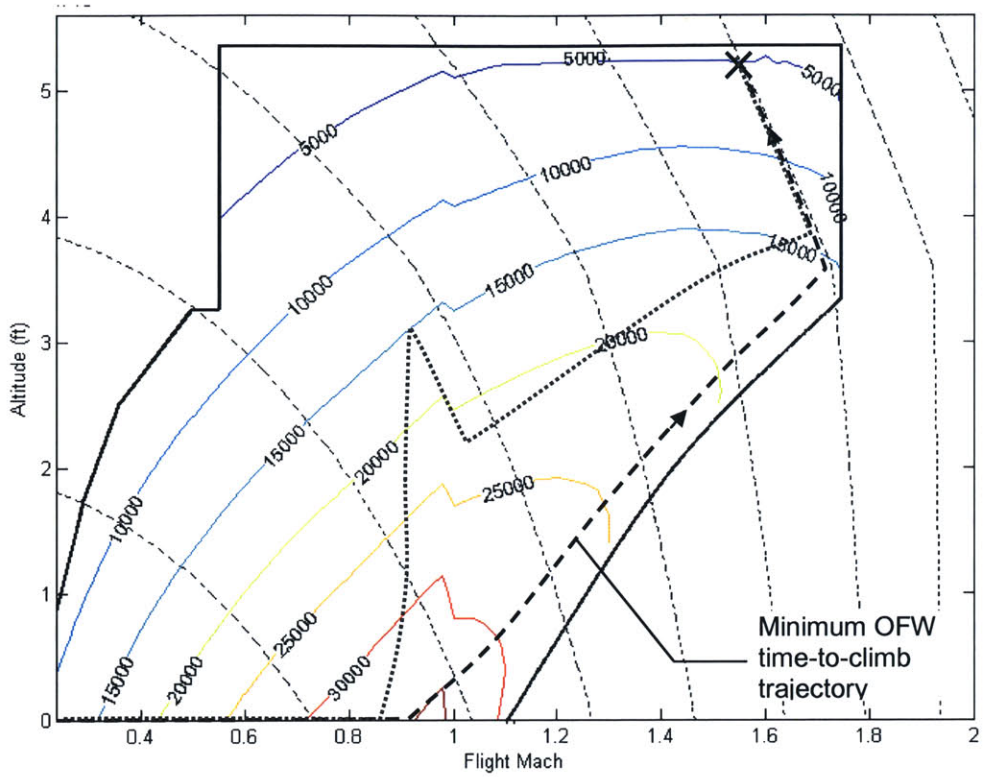

Figure 5.1: Ps contours for an OFW with a TF30 cycle engine (T/W = 0.75)

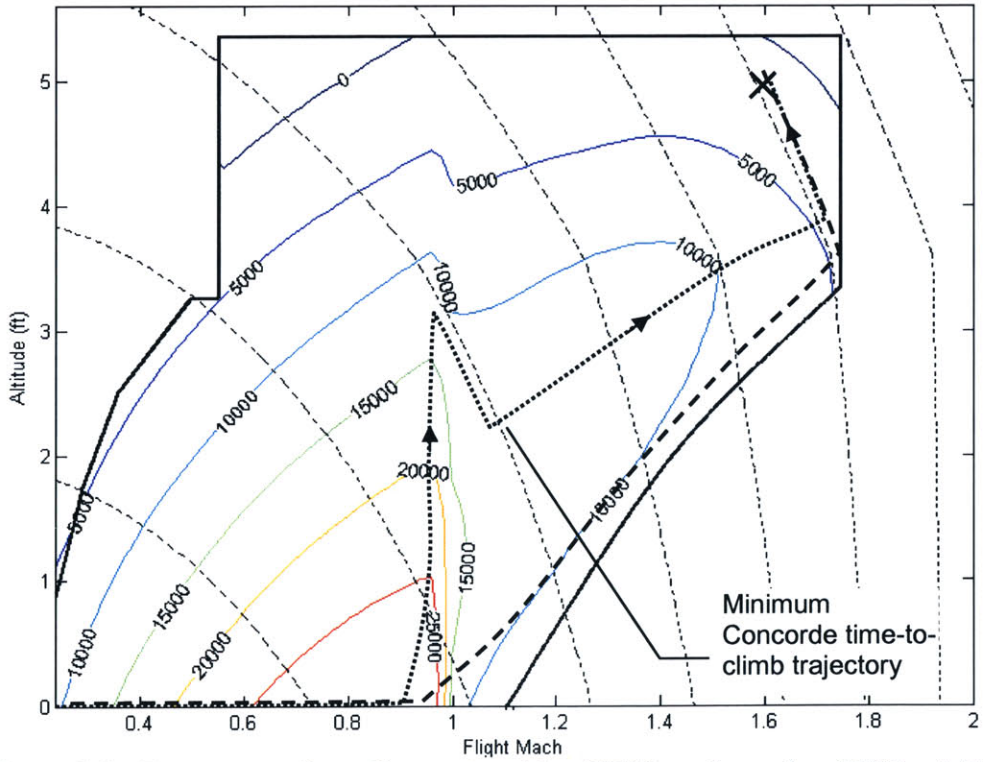

Figure 5.2: Ps contours for a Concorde with a TF30 cycle engine (T/W = 0.75)

The minimum time-to-climb trajectories can be obtained easily graphically (via the methodology explained at the beginning of this section), but not so computationally since it involves finding and integrating the tangent points of two discrete contour variables. Instead, it was assumed that the climb and acceleration performance along a common predetermined trajectory would be sufficiently indicative of the optimal capabilities of both aircraft. Moreover, it is unlikely that an aircraft in operation would be inclined to fly the best climb trajectory for the types of missions being proposed for the OFW. Most likely, the trajectory flown during some phases of the operation may be governed by survivability over all other metrics, as was the case for the military power zoom climb in the lo-lo-hi mission discussed earlier. For these reasons, there is little practical value in integrating the best climb trajectory for the purposes of sizing the engine.

5.1.3 Engine Sizing and its Effect on Climbing Flight

For the purposes of assessing climb performance, a common constant-C_L trajectory was selected for both aircraft. Here, the concern was that without a common altitude trajectory, the performance expectations for both aircraft would be considerably different simply because of the disparity in thrust between aircraft flying at different altitudes. The left side of Figure 5.3 below plots the common trajectory and the TSFC that corresponds to each altitude and Mach. The aerodynamic characteristics (total drag and L/D) unique to each aircraft are plotted on the right. From the large drop in the L/D for the OFW, it is evident that this constant C_L trajectory is far from what is optimal in the supersonic regime. Recall from Figure 2.4 that the maximum achievable L/D in the low supersonic range is near 20, as opposed to the current value of 10 that results from flying this aerodynamically suboptimal trajectory. Since the climb phase is assumed to be much shorter than the rest of the mission, however, this poor range performance during climb is not expected to hurt the overall mission performance significantly. The total thrust available along the altitude trajectory is omitted here as it varies from case to case depending on the engine sizing criteria.

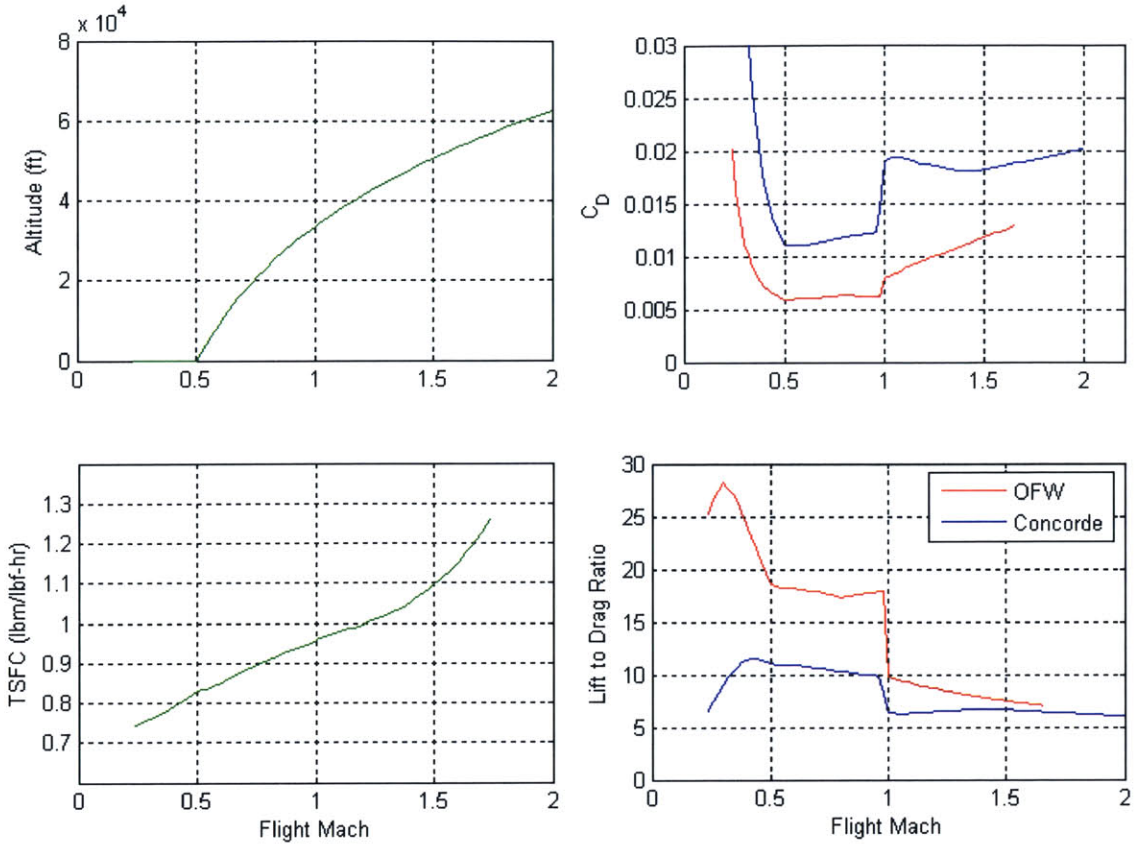

Figure 5.3: Altitude, TSFC, and drag characteristics along the common altitude trajectory for the OFW and Concorde (applicable for cases A, B, and C)

The following engine-sizing scenarios were investigated with the aircraft flying the trajectory specified above:

- Case A – Takeoff
- Case B – Transonic acceleration
- Case C – Supersonic cruise

For all three cases, the subsonic climb rate for both aircraft is disproportionately high for a long range strike aircraft. This is in part, due to the selection of a turbofan engine, which tends to oversize the engine for low speeds much more than would be the case for a turbojet. In fact, the selection of an afterburning turbojet, much like that of the Concorde, would tend

to minimize the disparity in the climb performance between the extents of the flight envelope.

5.1.3.1 Case A: Takeoff

It may be the case that OFWs designed for subsonic and low-supersonic cruise may require engines to be sized for takeoff because of sufficiently low thrust requirements at cruise. To verify this assumption, the takeoff ground roll distance was estimated and plotted as a function of OFW and Concorde T/W ratio.[4] Here, the following simplifying assumptions are made:

- Coefficient of rolling friction for both aircraft are the same ($C_{f,to}$=0.015) and constant throughout the ground roll
- Rotation speed of Concorde based on C_{Lmax}=0.8 (215 knots for W/S=100psf [30]; 144 knots for W/S=45psf); OFW value calculated based on maximum section lift coefficient, C_{lmax} of 1.0 (Appendix B)
- Thrust throughout takeoff roll constant and equal to thrust at rotation speed
- Wing loading of 45 psf for both aircraft

Based on these assumptions, the ground roll distance can be integrated to yield the following expression, modified from [27]:

$$x_T = \frac{-a_0^2 m}{\gamma p_0 S_{ref} C_{Do}} \ln\left(1 - \frac{mgC_{Do}/C_{L\max}}{T_{TO} - mgC_{f,to}}\right). \tag{5.3}$$

[4] This is not the balanced field length, as no accounting has been made for obstacles and engine-out conditions

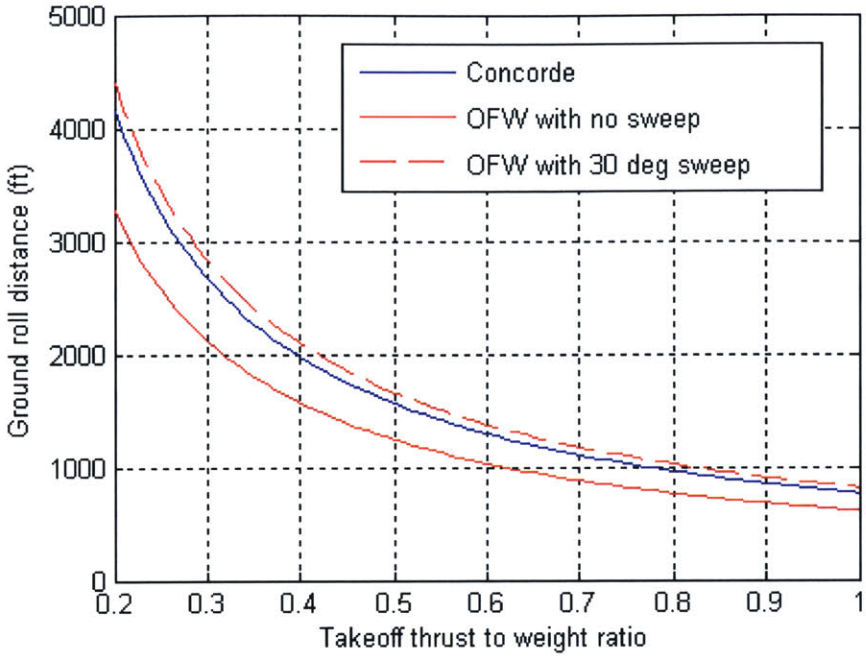

Figure 5.4: Effect of thrust to weight ratio on takeoff ground roll distance

As evident in Figure 5.4, the ground roll distance for both aircraft with thrust to weight ratios common for a jet transport (0.3-0.6) are considerably less than the length of standard runways (8000 ft). A wing loading of approximately half of what a loaded commercial transport—including the Concorde— achieves at takeoff explains why this is the case. Furthermore, sweeping the OFW to 30 degrees for takeoff reduces the maximum overall lift coefficient to 0.75, thereby increasing the ground roll distance beyond that of the Concorde's, but within the margin of uncertainty of the calculations. Figure 5.4 shows that to the first order, an OFW and a Concorde of the same wing loading can expect to have the same thrust to weight ratio requirements in order to achieve similar takeoff ground roll distances, and that those thrust to weight ratios are too low for supersonic cruise at M1.6. Figure 5.5 below plots the P_s of both aircrafts with a T/W of 0.75 as they fly along the common constant-C_L trajectory. A new non-dimensional parameter referred to as the excess power parameter (psp) is defined to quantify the P_s difference between the two aircraft. Although a P_s ratio would have been more convenient, it would yield an

unfortunate singularity in instances when the propulsion system is sized for cruise and when both excess powers tend to zero at the design point.

$$psp = \frac{P_{s,ofw} - P_{s,conc}}{v} \approx \frac{D_{conc} - D_{ofw}}{W}. \tag{5.4}$$

With the specific excess power and flight speed indicating the vertical and horizontal distances traversed in a given unit of time, respectively, the *psp* parameter can be rewritten as the difference in flight path angle, χ, between the two aircraft.

$$psp = \frac{\Delta h_{ofw}}{\Delta x_{ofw}} - \frac{\Delta h_{conc}}{\Delta x_{conc}} = \tan\chi_{ofw} - \tan\chi_{conc} \approx \chi_{ofw} - \chi_{conc} \text{ (for small } \chi\text{)}, \tag{5.5}$$

The subsequent figures plot this difference of flight path angle on the right-hand axis in units of radians, with positive values indicating that the OFW can sustain a steeper climb gradient than the Concorde.

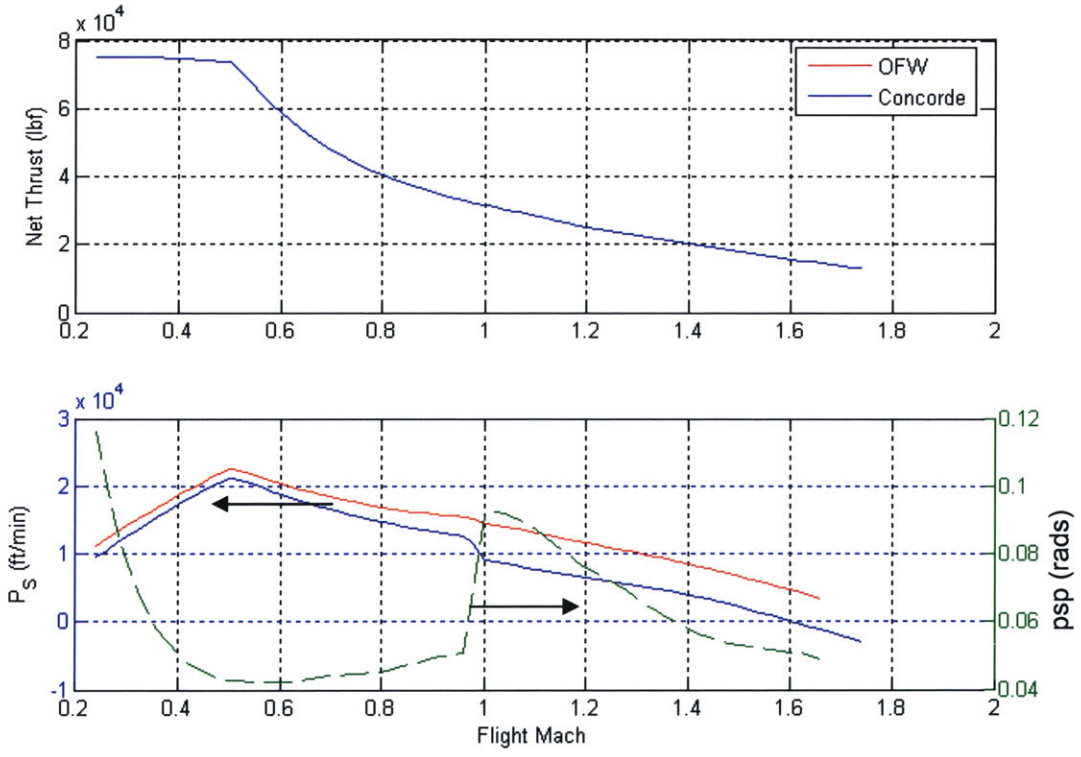

Figure 5.5: Case A – Engines on both aircraft sized for 1000 ft ground roll (red and blue lines read on Ps scale on left; green line is difference in climb gradients)

In this sizing case, the OFW has higher excess power across the entire climb trajectory, with noticeable advantages in the low subsonic and transonic regimes. The time it takes to accelerate through the transonic regime ($0.8 < M < 1.2$) was calculated to be 77s for the OFW as opposed to the 113s for the Concorde. The OFW has a higher ceiling in terms of altitude and speed along this particular trajectory with its excess power exhausted at M1.8 at 58,000 ft as opposed to M1.6 at 56,000 ft of the Concorde.[5]

5.1.3.2 Case B: Sized for Transonic Acceleration

The minimum takeoff T/W ratio necessary for the Concorde to sustain supersonic flight at the design flight condition (M1.6 at 56,000 ft) was found to be 0.75. In this sizing case, the T/W ratio for the OFW was reduced such that its transonic acceleration performance would match that of the Concorde with a T/W ratio of 0.75. With the takeoff T/W ratio reduced to 0.57, the OFW would have the same transonic acceleration time, but a shorter total climb time to cruise altitude (M1.6 and 56,000 ft). Likewise, the OFW has a marginally higher ceiling than the Concorde (approximately M1.65 at 56,500 ft).

[5] Here, ceiling is defined as altitude at which climb rate falls to zero as opposed to the commonly accepted value of 500 ft/s

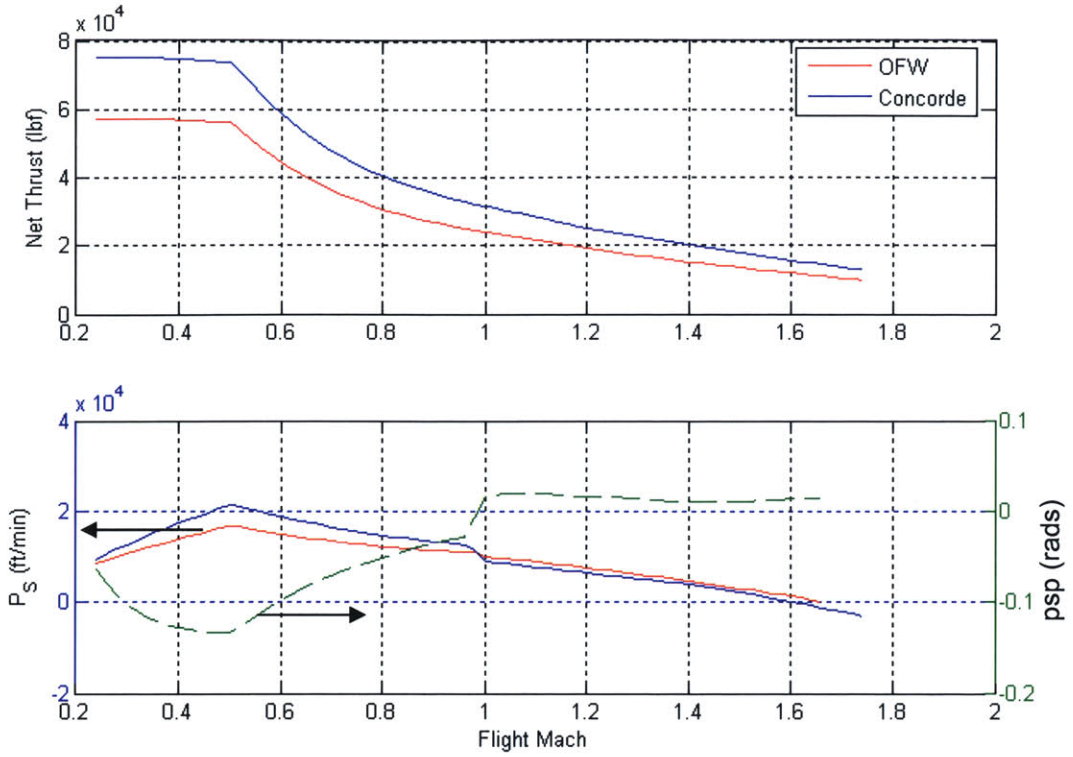

Figure 5.6: Case B – Engines sized to have identical transonic accel. times (red and blue lines read on Ps scale on left; green line is difference in climb gradients)

5.1.3.3 Case C: Sized for Cruise (M 1.6 @ 56,000 ft)

In the last case, the OFW T/W ratio was reduced further such that both aircraft would have zero thrust margin at design cruise conditions. At this takeoff T/W of 0.52, the OFW has noticeably less excess power in the subsonic regime, evidenced by the longer acceleration and climb times in comparison to the Concorde. Incidentally, the cusps in the P_s plots for cases B and C are simply an artifact of the change in ambient temperature that corresponds to the beginning of climb.

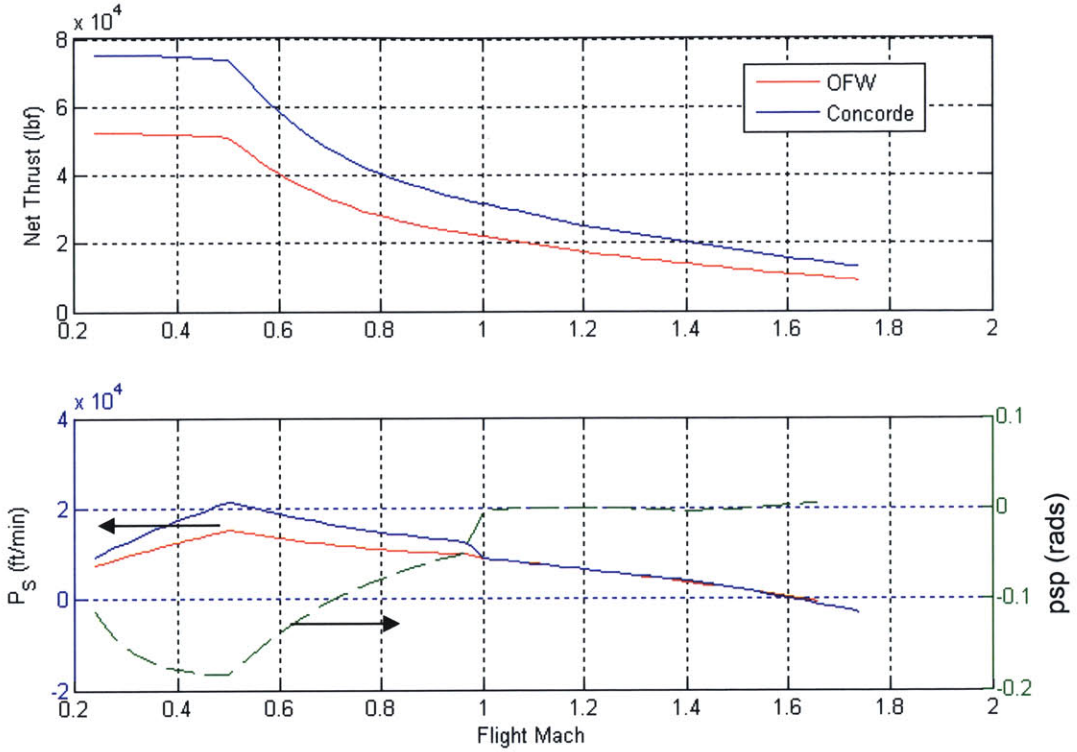

Figure 5.7: Case C – Engines sized to have zero thrust margin at supersonic cruise (red and blue lines read on Ps scale on left; green line is difference in climb gradients)

The results of the three sizing examples have been summarized into the table below

Table 5.1: Climb and acceleration metrics for the three sizing cases

		Case A	Case B	Case C
OFW	Takeoff thrust to weight ratio	0.75	0.57	0.52
	Total time to climb	231s	337s	495s
	Transonic acceleration time	77s	113s	127s
Concorde	Takeoff thrust to weight ratio		0.75	
	Total time to climb		469s	
	Transonic acceleration time		113s	

5.2 Effect of Cycle on Climb Performance

In Section 3.2, it was shown that lower specific thrust cycles could demonstrate an improvement in the integrated propulsion system performance (range parameter) even when considering the effects of nacelle wave drag. For the modified TF30 cycle with BPR 2.4, the critical Mach number that marked the point of diminishing returns in terms of

effective TSFC was found to be slightly above 2. TSFC aside, this section investigates the penalties associated with incorporating lower specific thrust engines in terms of climb and acceleration time degradation. The same three cases are investigated, but with the OFW using the BPR 2.4 engine detailed in Section 3.2, and with the Concorde using the baseline TF30 cycle. Figures 5.8, 5.9, and 5.10 compare the excess power parameter, *psp* (defined in equation 5.3), for an OFW with a BPR 2.4 cycle (in red) against that of the nominal TF30 cycle plotted earlier (in black). For both *psp* curves, the normalization is achieved by differencing the OFW excess parameter with that of the Concorde equipped with TF30 engines (as has always been the case).

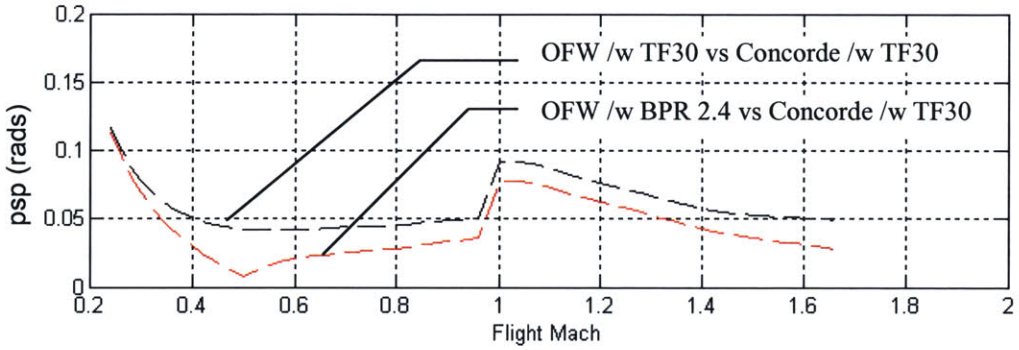

Figure 5.8: Case A – Sized for takeoff (red: BPR 2.4 cycle; grey: TF30 cycle)

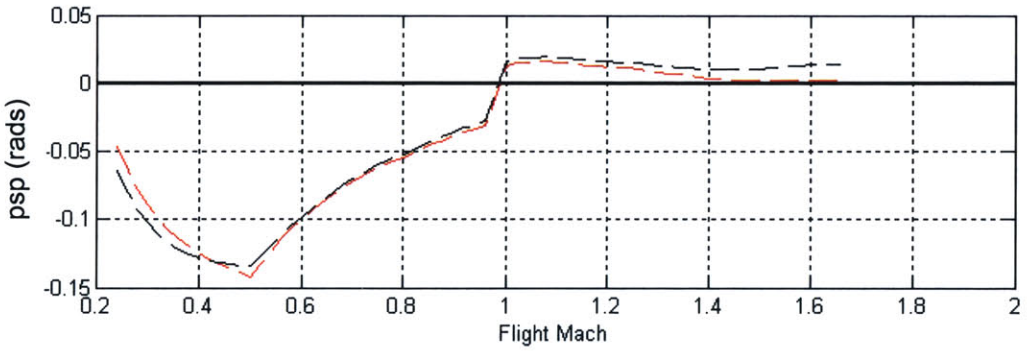

Figure 5.9: Case B – Identical transonic acceleration times (red: BPR 2.4; grey: TF30)

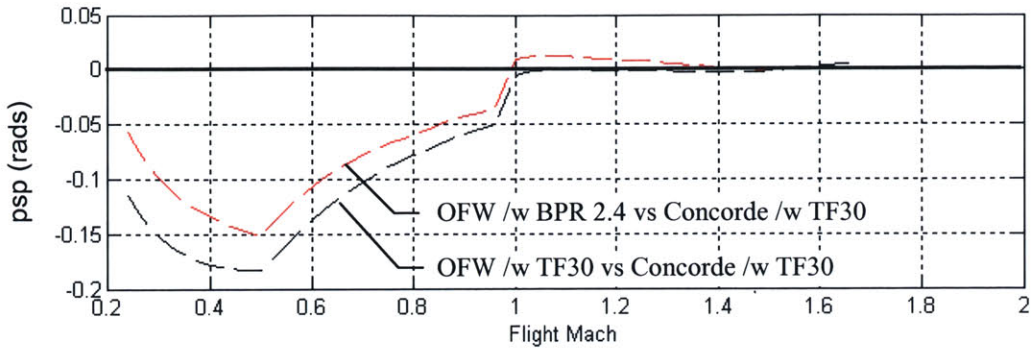

Figure 5.10: Case C – Zero thrust margin at supersonic cruise (red: BPR 2.4; grey: TF30)

Reducing the specific thrust of a cycle brings the *psp* parameter closer towards zero across all Mach numbers. For example, an OFW equipped with higher BPR engines sized for takeoff sustains a climb gradient much closer to that of a Concorde with the TF30 (on average, only 1.43 degrees steeper than the Concorde, as opposed to the earlier difference of +2.75 degrees when the OFW was equipped with the TF30). In cases where the engines are sized for transonic acceleration (case B), the effect of cycle is considerably more subtle—that is, the climb gradient is equally as shallow (-8 degrees difference at M0.5) in the subsonic regime and equally as steep in the supersonic regime (no more than +1.43 degrees difference). Again, these climb gradients are defined relative to those achieved by the nominal TF30 Concorde. For case C in which the engines are sized for cruise, the climb gradient is higher (+1.72 degrees difference) than what it was previously with the TF30 cycle, but still substantially shallower than the Concorde with the TF30 (no more than -8.60 degrees difference). These margins in the climb gradient—both relative to the Concorde and the OFW with TF30 cycles—tends to zero as the flight Mach approaches supersonic speeds. This is indicated by the narrowing of the red and black curves and their convergence to zero.

These trends simply support what was already expected of for lower specific thrust cycles – that they tend to widen the performance mismatch across the extent of the flight envelope. (i.e. A *psp* curve that lies along zero would imply that the engine is just as mismatched

(oversized) as that on the Concorde; similarly, deviations from zero indicate a better balanced thrust margin across the flight regime).

Table 5.2: Climb and acceleration metrics for three sizing cases (OFW with BPR 2.4 cycle)

		Case A	Case B	Case C
OFW	Takeoff thrust to weight ratio	0.75	0.59	0.58
	Total time to climb	258 sec	449 sec	485 sec
	Transonic acceleration time	82 sec	113 sec	116 sec
Concorde	Takeoff thrust to weight ratio		0.75	
	Total time to climb		469 sec	
	Transonic acceleration time		113 sec	

5.3 Engine Integration Concepts

This section proposes two engine integration concepts that address the three major challenges in submerging an engine into the airframe for military survivability reasons. They include

- Dimensional constraints, in which the physical engine must fit within the exterior contours of the airframe; even bulges parallel to the flight direction are unacceptable, as the spanwise component of the flow is supersonic and will lead to additional wave drag
- Flow acceptance at a range of sweep angles
- CG location driven by engine placement

Only the first two challenges are addressed in this section; recommendations pertaining to CG and weight are provided in section 6.1. Section 5.3.1 introduces the turntable concept, and section 5.3.2 provides a detail design of a sample slot-inlet concept for a 100ft-span OFW. The author would like to point out that these sections merely provide a starting point for future work on such concepts.

5.3.1 Considerations for the Turntable Concept

The engines for this concept are mounted flush against a circular rotating disk embedded within the suction surface of the wing. The obvious benefit of this configuration is that by

rotating the disk, the engine can accept the oncoming flow at zero relative angle regardless of the sweep configuration of the OFW.

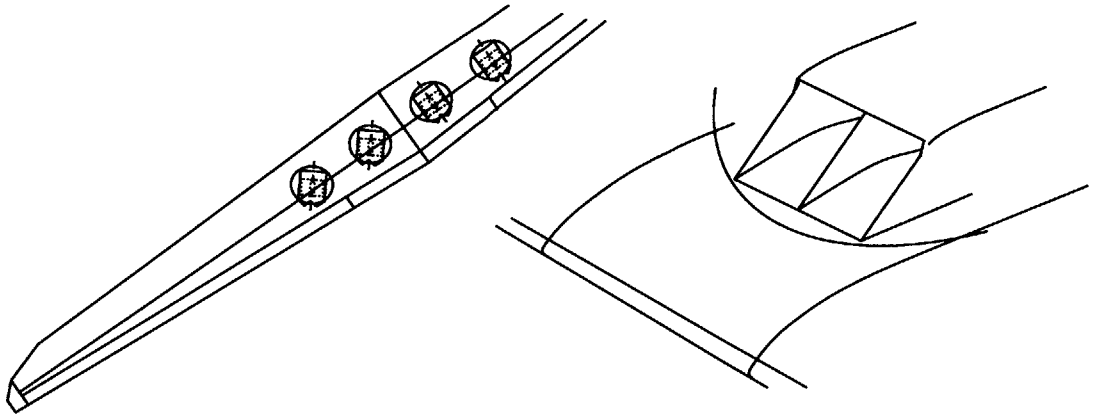

Figure 5.11: Turntable engine concept

With the sweep-accommodating mechanisms limited to the pivoting of the turn table, the engine itself does not require an inlet and nozzle more robust than those that would be typical to a fixed-sweep flying wing aircraft. This engine integration concept poses aerodynamic and structural weight challenges that cannot be ignored—notably, the surface discontinuities that form along the perimeter of the turn table upon its rotation and are not acceptable on supersonic airfoils. However, because its effect on the supersonic aerodynamics is viewed to be more critical than that of the subsonic regime, it may be possible to design so that the surface discontinuities will be manageable off design penalties at subsonic regimes instead of unacceptable penalties at supersonic design point. By orienting the engine on the turntable in such a way that the discontinuities are largest at minimal sweep (low speed) and zero at maximum sweep (supersonic cruise), one can circumvent the most critical aerodynamic penalties. The intent of this section is to investigate the criticality of these discontinuities by comparing their heights to the local boundary layer thickness. The contours in Figure 5.12 below reveal the surface discontinuities for a turntable optimized for 60 degree sweep, with 'hotter' colors indicating that the fixed turntable surface (free-stream reference frame) is higher than the rotated airfoil surface *at that particular chordwise station.*

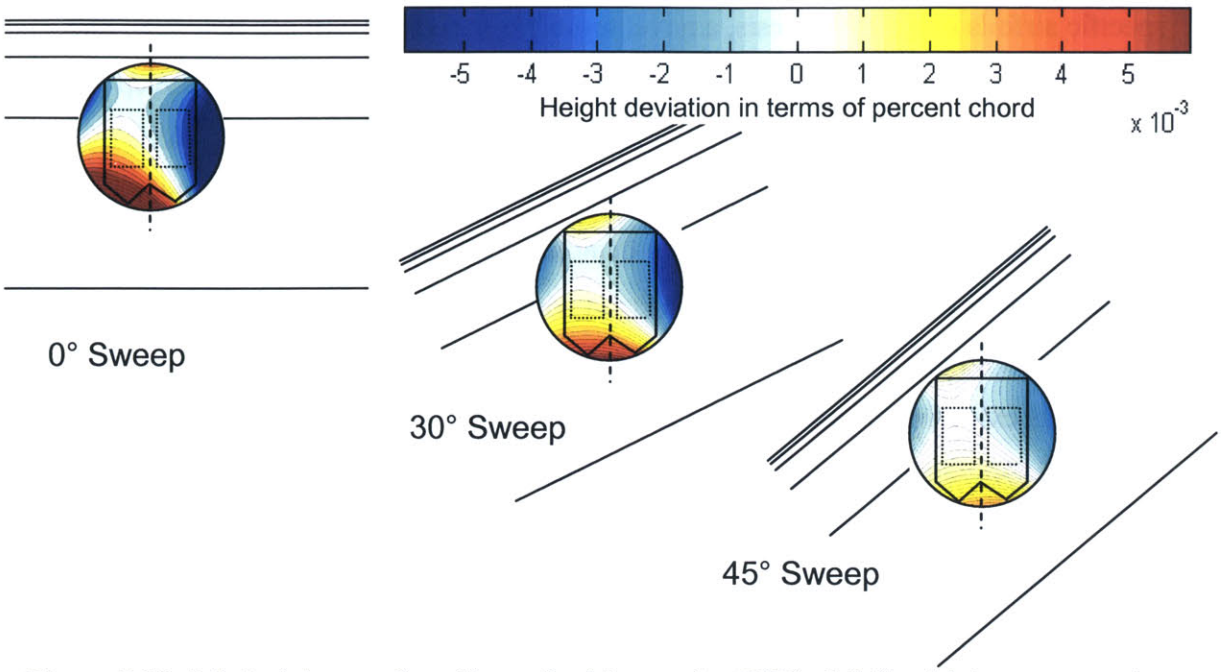

Figure 5.12: Minimizing surface discontinuities on the OW4 airfoil at high sweep angles (expressed in terms of percent chord)

At a sweep angle of 45 degrees, which is the optimal sweep for cruise at M0.9, the largest surface discontinuity at the perimeter is approximately 0.15% of the chord of the wing. For a 60ft span/4.5ft chord OFW, this corresponds to a 0.081in. discontinuity at the fore and aft portions of the turn table. At the 20% chord where the front edge of the initial discontinuity lies, the boundary layer thickness was found via MSES to be approximately 0.08% of the chord for an OW4 airfoil overswept to have an $M_{\perp}$ of 0.65—approximately half the height discontinuity. Although a sufficiently small OFW can conceivably have discontinuities smaller than the boundary layer thickness at the point of interest, it is unlikely that this engine integration concept will be a viable solution at those scales in the first place. The subsequent sections propose solutions for minimizing these surface discontinuities.

5.3.1.1 Minimization of Surface Discontinuities

This section investigates the possibility of tailoring the airfoil, turn table placement, size, and orientation so that flowfield conformity can be achieved without the installation of a flexible skirt around the discontinuity. Much in the same way Butler optimized OFW-

specific airfoils in his 1992 thesis, a novel turntable-friendly airfoil can potentially be optimized so as to limit or even to eliminate the surface discontinuity at all sweep angles. The geometry and section lift and drag characteristics of a sample "flat-top" airfoil is presented in Appendix D. Although its critical Mach number is lower than that of the OW4 (0.70 as opposed to the 0.75), this airfoil demonstrates sufficiently high section L/D and design point C_L to show that the notion is not completely out of the question. Here, Drela's optimization driver, LINDOP, may prove to be an effective tool for further investigation, but such is extensive enough to be a thesis topic in itself, with parameters such as flat-top width and location both being geometric variables that must be traded of for section profile drag. The reduction in critical Mach from 0.75 to 0.70 for the current unoptimized flat-top airfoil corresponds to a reduction in the maximum achievable flight speed from 1.5 to 1.4 if the sweep is to be limited to 60 degrees, and likewise from 2.04 to 2.19 if limited to 70 degrees. For now, this thesis will consider two candidate airfoil geometries – one unmodified OW4 airfoil and another modified by A. Merchant [31] to have an approximate 40% flat region centered around the 45% chord region (Appendix D). The maximum surface discontinuity anywhere along the perimeter of the turn table was plotted as a function of the turn table location for a variety of diameters (Figure 5.13).

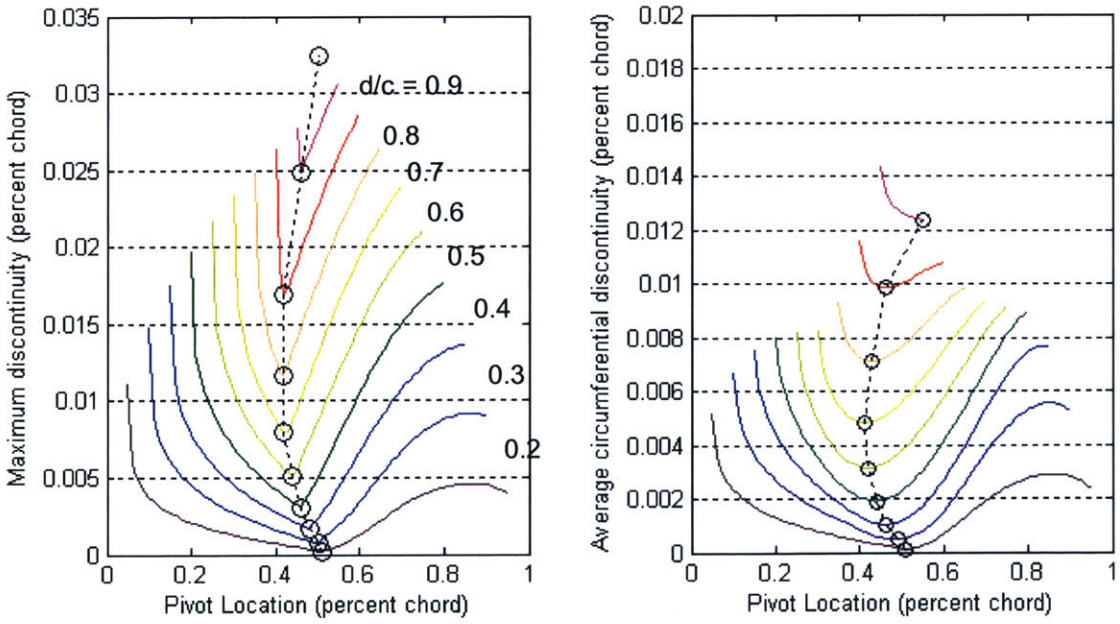

Figure 5.13: Optimal placement of turntables of various diameters on OW4 airfoil

As will be later revealed, a turn table diameter of at least 50% chord is desirable to keep the number of engines within 8. Centered at roughly the 45% chord, this results in a maximum discontinuity equivalent to approximately 0.5% of the chord, or about 0.25 inches for a 60 ft span/4.5 ft chord OFW. A more desirable solution would be to exploit the flat-top airfoil described previously so as to minimize the discontinuities for large turntable diameters. Figure 5.14 below is a similar plot of discontinuity as a function of turntable placement.

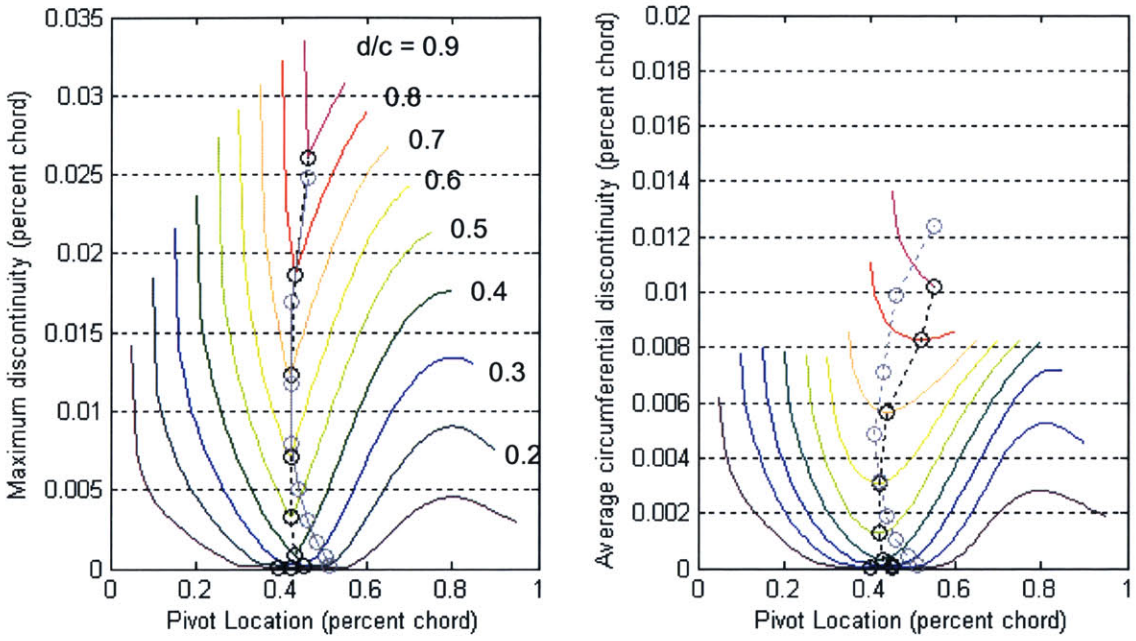

Figure 5.14: Optimal placement of turntable on modified flat-top OW4 airfoil designed by A. Merchant (Appendix D)

The absence of discontinuities for turntable diameters less than 40% are expected of, but improvements can be seen for larger diameters as well. At 50%, the same OFW configuration (60 ft span/4.5 ft chord) that employs a modified flat-top airfoil now has a maximum discontinuity of about 0.3% of the chord, or about 0.15 inches. Moreover, the optimal placement of the pivot point is approximately 10% further forward than of the unmodified airfoil, making it more attractive in terms of CG location.

5.3.1.2 Turn Table Diameter and its Effect on Engine Count

For preliminary engine sizing, the diameter of the n-turntables were made into a variable, defined in terms of the percent maximum chord of the airfoil. Naturally, a small turntable diameter would be the least intrusive to the flow field, with the limiting case being a vertical post onto which the engine is mounted on. However, this would either create gaps between the bottom of the inlet and the top surface of the airfoil or pose clearance issues when an overhanging component pivots into the rising airfoil contour adjacent to the turntable. For this reason, this preliminary study assumes that the total propulsion system length can be no larger than the diameter of the turntable – that is, there is no overhang. Figure 5.15 and 5.16 plots the number of engines required to sustain a 10% thrust margin at supersonic cruise at Mach 1.4 and 2.0, respectively for an OFW with AR of 16 and t/c of 0.12. The engine used for this trade study is a rubber GE F-110 engine cycle with a BPR of 0.8 and FPR of 2.98 – one that yields specific thrust values very similar to the TF30 cycle employed earlier.

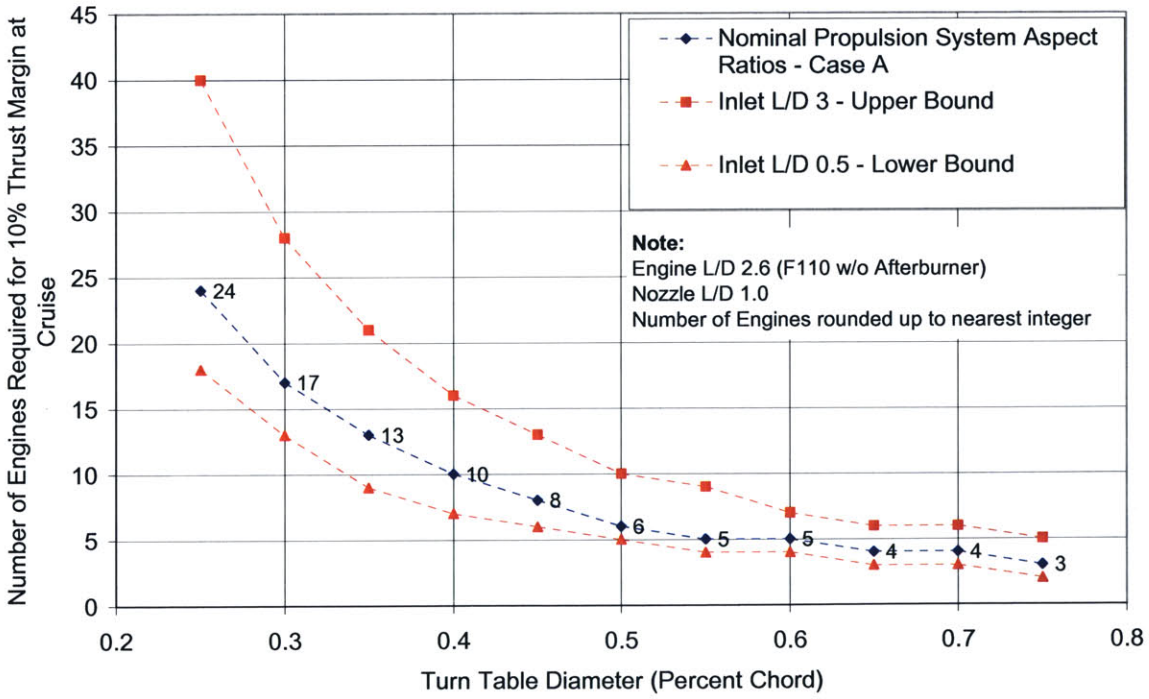

Figure 5.15: Engine count vs. turn table diameter for M1.4 cruise

For the M1.4 design point case, a normal shock inlet is employed because of its minimal length and near perfect pressure recovery. Based on the required area ratio of the subsonic diffuser ($A_2/A_1 = 1.25$), the total inlet length to diameter ratio of 1.5 was found to yield a subsonic diffuser pressure recovery of 0.96, which combined with the normal shock pressure ratio, results in an overall inlet pressure recovery of 0.94.

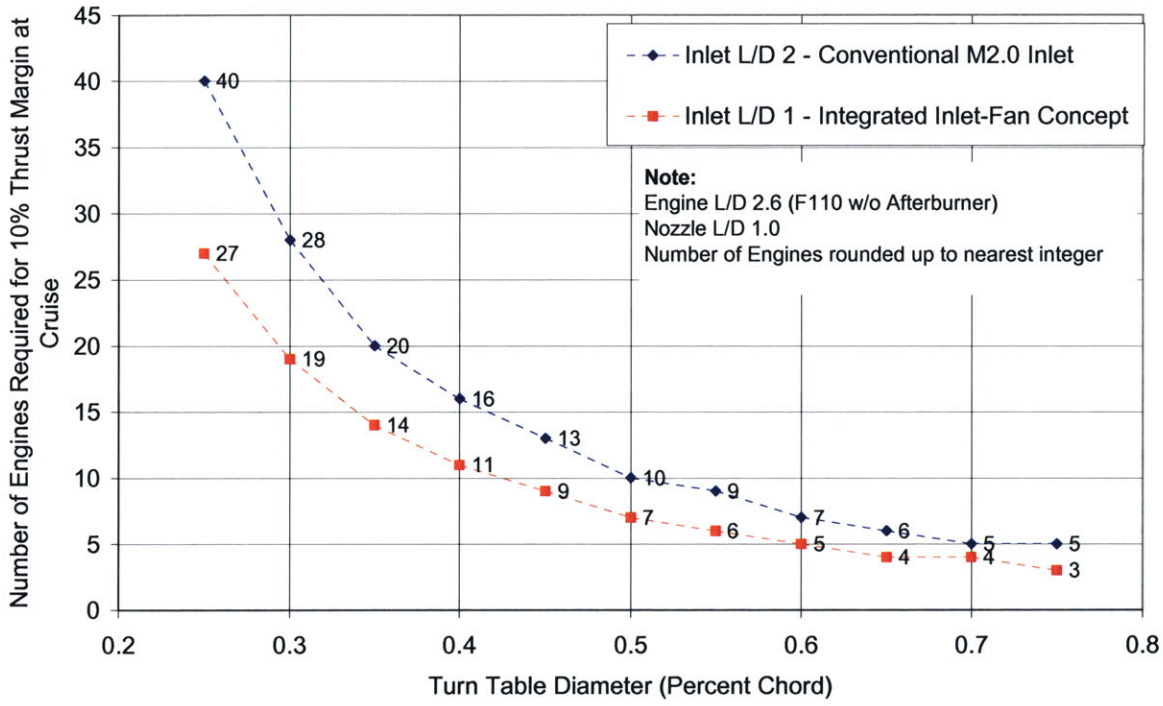

Figure 5.16: Engine count vs. turn table diameter for M2.0 cruise

5.3.1.3 OFW Aspect Ratio and its Effect on Engine Count

Interestingly enough, the required engine count for OFWs with lower aspect ratios (10) were not any higher than higher aspect ratio OFWs with the same turn table diameter—this, despite the fact that simple dimension analysis reveals a mild aspect ratio dependence on the engine diameter to chord ratio of two aircraft with everything else the same. Combining the expression for drag coefficient and aspect ratio, the drag coefficient can be related to thrust required to sustain level flight:

$$C_D \sim \frac{DAR}{\frac{\gamma}{2}PM^2b^2} \sim \frac{TAR}{\frac{\gamma}{2}PM^2b^2}. \tag{5.6}$$

By dropping the terms that are independent of aircraft geometry and by rewriting the thrust of a fixed-cycle engine in terms of the engine diameter, *d*, the expression becomes

$$C_D \sim \frac{d^2AR}{b^2} \Rightarrow \frac{d^2}{b^2} \sim \frac{C_D}{AR}. \tag{5.7}$$

Nondimensionalizing the engine diameter by the root chord reveals a weak dependence on aspect ratio as follows:

$$\frac{d}{c} \sim \sqrt{C_D AR} \quad or \quad \frac{d}{t} \sim \sqrt{C_D AR}, \tag{5.8}$$

where in this case, *c* is the OFW chord. If the *total* drag scales as the inverse of the aspect ratio as follows

$$C_D = C_{Di} \Leftrightarrow C_D \sim AR^{-1}, \tag{5.9}$$

then the diameter-to-thickness ratio would lose its dependence on aspect ratio, as is seemingly the case here:

$$\frac{d}{c}, \frac{d}{t} \neq f(AR), \tag{5.10}$$

where once again, d/c and d/t are the ratio of engine dimensions to OFW scale. This aspect ratio invariance, is unlikely to be the case unless the induced drag term is the dominating drag term. Much more conceivable is the fact that, just for the few representative aspect ratios investigated (10 and 16), the change in chord available on which to mount the propulsion system was offset just as equally by the change in engine size necessary to compensate for the additional induced drag. Based on the results of this aspect ratio trade study and the dimensional analysis above, lower AR OFWs are to the first order, no more or less geometrically constraining for propulsion systems that must be integrated into wing.

5.3.2 Stagnation Point (Slot) Inlet

The stagnation point inlet takes advantage of the free isentropic compression that takes place at the leading edge, thereby reducing the inlet Mach number and the related shock losses. The flow vector into the inlet consists of the constant spanwise component of the free stream and what will be referred to as the normal "suction-induced" component normal to the leading edge, although this term is a misnomer since the supersonic flow does not feel the effects of the engine upstream of the slot. Rather, it is the absence of compression waves that typically emanate from the upstream leading edge, which prevents the flow from turning completely parallel to the span; hence some of the normal component is retained. Inlet guide vanes turn and diffuse the incoming flow from its initial direction and Mach number to those that satisfy the flow conditions necessary at the front face of the engine.

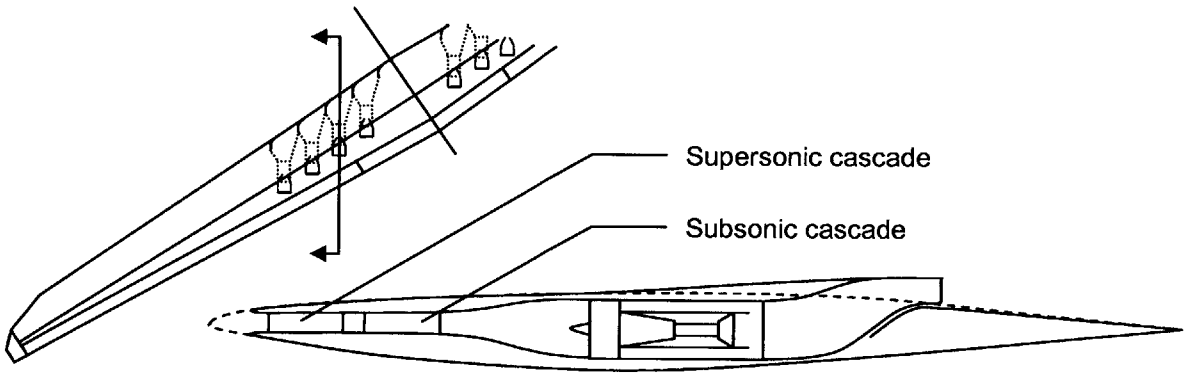

Figure 5.17: Stagnation point inlet concept

The major design parameters that must be optimized for the slot inlet include inlet blade angle, slot width, height, and engine installation angle, all of which affect the achievable inlet pressure recovery and the chordwise placement of the engine. For example, a large slot (as viewed from directly in front) which accepts the incoming flow at an angle nearly parallel to the leading edge will have the same inlet capture area (flux) as a smaller slot with a more normal velocity component, but will have made better use of the 'free' isentropic compression. The designs that make the most use of the free isentropic compression will have an inlet cascade Mach at or slightly above the spanwise Mach component of the airfoil, approximated by

$$M_{span} = M \sin \Lambda \,. \tag{5.5}$$

Figure 5.22 plots typical cascade inlet Mach numbers as a function of flight speed for an OFW with a constant-normal Mach sweep schedule, as explained earlier. Variable inlet guide vanes provide several worthwhile merits for the slot inlet, including: 1) improved airflow matching across all speed regimes and 2) minimal spillage at off-design conditions. Its mechanisms resembling that of Venetian blinds, its function is analogous to a translating/collapsing center body of an axisymmetric inlet.

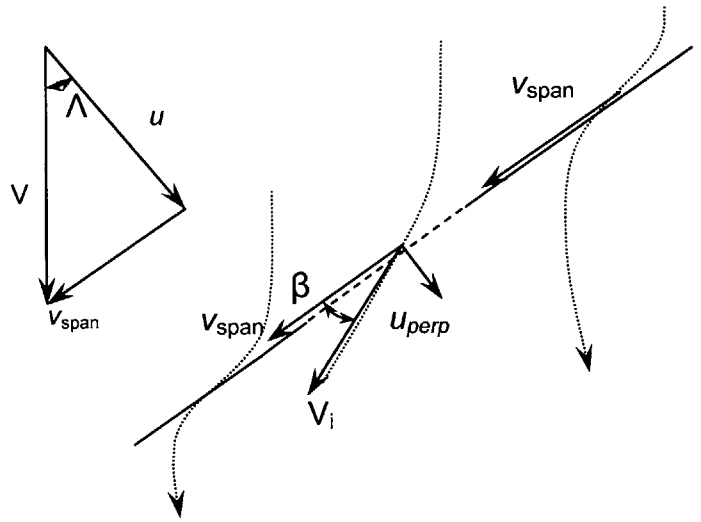

Figure 5.18: Velocity triangle at cascade inlet

5.3.2.1 Preliminary Sizing

A preliminary cascade sizing study was carried out via 1D compressible flow analysis in which only one row of cascades would diffuse the flow and in which the only loss mechanism was assumed to be normal shock losses[6]. A separate subsonic cascade and the viscous losses within it will later be considered once an appropriate blade scheduling scheme is established. Table 5.3 below summarizes the 5 cases considered, of which 3 are variable angle and 2 are fixed. The blade angles for the former three cases are plotted as a function of Mach in Figure 5.19. For preliminary sizing, the slot inlet is assumed to consist of only a supersonic cascade that diffuses the flow from the inlet flow angle and Mach to

[6] Actual shock losses will not be as severe as that dictated by a normal shock

the engine front face. These assumptions are considered sufficient for the purposes of calculating key area ratios if the flow is assumed to be inviscid and if the deceleration mechanisms are assumed to be isentropic with the exception of shocks. The diffusion will be split up into a supersonic and a subsonic cascade in section 5.3.2.3, when losses due to diffusion are considered.

Table 5.3: Cascade blade angle scheduling cases

	Case A	Case B	Case C	Case D	Case E
Flight Mach limit	1.8	1.8	1.8	1.3	1.5
Blade angle at inlet, β_i	Variable	Variable	Variable	35°	30°
Blade angle at exit, β_o	Variable	Variable	Variable	45°	38°
Turning angle, β_o-β_i	21.43°	15°	10°	10°	8.16°
Cascade exit Mach, M_o	~0.3	~0.35	~0.4	~0.45	~0.45
Engine installation angle, ε	~50°	~40°	~35°	45°	38°

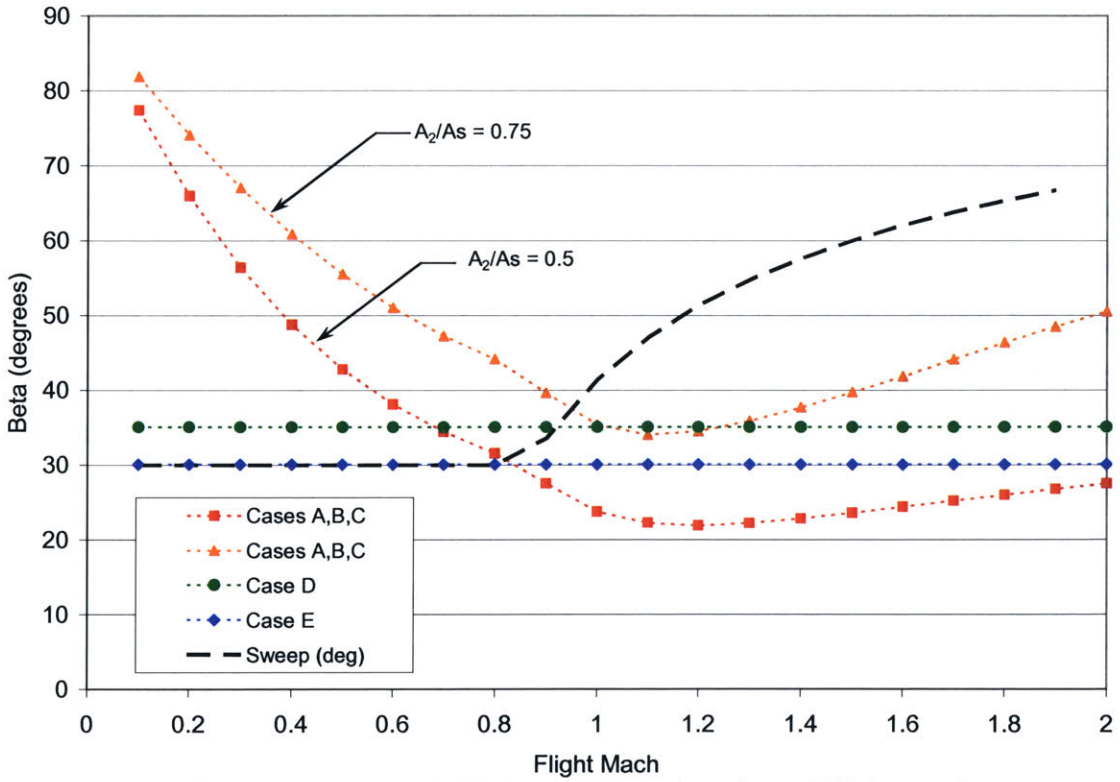

Figure 5.19: Cascade blade angle as a function of flight Mach

In Figure 5.19, A_2/A_s is the area ratio between the engine front face and the slot as viewed from a direction directly perpendicular to the leading edge, and is a free parameter in this case. The benefit of a small A_2/A_s is that since the flow capture area is larger, the incoming flow can achieve more isentropic compression before entering the slot at a smaller β and lower M_i (Recall, small β's correspond to flow that is more parallel to the leading edge). For the two cases investigated above, increasing the flow capture area by 50% provides the benefit of increasing the flight Mach number at which the flow into the inlet becomes supersonic—M1.2 for A_2/A_s=0.5 and M1.1 for A_2/A_s=0.75. Furthermore the upper limit to the flight speed at which the inlet cannot pass the required mass flow is increased from 1.3 to 1.75. This is referred to as the flight mach limit and will be discussed in section 5.3.2.2. Incidentally, for an A_2/A_s of 0.5, the slot width of a 100 ft span OFW is later calculated to be 4.0 ft, assuming 8 GE-110-type cycle engines distributed across the span of the wing. This corresponds to a cumulative slot width of 32 ft—approximately 1/3 of the span of the wing. Subsequent reductions in A_2/A_s must take into account the span available on which the slots will be distributed.

The engine installation angle is defined as the angle that the engine axis makes with the leading edge of the wing (90° being the conventional orientation). This section does not address extensively how to accommodate the need to have variable flow direction at the engine exit, but nevertheless tries to minimize the angle that the engine makes with the free stream so as to mitigate these concerns. An engine installation angle close to the sweep angle at all flight speeds is ideal and will reduce the directional extents of the vectored thrust.

5.3.2.2 Supersonic Cascade Blade Scheduling (Cases A,B and C)

For the variable angle cases, the blade angle sought at each Mach was such that the front face of the engine would retain a constant Mach number of 0.5. Hence, the variable angle blade schedule is the ideal solution for achieving engine-inlet airflow matching at off-design cruise conditions. The bucket shape results from the high corrected mass flow near

the transonic regime, which necessitates a smaller flow capture area (low β). Furthermore, this type of blade scheduling has what will be referred to as a high flight Mach number limit, in which a given slot area can pass the required mass flow to the engine even at high Mach numbers. This Mach number limit is based on the assumption that the incoming supersonic flow cannot turn inward towards the leading edge such that its normal component is greater than it is at free stream (i.e. the greatest flux into the slot is achieved when the free stream air dives straight in without any outward turning). Flights at speeds above this flight Mach limit must be with the engine operating at reduced mass flow (lower M_2). Figure 5.20 below plots the "worst-case" shock-related pressure recovery for each of the blade scheduling cases in which a normal shock is assumed the lie at the minimum channel width. Again, the actual shock losses are not expected to be as high as that dictated by this analysis.

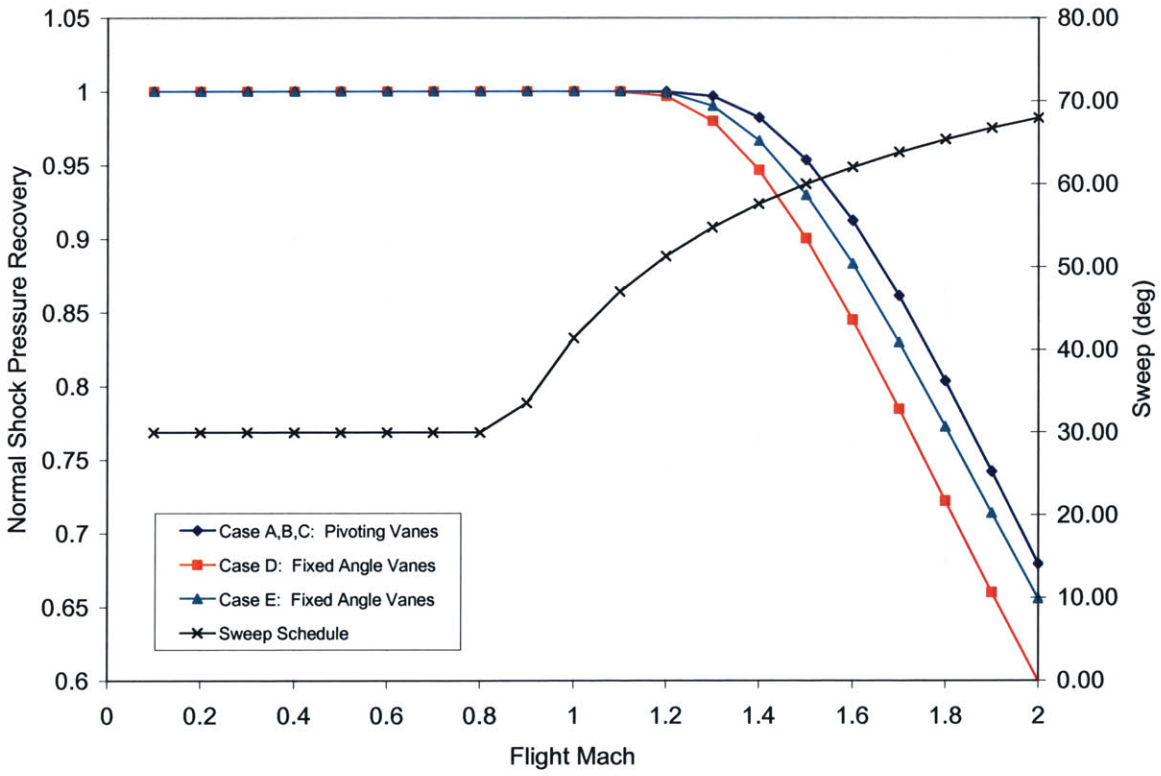

Figure 5.20: Inviscid normal shock pressure recovery as a function of flight Mach

Although the variable-angle blade schedule is shown to have the highest normal shock pressure recovery across the supersonic regime among the three blade angle case, it was also found that the variable-angle case tends to over-diffuse the flow because of their high blade turning angles (21°, 15°, and 10°, respectively). The result is cascade exit Mach numbers that are lower than what was initially desired at the engine front face (M0.5), as evident in Figure 5.21. On the other hand, the two fixed-angle cases maintains the exit Mach to within M0.05 of M0.5 for a larger range of flight speeds—from approximately M0.9 to M1.7—although with much greater deviations at subsonic Mach numbers below 0.5. In the subsonic flight regimes where the cascade exit Mach is denoted to be substantially lower than what is desired, the actual values are expected to be higher due to the influence of the engine on the upstream streamtube capture area—that it *is* possible for the flow at the inlet of the cascade to be larger than the flight Mach number. In extreme cases, blow-in doors may provide additional airflow at low speed operations, but the notion is not addressed any further in this thesis.

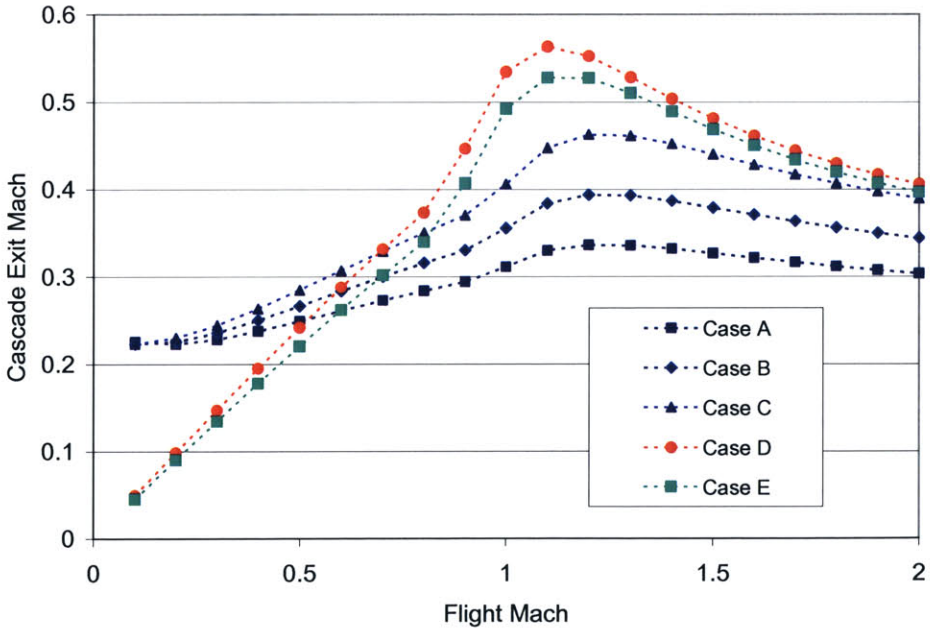

Figure 5.21: Mach number at the exit of the supersonic cascade

To minimize the overdiffusion that arises from the variable-angle blade schedule, a custom blade with a 7° turning angle was designed by A. Merchant (Appendix E). Figure 5.22 below plots the flow angles and Mach (the same metrics plotted in Figures 5.21 and 5.19) as a function of flight Mach for this custom blade. Note that the flight Mach limit is denoted as the point where the required supersonic cascade inlet Mach exceeds the flight Mach (intersection between the grey line with slope 1 and the solid black line).

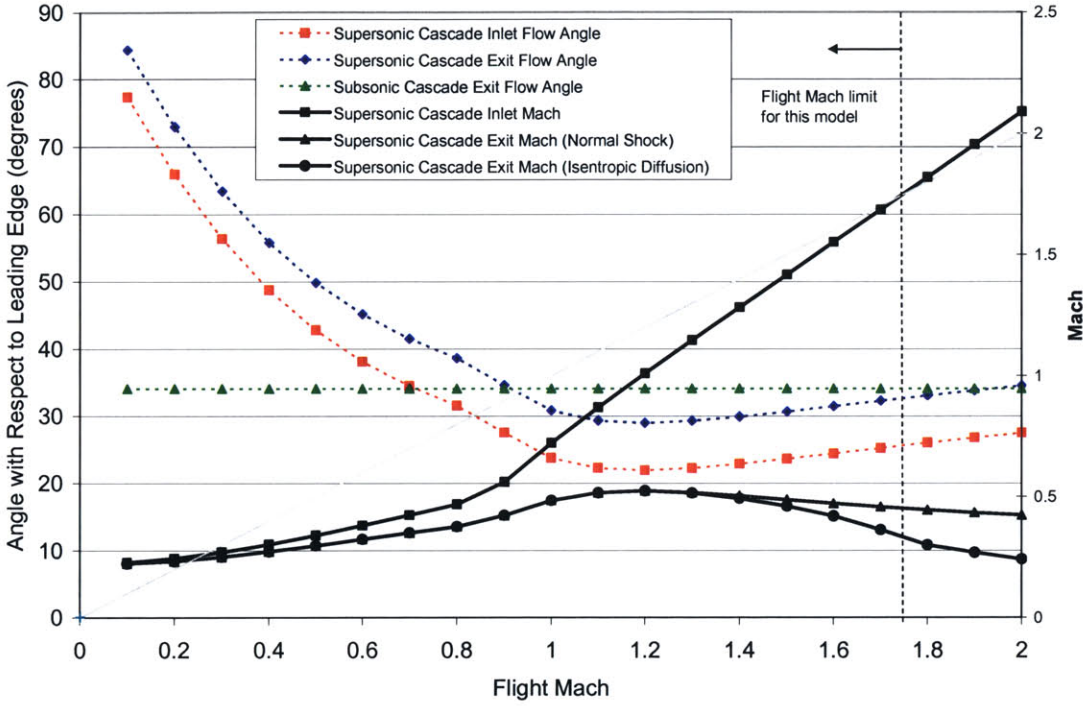

Figure 5.22: Variable supersonic cascade blade angle with 7° turning angle

As evident from Figure 5.22, this blade schedule successfully maintains a near constant supersonic cascade exit Mach of 0.5 throughout the supersonic regime if purely isentropic diffusion is assumed (denoted by the higher of the two branches in the solid black curve). Note that the actual solution is expected to be somewhere in between this ideal isentropic solution and the normal shock solution, but sufficiently invariant of flight Mach to provide adequate airflow matching.

5.3.2.3 Blade Sizing

Supersonic and subsonic blade rows allow for diffusion to take place in a smaller streamwise length than would otherwise be possible in a variable-area duct. In fact, both the blade solidity and aspect ratio are free variables that govern the dimensions of a cascade with particular diffusion requirements—high solidity and aspect ratio for smaller dimensions, and low solidity and aspect ratio for larger dimensions. For a fixed amount of turning, high solidity decreases the diffusion losses at the expense of an increased total weight of the cascade. In addition, from the perspective of a 2-D semi-infinite cascade, a high aspect ratio is beneficial in that it scales down the dimensions of the blades, although at the expense of total blade count and surface area to yield in more friction drag. For turbomachinery, the maximum aspect ratio may be limited by radial blade stresses or susceptibility to flutter, whereas for stationary cascades, such as in this case, it may be limited by the minimum Reynolds number [27]. In this analysis, the Reynolds number at the worst case regime (56,000ft, M_i=0.8 is assumed to set the lower limit to the size of the blades—$1x10^6$ for the supersonic cascade and $5x10^5$ for the subsonic cascade.

Based on the following iterative procedure, the supersonic and subsonic cascades of a sample slot inlet were sized (dimensions of slot and blades provided in Appendix E):

- Select minimum acceptable Reynolds number
- Find chord length that corresponds to the above Reynolds numbers at the limiting case (low Mach and high altitude)
- Know the height of the slot → blade aspect ratio falls out
- Know the width of the slot → calculate the number of blades
- Guess solidity
- Calculate the upper and lower bound to the subsonic diffusion losses
- Recalculate solidity based on the extents of the diffusion factor
- No diffusion takes place in the transition duct (duct inlet to exit area ratio equal to unity)

To estimate the losses within the supersonic cascade, this thesis accounts for the diffusion and shock losses independently and combines the two to obtain the cumulative value. Although [27] states that the actual losses have historically been worse than those estimated by this method, it is assumed to be a sound starting point for the future design of this engine integration concept. Figure 5.23 plots a range of expected diffusion factors as a function of flight Mach for three types of flow deceleration mechanisms—one in which subsonic diffusion takes place within the complete region between the cascade inlet to the exit; another in which diffusion takes place solely downstream of the leading edge normal shock; and a third in which diffusion takes place as if it is the only deceleration mechanism (no shock losses). Again, the actual solution is expected to be bound by the two extreme cases (cases II and III).

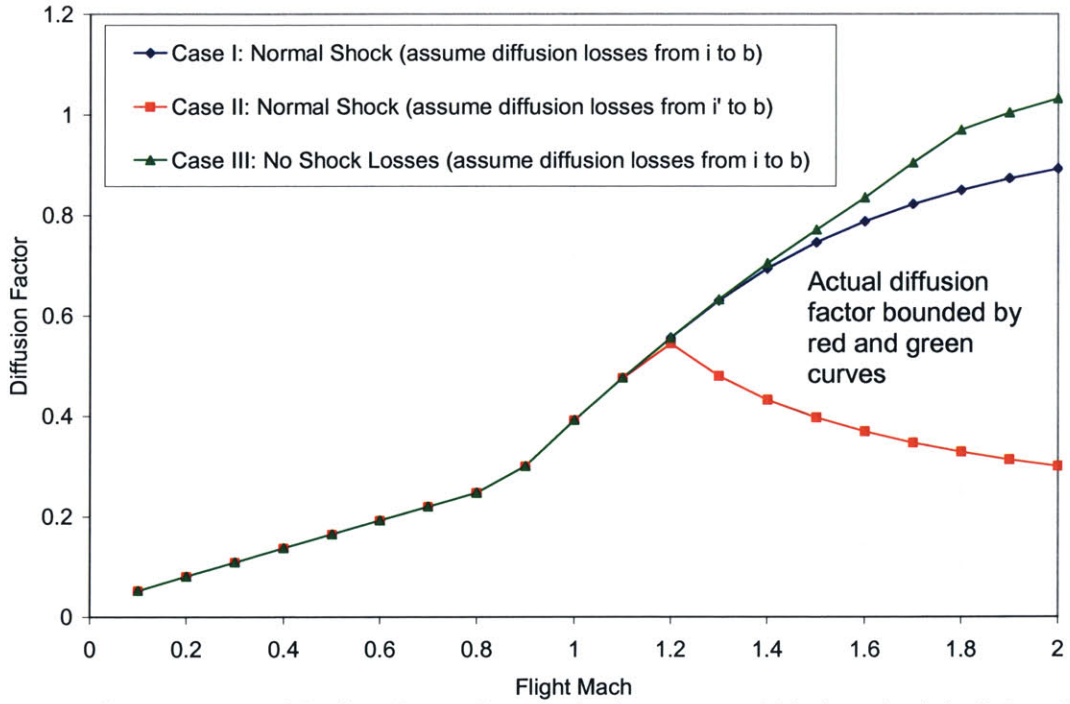

Figure 5.23: Diffusion factor for nominal sweep and blade schedule (c/s = 2)

A solidity of two was found to yield an average diffusion factor slightly less than 0.6, which according to the loss parameter correlation provided in [27], is the diffusion limit before incurring substantial additional losses. Figure 5.24 below correlates the diffusion factor to the stagnation pressure ratio across the cascade for all three cases (I, II, and III),

and shows that a pressure ratio of 0.92 can be achieved by a diffusion factor of 0.6. Figure 5.25 correlates Figures 5.23 and 5.24 to plot the diffusion related pressure recovery as a function of flight Mach number. Note that because of the uncertainty in the diffusion factor estimates of Figure 5.23, the highest flight Mach number at which a pressure recovery higher than 0.9 is expected is M1.3.

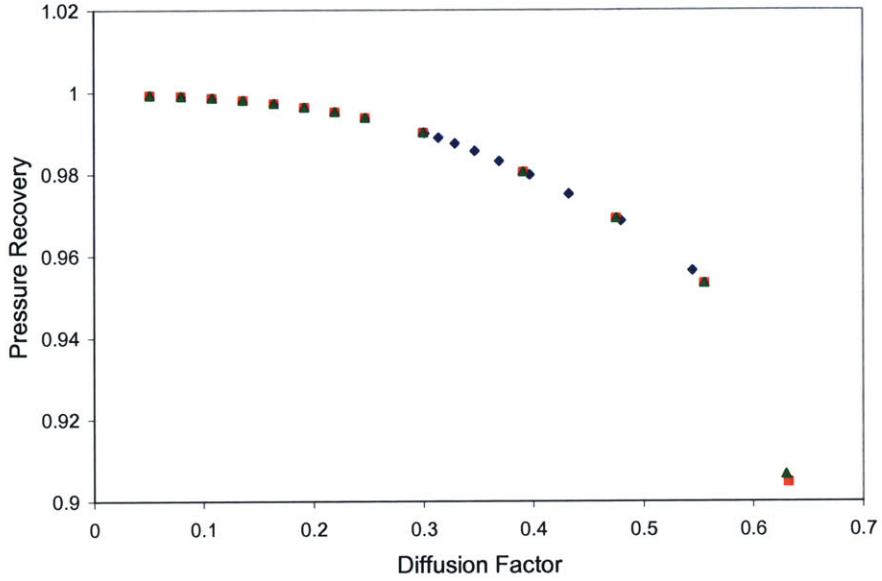

Figure 5.24: Correlation of pressure recovery to diffusion factor (c/s = 2) [27]

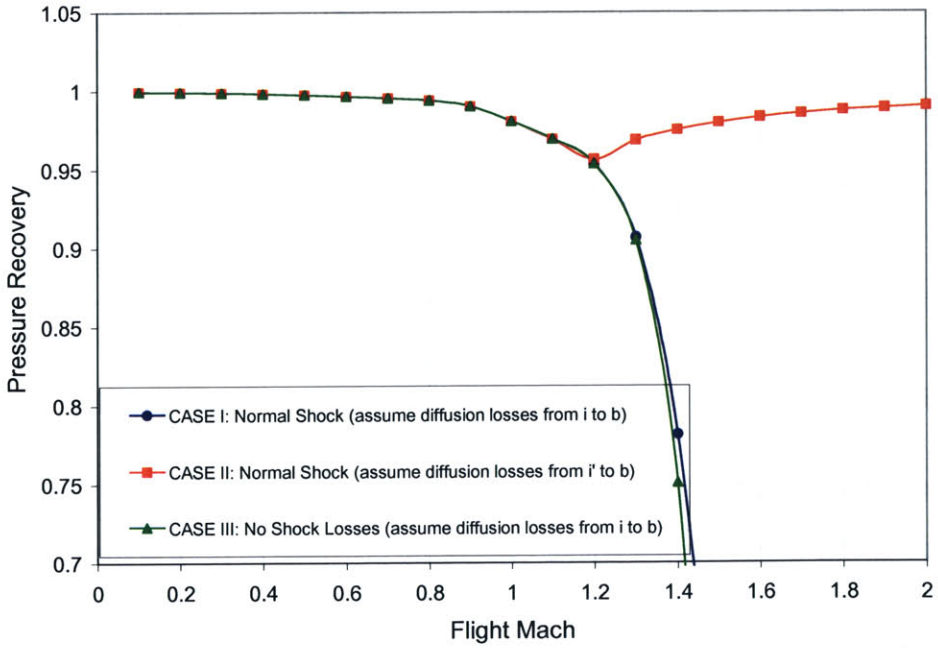

Figure 5.25: Diffusion related pressure recovery as a function of flight Mach (c/s = 2)

Chapter 6

Summary and Conclusions

This thesis addressed the current state of OFW-related technologies and developments; developed synthesis methodologies for assessing integrated aero-propulsive performance; reinforced its purported aerodynamic and range performance advantages over supersonic transports with conventional wing-body configurations; and addressed key issues on two novel engine integration concepts. In this section, the major 'takeaways' from each section are recapitulated and suggestions for future OFW research provided.

Although the theoretical OFW aerodynamic performance is already established to be superior to conventional subsonic and supersonic aircraft configurations, the extent to which an actual operational OFW can approach the theoretical limit depends on the criticality of the stability and control, and the propulsion integration requirements, only the latter of which has been addressed in this thesis. The recent DARPA 'Switchblade' project, on the other hand will—upon its completion—reveal whether modern control schemes can provide adequate flying characteristics at high sweep necessary for supersonic flight (60 degrees at M1.4). Propulsion integration, however, is not within the scope of the project.

The maximum achievable L/D of an OFW with the nominal OW4 airfoil and aspect ratio 16, optimized for cruise at 56,000 ft was found to be 30 for loiter at M0.4, 25 for optimal subsonic cruise at M0.9, and 10 for supersonic cruise at M1.6. Although somewhat affected by altitude trajectory, L/Ds were found to be much stronger functions of sweep schedule, especially at high supersonic cruise—with the general trend being that

oversweeping the wing such that the normal Mach is substantially lower than the critical section Mach improves the L/D by up to 40% at speeds near M1.6 . Unfortunately, the optimal sweep angles at these speeds almost always exceed the admissible limit dictated by stability and control considerations (70 degrees).

It was also shown—although anticipated from before the undertaking of this project—that the OFW experiences a much smaller (approximately half) drag rise in the transonic regime due to the absence of the additive "shock-induced" profile drag. For this reason, the optimal time to climb trajectory for an OFW with the same propulsion system as that of a conventional wing-body configuration does not necessarily require a transonic dive along a constant energy-height curve, as is often the case for its symmetric-wing counterpart.

In terms of cycle selection, it was found that lower specific thrust cycles encourage higher range parameters for cruise speeds up to M2.0 for $T_{t4}/T_{t2} = 5$, and M 2.2 for $T_{t4}/T_{t2} = 6$, above which the uninstalled TSFC reductions are not enough to offset the mounting nacelle wave drag. Due to the geometric constraints of a very volume-limited OFW, lower specific thrust cycles become less of a feasible option, however, if one were to require the engine to be integrated into the airframe. In fact, it may be necessary to regress the TSFCs by reverting to a higher specific thrust engine, if we are to consider operability and practicability. In cases such as these, the high aerodynamic efficiency of the OFW more than makes up for the less than optimal TSFCs—the end result being a range parameter that is still modestly better than what a conventional wing-body configuration can promise.

In terms of engine sizing, it was shown that when OFW engines were sized under the same criteria as conventional wing-body configurations, the OFW excess power curves were characteristic of high-thrust fighters, which do not benefit from constant energy-height dives to minimize time to climb. And like most conventional wing-body configurations (including the Concorde), OFW engines sized for supersonic cruise were still found to be oversized for takeoff, although not to the extent of former. For example, a takeoff T/W

ratio of 0.4 is required for a takeoff ground roll distance of 2000 ft, both for the OFW and the Concorde. However, the Concorde requires a static T/W ratio of 0.75 to sustain level flight at the supersonic design point. The OFW, on the other hand, requires a T/W of 0.52.

6.1 Recommendations for Future Work

This section provides a list of recommendations for future work pertaining to the integrated aero-propulsive performance of the OFW and the author's rationale for proposing each task

- Develop a higher fidelity aerodynamic model to obtain more accurate aerodynamic predictions (i.e L/D) to reveal exactly how critical the structural and propulsive performance metrics are if the OFW is to achieve a target mission range requirement; achieved via the implementation of the following tools:
    - vortex lattice model for the estimation of lift-dependent drag
    - 3D Euler code for the estimation of volume dependent wave drag
- Develop a propulsion system weight model to assess the criticality of the engine cycle selection and the propulsion system placement on the static stability
- Conduct a parameter sensitivity study to quantify exactly how critical the final figure of merit (range parameter) is to each design parameter (i.e d(L/D)/d(AR) |(const payload and range) centered about the baseline case

Appendix A: Mission Modeling Methodology

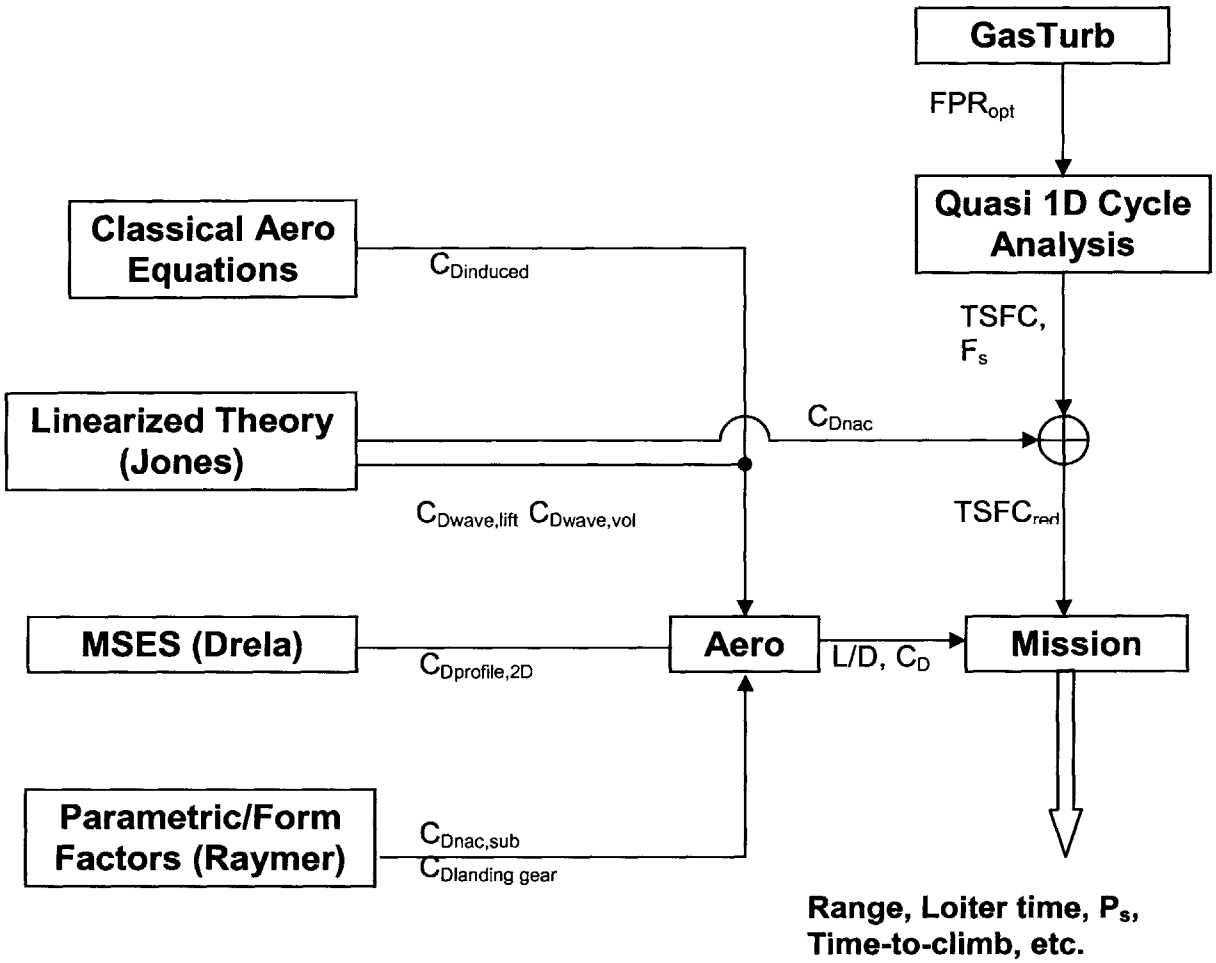

Appendix B: Baseline Airfoil Characteristics

Below is the surface pressure distribution of the baseline OW4 airfoil operating at its design point.

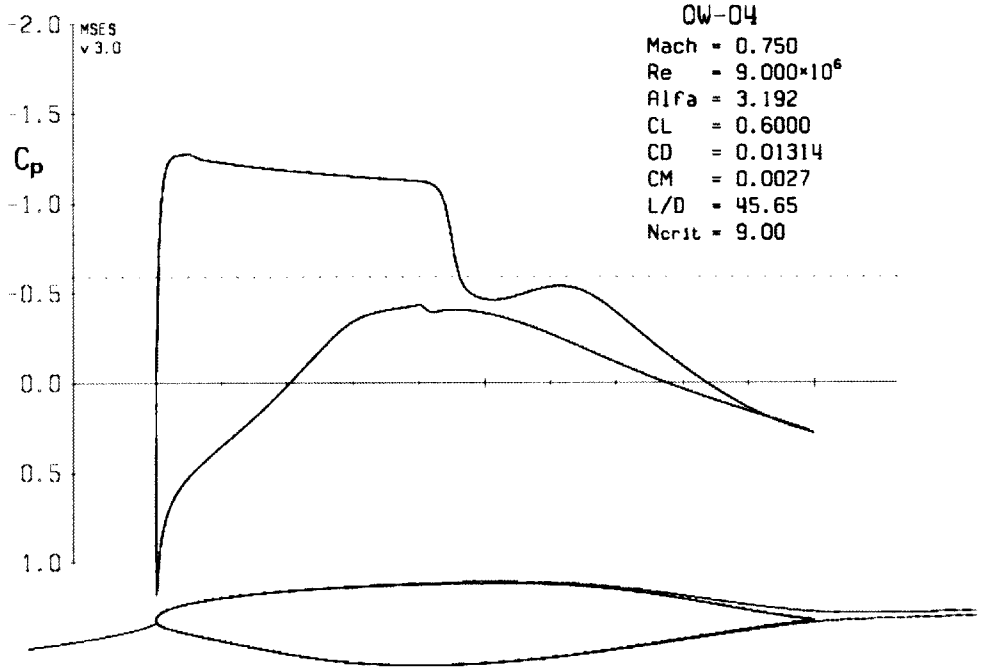

Here, the results of a very arduous computational process has been condensed into two tables—one for the section profile drag and another for the friction drag. The Reynolds number for all combinations of Mach and lift coefficient were held constant at Re=9x10^6; the pressure and friction drag at a particular operating point were obtained by linearly interpolating between the 4 points of the table below and by applying a Reynolds number correction to the friction drag term (equation 2.11).

C_{dp}		M						
		0.2	0.3	0.4	0.5	0.6	0.7	0.75
C_l	0	0.000945	0.000992	0.001066	0.001183	0.001376	0.001753	0.002852
	0.05	0.000982	0.001029	0.001106	0.001226	0.001424	0.001810	0.002501
	0.1	0.001026	0.001078	0.001156	0.001279	0.001483	0.001880	0.002377
	0.15	0.001082	0.001133	0.001213	0.001342	0.001552	0.001961	0.002401
	0.2	0.001148	0.001200	0.001283	0.001413	0.001629	0.002052	0.002497
	0.25	0.001224	0.001278	0.001363	0.001497	0.001719	0.002157	0.002617
	0.3	0.001316	0.001370	0.001455	0.001593	0.001822	0.002275	0.002759
	0.35	0.001450	0.001513	0.001601	0.001742	0.001965	0.002405	0.002988
	0.4	0.001603	0.001660	0.001757	0.001913	0.002196	0.002573	0.003510
	0.45	0.001758	0.001404	0.001486	0.002150	0.002470	0.003372	0.004347

	0.5	0.001966	0.001964	0.001689	0.002441	0.002924	0.004561	0.005372
	0.55	0.002188	0.002154	0.002361	0.002990	0.003055	0.006386	0.006646
	0.6	0.002351	0.002703	0.002664	0.003180	0.003173	0.008000	0.008303
	0.65	0.002581	0.002533	0.002962	0.003884	0.005259	0.009000	0.010586
	0.7	0.002856	0.002971	0.003308	0.005003	0.010372	0.010000	NaN
	0.75	0.003187	0.003398	0.004091	0.007323	0.015603	NaN	NaN
	0.8	0.003448	0.003684	0.007896	0.030180	0.050958	NaN	NaN
	0.85	0.003775	0.004034	0.011767	NaN	NaN	NaN	NaN
	0.9	0.004100	0.004435	NaN	NaN	NaN	NaN	NaN
	0.95	0.004496	0.004898	NaN	NaN	NaN	NaN	NaN
	1	0.004923	0.005523	NaN	NaN	NaN	NaN	NaN

C_{df}		M						
		0.2	0.3	0.4	0.5	0.6	0.7	0.7501
$\bar{C}$	0	0.005275	0.005250	0.005213	0.005164	0.005099	0.005007	0.004909
	0.05	0.005305	0.005278	0.005239	0.005187	0.005119	0.005023	0.004936
	0.1	0.005332	0.005302	0.005261	0.005206	0.005135	0.005034	0.004957
	0.15	0.005351	0.005322	0.005279	0.005221	0.005147	0.005043	0.004967
	0.2	0.005366	0.005335	0.005291	0.005232	0.005156	0.005049	0.004967
	0.25	0.005378	0.005344	0.005298	0.005236	0.005157	0.005048	0.004965
	0.3	0.005392	0.005351	0.005300	0.005235	0.005153	0.005044	0.004959
	0.35	0.005456	0.005407	0.005354	0.005277	0.005170	0.005041	0.004942
	0.4	0.005501	0.005446	0.005388	0.005315	0.005218	0.005031	0.004915
	0.45	0.005522	0.005351	0.005285	0.005332	0.005160	0.004983	0.004894
	0.5	0.005554	0.005464	0.005276	0.005299	0.005070	0.004932	0.004885
	0.55	0.005554	0.005482	0.005431	0.005213	0.005026	0.004881	0.004871
	0.6	0.005560	0.005455	0.005407	0.005195	0.005058	0.004838	0.004839
	0.65	0.005564	0.005495	0.005387	0.005089	0.004921	0.004806	0.004785
	0.7	0.005558	0.005489	0.005353	0.004944	0.004705	0.005019	NaN
	0.75	0.005546	0.005449	0.005242	0.004733	0.004573	NaN	NaN
	0.8	0.005555	0.005451	0.004626	0.003300	0.002824	NaN	NaN
	0.85	0.005552	0.005440	0.004358	NaN	NaN	NaN	NaN
	0.9	0.005560	0.005418	NaN	NaN	NaN	NaN	NaN
	0.95	0.005549	0.005393	NaN	NaN	NaN	NaN	NaN
	1	0.005525	0.005330	NaN	NaN	NaN	NaN	NaN

Appendix C: Comparison of Turntable Surface Discontinuity to Boundary Layer Thickness

Here, the height of the surface discontinuity of a 40%-diameter turn table operating at 45 degrees sweep is compared to the boundary layer thickness of the OW4 airfoil at a Reynolds number of $9x10^6$.

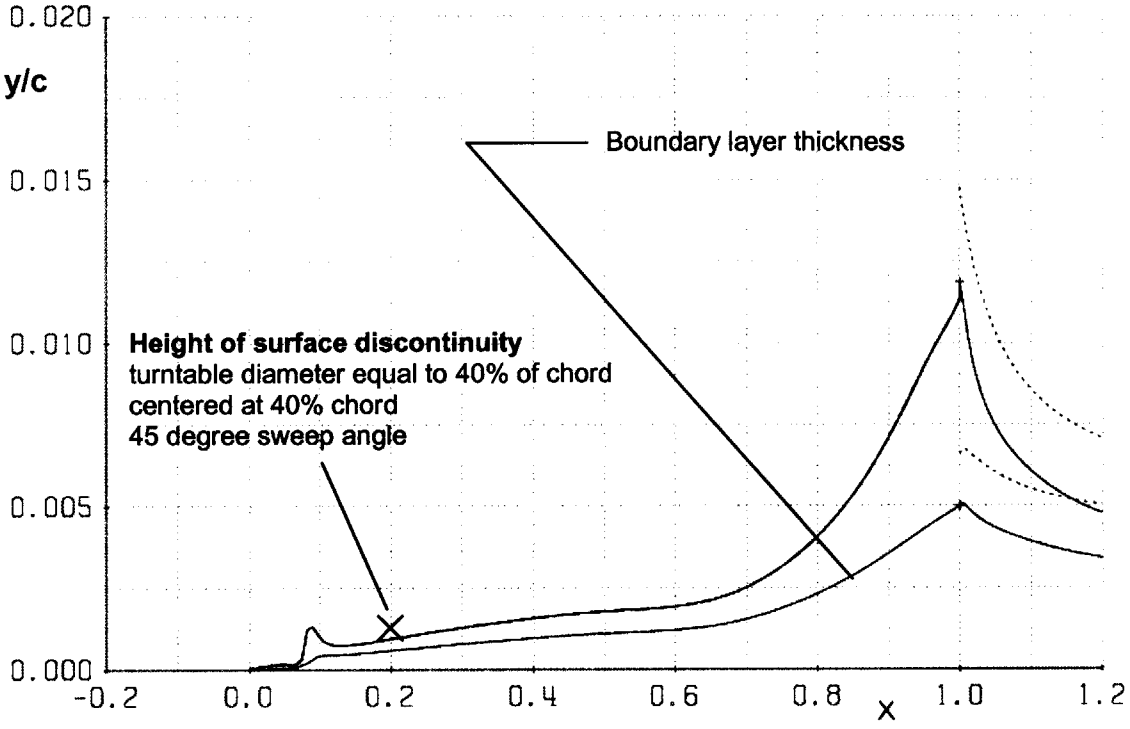

Appendix D: 'Flat-top' Airfoil Characteristics

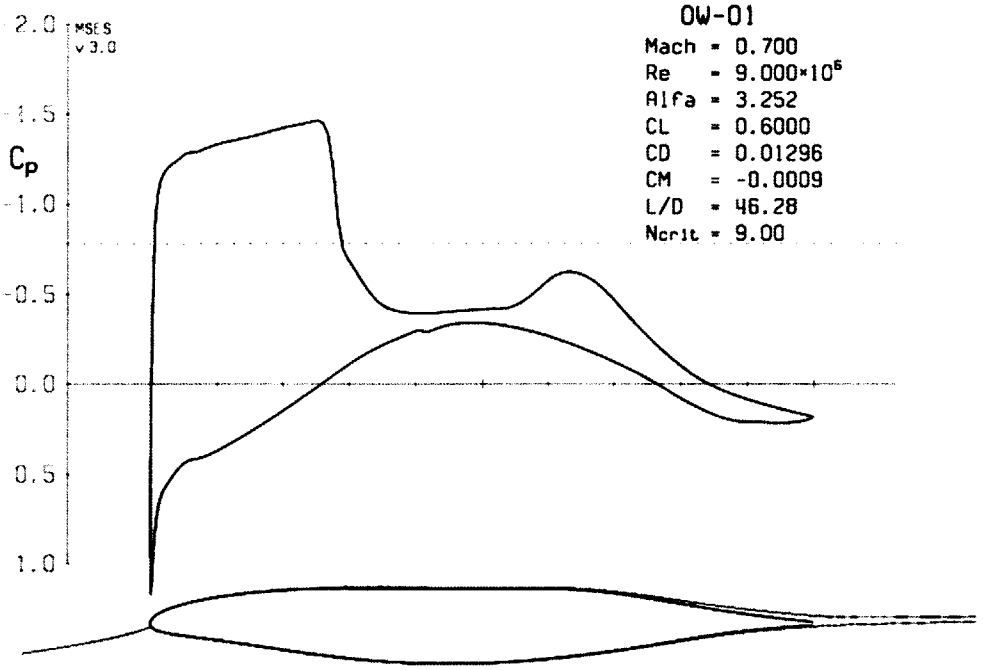

Appendix E: Stagnation Point Inlet Dimensions

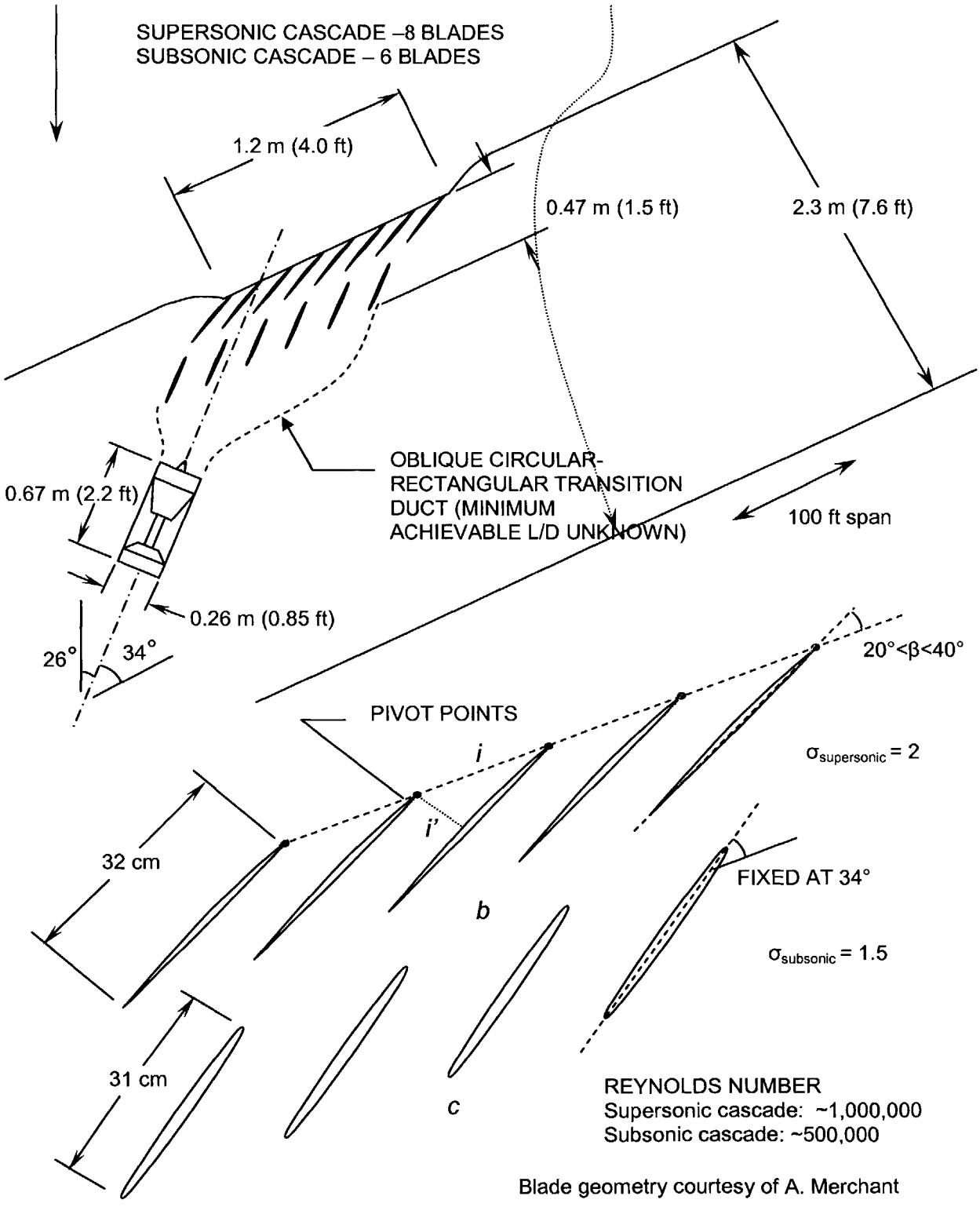

Blade geometry courtesy of A. Merchant

References

[1] Kress, R. W., "The Evolution of Aircraft Wing Design" AIAA Paper, 1980.

[2] Warwick, G., "Strange Shapes," Flight International, 13 September 2005.

[3] Verani, M., et al., "F-111 Case Study," Aircraft Systems Case Study, Massachusetts Institute of Technology, December 2003.

[4] Curry, M., "Past Projects – AD-1 Oblique Wing," NASA History Archive, 7 April 2005.

[5] Nickel, K., Wohlfahrt, M., "Tailless Aircraft in Theory and in Practice," Edward Arnold, London, 1994.

[6] "Quiet Supersonic Platform (QSP)," Global Security. http://www.globalsecurity.org/military/systems/aircraft/qsp.htm (5 November 2005).

[7] Correspondence with Thomas Beutner, DARPA.

[8] Shachtman, N., "DARPA Wants Mach 2, Uneven Flying Wing," Defense Tech, 17 October 2005.

[9] Warwick, G., "DARPA Seeks Oblique Wing Design," Flight International, 6 September 2005.

[10] Van der Velden, A., Kroo, I., "Aerodynamic Design and Synthesis of the Oblique Flying Wing Supersonic Transport," Ph.D. Thesis, Stanford University, May 1992.

[11] Morris, S., Tigner, B., "Flight Tests of an Oblique Flying Wing Small Scale Demonstrator," AIAA paper No. 95-3327-CP, Guidance, Navigation and Control Conference, August 1995, Baltimore, MD.

[12] Morris, S.J., "Integrated Aerodynamics and Control System Design for Oblique Wing Aircraft," Ph.D. Thesis, Stanford University, June 1990.

[13] Waters, M. et al., "Structural and Aerodynamic Considerations for an Oblique All-Wing Aircraft," AIAA 92-4220, AIAA Aircraft Design Meeting, August 1992.

[14] Nicolai, L. M., "Fundamentals of Aircraft Design," University of Dayton, Dayton, OH, 1975.

[15] Jones, R. T., Wing Theory. Princeton University Press, Princeton, NJ, 1990.

[16] Raymer, D. P., "Aircraft Design: A Conceptual Approach," 3rd ed., AIAA Education Series, AIAA, Reston, VA, 1999.

[17] Hendrickson, R. et al., "Drag: An Introduction," Dragbusters, January 1997, http://www.aoe.vt.edu/~mason/Mason_f/CAtxtChap5.pdf

[18] Prandtl, L., "Tragflügel Theorie," *Nachricten von der Gesellschaft der Wissenschaften zu Göttligen*, Ges-chäeftliche Mitteilungen, Klasse, 1918, pp. 451-477.

[19] Sears, W. R., "On Projectiles of Minimum Wave Drag," Quart. J. Appl. Math. 4, no. 4, January 1947.

[20] Smith, J. H. B., "Lift/Drag Ratios of Optimized Slewed Elliptic Wings at Supersonic Speeds," The Aeronautical Quarterly, Vol. 12, 1961, pp. 201-218

[21] Butler, M. E., "Supersonic 'Oblique All Wing' Airfoil Design," M. S. Thesis, Massachusetts Institute of Technology, September 1993.

[22] Kurkchubasche, R. R., "Lift to Drag Ratios for the Oblique Flying Wing Transport," Technical Report, Stanford University, August 1990.

[23] Drela, M., "The Oblique Flying Wing: Advantages and Challenges," Technical Report, Massachusetts Institute of Technology, March 2005.

[24] Lynch, F. T., "Commercial Transports—Aerodynamic Design for Cruise Performance Efficiency," Progress in Astronautics and Aeronautics, D. Nixon, ed., Vol. 81, AIAA, 1982, pp. 81–147.

[25] Corning, G., "Supersonic and Subsonic CTOL and VTOL Airplane Design," 4th ed., published by author, College Park, MD, 1960.

[26] Kurzke, J., GasTurb, Software Package, v9, 2005.

[27] Kerrebrock, J. L., "Aircraft Engines and Gas Turbines," MIT Press, Cambridge, MA, 1992.

[28] Eminton E., "On the Numerical Evaluation of the Drag Integral," RM 3341, RAeS 1961.

[29] Brear, M. J., et al., "Propulsion System Requirements for Quiet, Long Range, Supersonic Aircraft," presented at the 4th ASME/JSME Joint Fluids Engineering Conference, July 6-10, Waikiki, Hawaii.

[30] Roxburgh, G., "Concorde: Technical Specifications," http://www.concordesst.com/performance.html. (4 November 2005)

[31] Private communication with Dr. Ali Merchant of the Massachusetts Institute of Technology.

[32] Smith, L. H., "Wake Ingestion Propulsion Benefit," Journal of Propulsion and Power, Vol. 9, No. 1, January-February 1993, pp. 74-82.

[33] Hill, P. and Peterson, C., "Mechanics and Thermodynamics of Propulsion," 2nd ed., Addison Wesley, Reading, MA, 1992.

[34] Masuda, K., and Yoshida, K., "Improving the Lift to Drag Characteristics of SST," AIAA 91-3105.